THEORETICAL STUDY OF STRUCTURAL TRANSFORMATIONS AND PROPERTIES OF SELECTED MATERIALS AT EXTREME CONDITIONS

A Thesis Submitted to the College of

Graduate and Postdoctoral Studies

In Partial Fulfillment of the Requirements

For the Degree of Doctor of Philosophy

In the Department of Physics and Engineering Physics

University of Saskatchewan

Saskatoon

By

Arnab Majumdar

PERMISSION TO USE

ABSTRACT

There are several objectives that have been addressed in this thesis. Under a broader heading, the methods that have been explored and applied are density functional theory (DFT), *ab initio* metadynamics and *ab initio* molecular dynamics (AIMD). These methods have been employed to analyze structural phase transitions, electronic, vibrational and transport properties of selected materials at high pressure. All the materials that have been considered in this thesis have been studied experimentally by various research groups. Using theoretical methods and the sophisticated computational tools mentioned above, the aim of this thesis is to predict as well explain the experimental observations, thus bridging the gap between experiment and theory. The thesis has been divided as follows.

The first project that has been discussed is on the structural phase transition of aluminium triiodide (AlI_3). Experimentally, no structural phase transition was reported for crystalline AlI_3 at high pressure in spite of getting certain subtle results which hinted at a first order phase transition. Thus, in our study, we employed *ab initio* metadyanamics to scan the potential energy surface (PES) and find the energetically most stable configuration. Indeed, we found first order structural phase transition at approximately 1.3 GPa which was verified by the Raman spectra as well.

The next project was to explore the structure of the superconducting phase of hydrogen sulfide (H_2S) which was experimentally observed to have a high superconducting critical temperature of 203 K. However, the crystal structure of the superconducting phase has been ambiguous and has been proposed to be a metastable phase. Therefore, in our study, we performed *ab initio* metadyanamics to search for metastable phases. At 80 GPa and 80 K, a metastable structure was found. This metastable structure on further *ab initio* molecular dynamics (AIMD) at

200 GPa and 200 K resulted in a modulated structure whose X-Ray diffraction (XRD) pattern matched excellently with that obtained experimentally. Analysis of the electron-phonon interactions on this modulated structure gave superconducting critical temperatures close to the value obtained experimentally.

The third project is based on the electron-phonon interaction and subsequent calculation of superconducting properties of an experimentally synthesized polyhydride of iron, FeH_5. The structure was found to have hydrogen in the atomic form, which has long since been proposed to be a criterion for high temperature superconductivity. First principles theoretical calculations revealed FeH_5 to be a superconductor at high pressure albeit with a low critical temperature of 51 K at 130 GPa, confirming a hypothesis that the superconductivity of any material is sensitive to several factors that have been discussed in the chapter.

The final project deals with the study of structural, electronic and transport properties of glass and molten basalt (igneous rock). This material is amorphous and abundant in the Earth's mantle. Although several experimental and theoretical studies have been performed on materials that mimic basalt, there is still a lot to be unravelled regarding its structural and transport properties at the mantle conditions. A clear understanding of the structure and transport properties of basalt can explain in depth about the thermochemical evolution of the Earth and origin of life. In the study reported in this thesis, *ab initio* molecular dynamics simulations were performed on an amorphous model basalt structure (containing the most abundant chemical species, Si, Al, Ca, Mg and O) at the mantle conditions over a range of high pressures. The results that have been reported here are in very good agreement with earlier experimental and theoretical results, confirming that the model basalt considered is indeed a good approximation and can be further improved by considering the minor occurring elements (Na, K, *etc.*) for future research.

The research in this thesis are a result of collaborations between the authors, Arnab Majumdar, supervisors Prof. John S. Tse and Prof. Yansun Yao of the Department of Physics and Engineering Physics at the University of Saskatchewan, and Dr. Dennis D. Klug, Principal Research Scientist at the National Research Council in Ottawa, Canada, whose contributions are described below.

Chapter 1 describes the underlying theory and computational tools employed in this thesis, and was written by Arnab Majumdar.

Chapter 2 is a slightly modified version of an article (*vide infra*) published in the Journal of Chemical Physics. Alongside Arnab Majumdar, the peer reviewed article has been co-authored by Dr. Dennis D. Klug and Prof. Yansun Yao. Calculations of the equation of state, thermodynamic stability, *ab initio* metadynamics calculations, phonon dispersion and electronic were performed by Arnab Majumdar. Analysis of the above was carried out by Arnab Majumdar and Prof. Yansun Yao. The calculation and analysis of the Born effective charges and Raman tensors were performed by Dr. Dennis D. Klug. Drafting of the manuscript was done by all the authors.

Chapter 3 has been partially published in Angewandte Chemie International Edition (*vide infra*), while the remaining portion is currently being drafted. The calculations pertaining to *ab initio* metadynamics, equation of state, electronic band structures, Bader charge analysis, phonon dispersion, electron-phonon coupling and superconducting properties were performed by Arnab Majumdar. The analysis of the above were done by Arnab Majumdar, Prof. John S. Tse and Prof. Yansun Yao. The calculation and analysis of vibrational properties were done by Arnab Majumdar,

Prof. John S. Tse and Prof. Yansun Yao. Prof. John S. Tse and Prof. Yansun Yao carried out the *ab initio* molecular dynamics simulations. Drafting of the manuscript was done by all the authors.

Chapter 4 is a slightly modified version of an article (*vide infra*) published in Physical Review B. Optimization of the FeH_5 structure was done by Prof. John S. Tse. Calculation of the phonon dispersion, electron phonon coupling and superconducting properties of the material were carried out by Arnab Majumdar. Arnab Majumdar, Prof. John S. Tse and Prof. Yansun Yao were all responsible for analysing and drafting the manuscript.

Chapter 5 is currently being drafted for publication. All the *ab initio* molecular dynamics, equation of state, thermodynamic, elastic, electronic and transport properties were done by Arnab Majumdar. Analysis of the above were performed by Arnab Majumdar and Prof. John S. Tse.

Chapter 6 is a general conclusion of the thesis and is solely written by Arnab Majumdar.

ACKNOWLEDGEMENTS

জীবনমরণের সীমানা ছাড়ায়ে,
বন্ধু হে আমার, রয়েছ দাঁড়ায়ে ॥

Dedicated to Rabindranath Tagore (first Asian Nobel Laureate), for always being there in spirit

TABLE OF CONTENTS

LIST OF TABLES

LIST OF FIGURES

xiii

LIST OF ABBREVIATIONS

0D	Zero Dimensional
3D	Three Dimensional
AIMD	ab initio Molecular Dynamics
BCC	Body-centred Cubic
BCS	Bardeen-Cooper-Schrieffer
BO	Born-Oppenheimer
BZ	Brillouin Zone
CV	Collective Variables
DAC	Diamond Anvil Cell
DFPT	Density Functional Perturbation Theory
DFT	Density Functional Theory
DOF	Degrees of Freedom
DOS	Density of States
EOS	Equation of State
EPC	Electron Phonon Coupling
FFT	Fast Fourier Transform
FCC	Face-centred Cubic
FPMD	First Principles Molecular Dynamics
GED	Gas-phase Electron Diffraction
GGA	Generalized Gradient Approximation
HCP	Hexagonal Close Packed
HK	Hohenberg-Kohn
HSE	Heyd-Scuseria-Ernzerhof
KS	Kohn-Sham
LDA	Local-Density Approximation
LSDA	Local Spin-density Approximation
MD	Molecular Dynamics
MP	Monkhorst Pack
MSD	Mean Squared Displacement
NMR	Nuclear Magnetic Resonance
NPT	Constant Pressure and Constant Temperature
NVT	Constant Volume and Constant Temperature
PAW	Projector Augmented Wave
PBC	Periodic Boundary Conditions
PBE	Perdew-Burke-Ernzerhof
PES	Potential Energy Surface
PW	Plane Wave
RDF	Radial Distribution Function

SACF	Stress Autocorrelation Function
U	Hubbard Parameter
VASP	Vienna ab initio Simulation Package
vDOS	Vibrational Density of States
VF	Verlet Leapfrog
VV	Velocity Verlet
XC	Exchange-Correlation
XRD	X-Ray Diffraction

CHAPTER 1

INTRODUCTION AND THEORETICAL METHODS

The discovery of novel materials is often a result of industrial, societal, economic and logistic needs. Therefore, it has become the norm to fabricate new materials by tweaking the intrinsic parameters of the conventional materials by controlling them during the synthesis, for example, manipulating the chemical composition and dimensionality of the system. Another method is by varying the external parameters which often give rise to completely new, otherwise unknown structures with absolutely different properties (electronic, optical, *etc.*) compared to the same materials at ambient conditions. Some of these external parameters are extreme pressures and temperatures, application of electric and magnetic fields and so on. Of the abovementioned external factors which can bring about significant changes in materials, the thermodynamic variable, pressure, has the potential to vastly change structural and other dependant properties. Starting from influencing the interatomic electrostatic interactions to modifying the microstructure, application of pressure enables the formation of new materials not prevalent at ambient conditions. In the last few decades, this has helped high pressure researchers not only to synthesize new materials but also understand the underlying science and contribute further to the dissemination of scientific knowledge [1-12]. To mention explicitly, how pressure gives rise to new structures, it is imperative to briefly discuss some established results obtained from high pressure research. Firstly, on exerting pressure, the interatomic distances and hence the bonding patterns change. The energetic stability also changes, often being responsible for structural phase transition. The thermodynamic work ($P\Delta V$) if increased considerably, can contribute to the overcoming of energy barriers and help the system attain a new thermodynamically stable configuration, in other words form a new structure. The most common example is that of the compression of graphite into diamond. Similarly, on

compressing hexagonal boron nitride, cubic boron nitride is formed [13]. Several industrially applicable properties also emerge at high pressures, *e.g.* occurrence of superconductivity in insulating materials when compressed, extreme hardness and high energy density. Secondly, owing to the limitations of our conventional knowledge of rules of chemistry at ambient conditions, certain stoichiometry are not conceived of. However, apart from modifying the potential energy surface, pressure can also alter the compositional landscape. For instance, the occurrence of unusual stoichiometry of $NaCl_3$ [14], *etc.* were previously unheard of. Thirdly, as previously stated, the $P\Delta V$ term, *i.e.* the thermodynamic work is capable of interfering with inter and intra-atomic interactions, leading to unprecedented chemical bonds and properties. Surprisingly, even noble gases have been shown to undergo chemical reactions theoretically, with other elements such as Li, Mg and Ni [15-17]. These discoveries question the conventional concepts in chemistry on the formation and stability of chemical bonds, the mechanism of how atoms and molecules reorganize at short and long ranges, and how kinetics and thermodynamics govern material stability. Lastly, even if the material doesn't undergo structural phase transition or the stoichiometry remains constant, the applied pressure reduces the interatomic distances, altering interatomic interactions and in turn modifying electronic properties. This is one of the most common areas of high pressure research. The conversion of an insulator to a semi-conductor, then to a metal and eventually to a superconductor has been observed several times. Some of the best examples showing this trait are of H_2S [18], Silane [19], *etc.* This property can have huge industrial impact. Recently developed structure searching methods based on accurate first-principles energetic calculations have enabled the theoretical design of high-pressure materials. The effective collaboration between experimentalists and theoreticians has greatly expedited materials discovery at high pressures [20]. Experimentally, high pressure can be applied by the use of Diamond Anvil Cells (DAC) which generate static pressure. The other dynamic method of generating pressure is by imparting shock

waves to the system in concern. The diamond anvil cell is one of the most widely used devices to generate extremely high pressures. Apart from extreme compression, DAC enables the *in situ* measurement of X-ray diffraction (XRD), Raman and infrared spectroscopy. The efficiency of DACs has been increasing steadily over the years, until recently when pressures of more than 1TPa have also been achieved [21]. But such extreme conditions are difficult to attain and sustain. Another disadvantage of using diamond anvil cells is the very low size of the sample that has to be used. But these shortcomings may be bypassed with the use of theoretical techniques by the help of simulating high pressure scenarios on a computer. First-principles density functional theory (DFT) [22-23] revolutionized the way materials are studied today. Not only can one simulate previously unknown materials but can also study their various properties. This is the tool that has been used in our research too. Extremely high pressure which is a feat to achieve in the experimental facility, can very easily be simulated on a computer by varying the size of the system (unit cell) being studied. The total energy can be minimized for different structures as a function of pressure, thus allowing the investigation of pressure-induced structural phase transitions. Energy calculations using DFT precisely distinguish the relative stabilities of competing phases within the resolution of a few meV. These calculations can therefore provide a more deep insight and further assist in understanding experimental observations; for example, in the determination of the actual phase stability and the assignment of electronic and vibrational excitation modes. In the last a few years, remarkable progress has been made in the development of first-principles crystal-structure searching methods, leading to several successful high-pressure discoveries [20]. Structure-searching methods combined with reliable DFT calculations can explore complicated free-energy surfaces to seek the global energy minimum corresponding to the most stable ground-state structure. Just by the knowledge of the chemical composition, these computational methods can identify the thermodynamically stable structures of materials under pressure enabling the theory to

have a predictive power that can be beneficial for experimentalists. Several efficient global optimization schemes for predicting the correct and stable structures have been developed. These codes that are frequently used in high-pressure research include methods designed to overcome energy barriers such as simulated annealing [24], minima hopping [25], *ab initio* molecular dynamics [26-27], metadynamics algorithms [28] and global minimization methods such as random sampling [29], genetic algorithms [30–33] and so on. Some of these methods will be discussed in details in the following sections.

High pressure has been one of the primary tools to give rise to new superconductors. In conventional superconductors, the superconductivity arises by the exchange of phonons between two electrons. The application of pressure on metals, for example, elemental metals [34-35] like Ca, Cs, Y, Fe, *etc*. generate new structures which are superconducting. Some non-metallic elements like B, O, Si, *etc*. lose their insulating or semiconducting properties and turn into superconductors under high pressures [34]. Similarly, superconducting properties of some novel materials under high pressures will be discussed in detail in the later chapters of this thesis.

In this thesis, some of the above mentioned theoretical techniques have been used to study the structural phase transitions of materials at high pressures and determining their electronic, thermodynamic, and other properties. The works that have been reported in this thesis are (i) verifying the structural phase transition of AlI_3 at high pressure using *ab initio* metadynamics method and reporting of a new phase after approximately 2 GPa, (ii) theoretically determining the superconducting phase of hydrogen sulfide (H_2S) at high pressure inspired by the experimental discovery of high temperature superconductivity in compressed H_2S [18]. This project was also carried out using *ab initio* metadynamics as well as *ab initio* molecular dynamics (AIMD), (iii) superconductivity in FeH_5. This theoretical study followed the experimental finding of a new stoichiometry of iron polyhydride [36] at high pressure. Given the tendency of covalent hydrides

to show high temperature superconductivity, hence this material was investigated for high critical temperature (T_c) superconductivity, and the last project reported is (iv) determining the structural phase transition and transport properties of Basalt at the deep mantle conditions. For this project AIMD has been extensively used to simulate the basalt system over large time scales.

While studying any material, the underlying science is that of the atoms which consist of electrons and nuclei. Therefore, it is necessary to treat the particles, namely electrons and nuclei in a quantum mechanical manner. Small systems have been successfully studied using the Schrödinger equation. But it becomes cumbersome when treating bigger systems with many atoms. Therefore, several approximate numerical solutions have been introduced over the years to solve many body problems. One of the methods is using first-principles methods, *i.e*. a method which does not require any input parameter obtained from experiments. One such method, density functional theory, is discussed henceforth, starting from the initial approximations to the final implementation of the method.

1.1 Schrödinger Equation and Born-Oppenheimer Approximation

Over the past few decades, DFT has been one of the most successful and popular quantum mechanical approaches to solve many body problems. It has applications in physics and chemistry in a conventional manner as well as in interdisciplinary fields, for example biology and mineralogy. Superconductivity, magnetic properties, bond characteristics, and other properties have been studied using DFT as the tool. To explain the basis of DFT, we will tread a step back to the Schrödinger equation. From quantum mechanics we know that all the information of a system is stored in the wavefunction. The wavefunction itself is determined from the Schrödinger equation (Eq. 1.1) as follows,

$$\left(\frac{-\hbar^2}{2m}\nabla^2 + V(\vec{r})\right)\psi(\vec{r}) = E\psi. \tag{1.1}$$

This is for a single particle which is subjected to the external potential $V(\vec{r})$. Hence, with the proper form of $V(\vec{r})$, the wavefunction can be found out from Eq. (1.1) and subsequently all other observables can be computed, taking the expectation values with respect to the wavefunction. This is fairly straightforward to calculate. The challenge arises when there are more than one particle. The Schrödinger equation then reads as

$$\left[\sum_i^N\left(\frac{-\hbar^2}{2m}\nabla_i^2 + V(\vec{r}_i)\right) + \sum_{i\neq j}U(\vec{r}_i,\vec{r}_j)\right]\psi(\vec{r}_1,\vec{r}_2,...\vec{r}_N) = E\psi(\vec{r}_1,\vec{r}_2,...\vec{r}_N), \tag{1.2}$$

where N is the total number of particles and $U(\vec{r}_i,\vec{r}_j)$ is the Coulombic electron-electron interaction as shown in Eq. (1.3).

$$U(\vec{r}_i,\vec{r}_j) = \frac{e^2}{|\vec{r}_i - \vec{r}_j|}. \tag{1.3}$$

Since the denominator in Eq. (1.3) can't be separated algebraically to convert it into a single particle problem, the new strategy, DFT was introduced. In this theory the many body problem with the electron-electron interaction term, $U(\vec{r}_i,\vec{r}_j)$, is mapped onto a single body problem without the $U(\vec{r}_i,\vec{r}_j)$ term. For a system of N interacting electrons and M nuclei, the Hamiltonian is written as,

$$\hat{H} = -\frac{1}{2}\sum_{i=1}^N\nabla_i^2 + \frac{1}{2}\sum_{i=1}^N\sum_{j\neq i}^N\frac{1}{|\vec{r}_i-\vec{r}_j|} - \frac{1}{2}\sum_{A=1}^M\frac{1}{M_A}\nabla_A^2 - \sum_{i=1}^N\sum_{A=1}^M\frac{Z_A}{r_{iA}} + \frac{1}{2}\sum_{A=1}^M\sum_{B\neq A}^M\frac{Z_AZ_B}{|\vec{R}_A - \vec{R}_B|}. \tag{1.4}$$

This equation is expressed in atomic units (*a.u.*) (Hartree is the unit of the energy and $\hbar = 1$, $e = 1$, and $m_e = 1$). The first two terms in Eq. (1.4) correspond to the kinetic energy and Coulomb interaction potential of the electrons, respectively. The next two terms are the kinetic energy of the

nuclei and Coulomb interaction between the electrons and nuclei respectively. The last term represents the Coulomb interaction potential of the nuclei. In principle, all the properties of a system can be obtained by solving the many-body Schrödinger equation. Practically, a full quantum mechanical treatment is only solvable for the simplest of systems, *e.g.* hydrogen atom. In liquids or crystals, the total number of electrons and nuclei is of the order of 10^{23}. The motion of one particle affects other particles, modifying the Coulomb potential and experiencing a force and therefore the other particles too have to move in order to maintain equilibrium in the structure. Thus, in a system with more than one atom, the motions of all the particles are correlated. With the increment in the number of degrees of freedom, the correlation between all the particles also increases. In order to study such systems, the motions of the electrons are decoupled from that of the nuclei following the Born-Oppenheimer (BO) approximation, a method introduced by Max Born and J. Robert Oppenheimer in 1927 [37]. The BO approximation is also known as the 'adiabatic approximation' in describing electronic structures. This approximation is based on the fact that the mass of the electrons is much lesser than that of the nuclei and their velocities are consequently much larger than that of the nuclei. Using this concept, the movement of the electrons and nuclei can be separated. For a particular configuration of the nuclei, one can thereby describe the electronic structure separately and allow the electrons to relax to optimal eigenstates before the nuclei move to the next arrangement. Mathematically, the Hamiltonian for the electrons in Eq. (1.4) becomes:

$$\widehat{H_e} = -\frac{1}{2}\sum_{i=1}^{N}\nabla_i^2 - \sum_{i=1}^{N}\sum_{A=1}^{M}\frac{Z_A}{r_{iA}} + \frac{1}{2}\sum_{i=1}^{N}\sum_{j\neq i}^{N}\frac{1}{|\vec{r}_i - \vec{r}_j|}. \tag{1.5}$$

Within the BO approximation, for a given nuclear configuration, the kinetic energy of the nuclear Coulomb potential can be considered to be constant. The electrons can now be considered as

moving in an external potential (V_{ext}) due to Coulomb interactions between the electrons and the nuclei. This simplified Hamiltonian depends only parametrically on the coordinates of the nuclei. The total energy of a poly-atomic system at a given spatial configuration is the sum of the total energy of the electronic many-body system and the classical inter-nuclei Coulomb repulsion:

$$E_{Total} = E_e + E_{ion} .\tag{1.6}$$

1.2 Density functional theory

In DFT, the total electronic energy of a system rather than being a function of the spatial coordinates is just a functional of the electron density. DFT achieved great success in electronic structure calculations of atoms, molecules and condensed matter since the last few decades. Its concept has its foundations in the Thomas-Fermi theory introduced in 1927, which formulated the equation of the total energy of a many-electron system as a density-based expression [38-40]. Eventually in the 1960s, DFT was formalized by Kohn and Hohenberg [22-23]. Within the realm of computational materials science, *ab initio* DFT calculations enable the prediction and calculation of the characteristics of materials, based on quantum mechanical considerations, without requiring higher order parameters such as fundamental material properties. In contemporary DFT techniques, the electronic structures are determined by using a potential acting on the system's electrons. This potential is the sum of external potentials, determined solely by the structure and the elemental composition of the system, and an effective potential, which represents electron-electron interactions. Thus, a problem for a representative super-cell of a material with *n* electrons can be studied as a set of *n* one-electron Schrödinger like equations, which are also known as Kohn–Sham equations, hence reducing the problem to a single body problem.

1.2.1 Hohenberg–Kohn Theorem

The Hohenberg-Kohn (HK) theorem, introduced in 1964, states that the external potential $V_{ext}(\vec{r})$ is (to within a constant) a unique functional of $\rho(\vec{r})$ [22], assuming a non-degenerate ground state. In other words, the HK theorem demonstrates that the electron density uniquely determines the Hamiltonian operator and thus all the properties of the system. The proof is as follows. Let us assume that there are two external potentials $V_{ext}(\vec{r})$ and $V'_{ext}(\vec{r})$ that differ by a constant and each gives the same density $\rho(\vec{r})$ for its ground state. We will have two Hamiltonians $\hat{H}$ and $\hat{H}'$ whose ground-state densities are the same although the normalized wave functions ψ and ψ' will be different. Taking ψ' as a trial wave function for the H problem,

$$E_0 < \langle \psi' | \hat{H} | \psi' \rangle = \langle \psi' | \hat{H}' | \psi' \rangle + \langle \psi' | \hat{H} - \hat{H}' | \psi' \rangle = E'_0 + \int \rho(\vec{r}) \, [V_{ext}(\vec{r}) - V'_{ext}(\vec{r})] d\vec{r} \,,$$

$$(1.7)$$

where E_0 and E'_0 are the ground-state energies for $\hat{H}$ and $\hat{H}'$, respectively. Similarly, taking ψ as the trial function for the $\hat{H}'$ problem,

$$E'_0 < \langle \psi | \hat{H}' | \psi \rangle = \langle \psi | \hat{H} | \psi \rangle + \langle \psi | \hat{H}' - \hat{H} | \psi \rangle = E_0 + \int \rho(\vec{r}) \, [V'_{ext}(\vec{r}) - V_{ext}(\vec{r})] d\vec{r}.$$

$$(1.8)$$

Adding Eqs. (1.7) and (1.8), we obtain $E_0 + E'_0 < E'_0 + E_0$, which is a contradiction and therefore there cannot be two different $V_{ext}(\vec{r})$ that give the same $\rho(\vec{r})$ for the ground state. Thus the first Hohenberg-Kohn theorem states that there is a one-to-one correspondence between the external potential $V_{ext}(\vec{r})$ and the ground state density $\rho(\vec{r})$. A universal functional of the total energy as a function of density must exist. The second HK theorem is a proof of the fact that the exact ground state density minimizes this universal functional and the corresponding energy is the exact ground

state energy. In spite of extensive research to formulate an exact universal energy functional, researchers have not yet been able to come up with one.

1.2.2 Kohn-Sham Formulation of DFT

In 1965, Kohn and Sham [23] devised a practical scheme to calculate the total energy. This method is the basic procedure for DFT calculations. A model of non-interacting electrons moving in an effective local potential to reproduce the interacting electrons in the external potential was proposed. The electronic energy functional can be written as,

$$E_{electron}[\rho] = F[\rho] + \int d\vec{r} V_{ext}(\vec{r}) . \rho(\vec{r}).$$ (1.9)

$$V_{ext} = \sum_{i=1}^{N} \sum_{A=1}^{M} \frac{Z_A}{r_{iA}}.$$ (1.10)

In Eq. (1.9), $F[\rho]$ contains all the kinetic energy terms and electron-electron interactions. If we separate out the Coulombic interaction, then $F[\rho]$ can be written as

$$F[\rho] = \frac{1}{2} \int \int d\vec{r} d\vec{r}' \frac{\rho(\vec{r})\rho(\vec{r}')}{|\vec{r} - \vec{r}'|} + T_S[\rho] + E_{xc}[\rho],$$ (1.11)

where $T_S[\rho]$ is the kinetic energy functional of the non-interacting electrons and $E_{xc}[\rho]$ is the exchange correlation functional. E_{xc} is simply the sum of the error made in using a non-interacting kinetic energy and the error made in treating the electron-electron interaction classically. The minimization of the electronic energy functional with respect to the electron density subject to the constraint, $\int d\vec{r} \rho(\vec{r}) = N$ leads to,

$$V_{ext} + \frac{\delta E_{xc}[\rho]}{\delta\rho(\vec{r})} + \frac{\delta T[\rho]}{\delta\rho(\vec{r})} + \int d\vec{r}' \frac{\rho(\vec{r}')}{|\vec{r} - \vec{r}'|} = \mu,$$ (1.12)

where μ is a Lagrange multiplier. Considering the many-body wavefuntion to be a product of all the one electron wavefunctions φ_i, each electron wavefunction in the non-interacting system satisfies the one-electron Schrödinger equation,

$$\left(-\frac{1}{2}\nabla^2 + V_{ext}(\vec{r})\right)\varphi_i(\vec{r}) = \varepsilon_i\varphi_i(\vec{r}). \tag{1.13}$$

Kohn and Sham extrapolated this idea to the case of interacting electrons and derived the effective potential as

$$v_{eff} = V_{ext} + \frac{\delta E_{xc}[\rho]}{\delta\rho(\vec{r})} + \int d\vec{r}' \frac{\rho(\vec{r}')}{|\vec{r}-\vec{r}'|}. \tag{1.14}$$

Hence analogous to Eq. (1.13), in the interacting electron system, the equation that each electron satisfies is

$$\left(-\frac{1}{2}\nabla^2 + v_{eff}(\rho)\right)\phi_i(\vec{r}) = \varepsilon_i\phi_i(\vec{r}). \tag{1.15}$$

Eq. (1.15) is known as the Kohn-Sham (KS) equation and v_{eff} depends only on the density. The Eqs. (1.14) and (1.15) are solved self-consistently keeping the total number of electrons constant as the constraint. Once the self-consistent cycles are over and the desired convergence is achieved, the eigenstates and eigenvalues obtained are referred to as the KS orbitals and KS energies, respectively. The ground-state electron density can then be calculated with KS orbitals using the following equation:

$$\rho(\vec{r}) = \sum_{i=1}^{N} |\phi_i(\vec{r})|^2. \tag{1.16}$$

The total energy in the KS scheme is then a sum of the kinetic energy, exchange-correlation energy, Hartree energy and energy due to the potential of the nuclei and it is given as:

$$E_e[\rho(\vec{r})] = \sum_{occ} \varepsilon_i - \frac{1}{2} \iint \frac{\rho(\vec{r})\rho(\vec{r}')}{|\vec{r} - \vec{r}'|} \mathrm{d}\vec{r}\mathrm{d}\vec{r}' + E_{xc}[\rho(\vec{r})] - \int \rho(\vec{r})V_{xc}(\vec{r})\mathrm{d}\vec{r} . \quad (1.17)$$

The schematic diagram (Fig. 1.1) shows how the original system consisting of interacting electrons is mapped onto a system with non-interacting quasi particles.
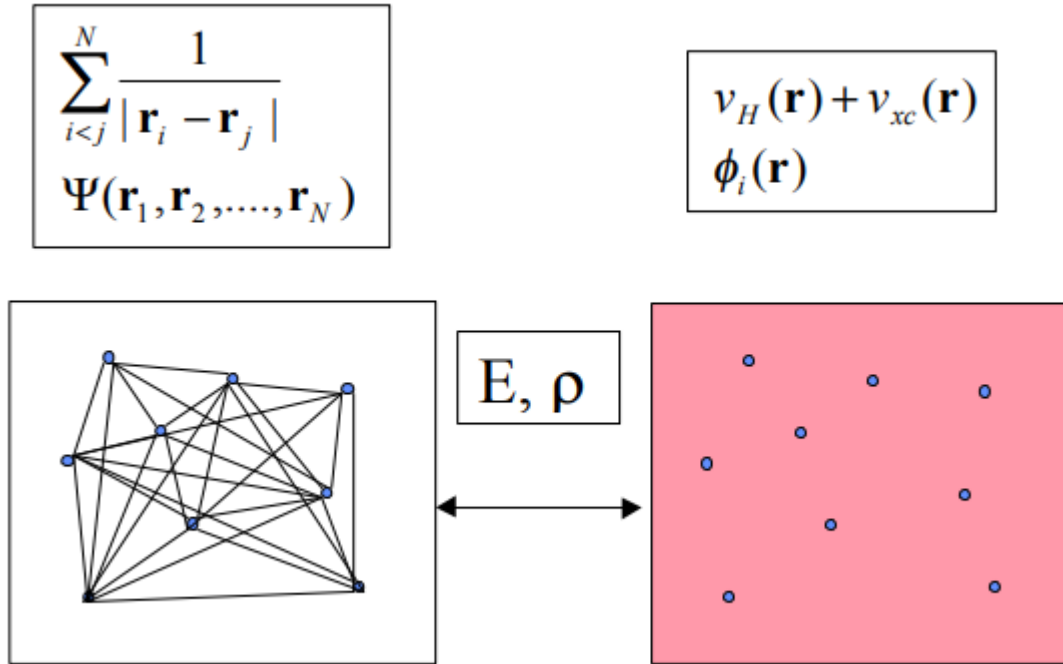
Figure 1.1 Mapping of a many electron interacting system to a system of non-interacting quasi particles of Kohn Sham Density Functional Theory. This figure has been taken from Ref. [41].

1.2.3 Functional Forms of Exchange Correlations

The major feat of DFT is that it mapped the problem of a system of interacting electrons to a system of non-interacting electrons. On making this assumption, the exchange electronic interaction and the difference in kinetic energy of the interacting and non-interacting electrons are collected into a common term, the exchange correlation (XC) energy. The exact form of the XC functional is unknown. This is one of the challenges of DFT which is still being tried to solve. Over the years, many approximations have been proposed for the XC functional $E_{xc}[\rho]$. The first and the

simplest approximation that was introduced was the local-density approximation (LDA). The concept of LDA comes from the assumption that the electron density is constant at all points in space for a uniform electron gas. The exchange-correlation potential from the uniform electron gas is substituted as the XC potential at each point in the non-uniform real system as follows:

$$V_{XC} = V_{XC}^{uniform}[\rho(\vec{r})] . \tag{1.18}$$

Thus, the XC functional can be written as:

$$E_{XC}^{LDA}[\rho] = \int \rho(\vec{r}) \varepsilon_{XC}[\rho(\vec{r})] \, d\vec{r} , \tag{1.19}$$

where,

$$\varepsilon_{XC}[\rho(\vec{r})] = \varepsilon_{XC}^{LDA}[\rho(\vec{r})] . \tag{1.20}$$

The functional $\varepsilon_{XC}[\rho(\vec{r})]$ consists of two parts, *i.e.* the exchange, ε_X and the correlation, ε_C energies. While the correlation part is determined numerically by Monte Carlo simulations for the homogeneous electron gas at a variety of electron densities [42], the exchange part is analytically [43] found to be

$$\varepsilon_X = -\frac{3}{4} \left(\frac{3\rho}{\pi} \right)^{\frac{1}{3}} . \tag{1.21}$$

Since LDA was derived from the uniform electron gas model, it was found to have its limitations in the regime of materials whose electron densities varied considerably (*e.g.* covalent materials) and was not slowly varying. Hence, as a consequence of the shortcomings of LDA, the Generalized Gradient Approximation (GGA) was developed [44-45] to incorporate the varying electron density. The GGA functionals include the dependency of spatial variation in the density. Therefore, GGA functional takes into consideration both the local density and the gradient of the electron density. The general GGA exchange-correlation functional is written as:

$$E_{XC}^{GGA}[\rho] = \int_V \varepsilon_{XC}[\rho]\, F_{XC}[\rho, \nabla\rho]\rho(\vec{r})\mathrm{d}\vec{r}\,. \tag{1.22}$$

F_{XC}, is the enhancement factor that incorporates some modification in the energy density by including the exchange (F_X) and correlation (E_C) terms. F_X is a function of the reduced density. The reduced density is given as:

$$s(\vec{r}) = \frac{|\nabla\rho(\vec{r})|}{2k_f\rho(\vec{r})}\,. \tag{1.23}$$

Here, the k_f is the Fermi wave vector. The formalism of Perdew–Burke–Ernzerhof (PBE) was started with the GGA for correlation in the form:

$$E_c = \int \rho(\vec{r})\{\varepsilon_C^{uniform}[\rho] + H(r_s, \xi, t)\}\,\mathrm{d}\vec{r}\,, \tag{1.24}$$

where $\varepsilon_C^{uniform}[\rho]$ is the correlation energy of the homogeneous electron gas, $H(r_s, \xi, t)$ is the correction term, the r_s is the Seitz radius and is independent of F_x, and t is the dimensionless gradient term defined as:

$$t = \frac{|\boldsymbol{\nabla}\rho(\vec{r})|}{2gk_s\rho(\vec{r})}\,, \tag{1.25}$$

where,

$$g = \frac{[(1+\xi)^{2/3} + (1-\xi)^{2/3}]}{2}\,, \tag{1.26}$$

k_s is dependent on k_f with and $k_s = (4k_f/\pi)^{1/2}$ while ξ is the degree of spin polarization. The GGA functionals have been improved over the years and have taken different forms. The most successful XC functional for electronic structure calculations is the PBE [46] functional. For the PBE functional, the enhancement factor and correlation term are:

$$F_X^{PBE} = 1 + \kappa - \frac{\kappa}{1 + \dfrac{\mu s^2}{\kappa}} \tag{1.27}$$

and

$$E_C^{PBE} = \int \rho(\vec{r})\{\varepsilon_C^{uniform}[\rho] + H(r_s, \xi, t)\}\,d\vec{r}\,. \tag{1.28}$$

The empirical parameters obtained are $\mu \sim 0.2195$ and $\kappa \sim 0.804$ by fitting Eq. (1.27) to various different systems. In the exchange energy of Eq. (1.28), the correction term $H(r_s, \xi, t)$ is written as:

$$H(r_s, \xi, t) = \gamma g^3 \log\left(1 + \frac{\gamma}{\beta} t^2 \frac{1 + At^2}{1 + At^2 + A^2 t^4}\right). \tag{1.29}$$

Once again, from fitting Eq. (1.29) to different systems, $\beta \sim 0.0667$, $\gamma \sim 0.031$ and

$$A = \frac{\beta}{\gamma}\left[\exp\left(\frac{-\varepsilon_C^{uniform}}{\gamma g^3}\right) - 1\right]^{-1}. \tag{1.30}$$

The implementation of PBE has been demonstrated to be highly successful in solid state calculations involving elements, such as Si, C, O, *etc*. [47]. The PBE functional has quite successfully been able to reproduce most of the geometrical parameters and total energy and make major improvements over LDA.

1.2.4 DFT+U

The conventional LDA and GGA functionals are not always the most efficient while determining the electronic band structure and magnetic properties. While they are sufficient for many of the materials, but when it comes to elements with d and f electrons, the LDA and GGA functionals fail. The main reason for the failure is that electrons in d and f orbitals are localized. These localized electrons have very strong inter-electron interactions so they cannot be treated as homogeneous electron gas due to the large gradients in the density and, moreover, the self-interaction term does not get cancelled explicitly. An *ad hoc* approximation is considered to

overcome this problem. In 1991, Anisimov, *et al.* [48] proposed the LDA+U method. A modification is made in the one electron Hamiltonian. A Hubbard like parameter (U) is added to take care of the strong electron-electron interaction. The on-site U parameter describes the effective electron-electron interaction (Coulomb interaction) in a solid state environment. With a proper choice of the U parameter, a more accurate electronic band structure can be reproduced or predicted.

1.2.5 Calculation of the Hubbard U parameter

The U parameter is dependent on the atom and the electronic configuration. It is known that the spatial extent of the d and f wave function changes with an increasing number of d and f electrons [49]. U is mathematically defined as the sum of the energy differences between two excited configurations, d^{n+1}, d^{n-1} and the ground state d^n. The energy required for this reaction is

$$U = E(n_d + 1) + E(n_d - 1) - 2E(n_d), \tag{1.31}$$

where, E is the Coulomb energy of the d orbital. The inter-electronic interactions of the d electrons are taken into account by adding a term, $E^U = \frac{1}{2} U \sum_{i \neq j} n_i n_j$, in the Hamiltonian. Here, $n_i n_j$ ($n = 0$ or 1) represent the occupancies of the ith and j^{th} localized d orbital. Therefore, the total energy of a system is written as

$$E^{DFT+U} = E^{DFT} + E^U - E^{dc}. \tag{1.32}$$

Since E^{DFT} is contained in part of E^U already, in order to avoid double counting their contribution, the energies of these orbitals should be removed. Hence, these overlaps are removed from the total energy by taking into account this term. The last term in Eq. (1.32) is the 'double counted' term which is equal to the on-site LDA contribution to the total energy. E^{dc} is expressed as the mean-

field value of the Hubbard term U, thereby allowing one to write the mean value of E^{dc} and neglected orbital polarization effects as

$$E^{dc}(n_d) = \frac{1}{2}UN_d(N_d - 1) - \frac{1}{2}JN_d(N_d - 1), \qquad (1.33)$$

where $N_d = \sum_i n_i$ is the total number of d electrons. The on-site exchange parameter J can be determined by fitting the Eq. (1.33) for the electron-electron interaction to the result of constrained Local Spin-density Approximation LSDA calculations [49]. This new addition to the one electron Hamiltonian improves the results significantly.

1.2.6 Periodic Boundary Conditions

The total number of particles in a solid, including the nuclei and electrons, is of the order of Avogadro's number (6.022 x 10^{23}). The one-electron wave functions are supposed to extend for the whole systems, thus the basis sets needed for the expansion of the Kohn Sham orbitals should ideally be infinite. However, a crystal structure consists of repetitions of identical units which in turn consist of electrons and nuclei. This enables one to use Periodic Boundary Conditions (PBC) and Bloch's Theorem [50]. We start with the periodicity of the potential and the eventual solution of the single particle Schrödinger equation in the presence of this potential taking the form of Bloch wave functions

$$\psi_n(\vec{k}, \vec{r}) = e^{i\vec{k}.\vec{r}} u_n(\vec{k}, \vec{r}). \qquad (1.34)$$

Since for any lattice vector $\boldsymbol{R}$, $u_n(\vec{k}, \vec{r}) = u_n(\vec{k}, \vec{r} + \vec{R})$ is a periodic function, the above equation above can be rewritten as

$$\psi_n(\vec{k}, \vec{r} + \vec{R}) = e^{i\vec{k}.\vec{r}} \psi_n(\vec{k}, \vec{r}). \qquad (1.35)$$

In the above equation, n is the band index, $\vec{k}$ is the wave vector of the electron in the first BZ. On substituting $\psi_j(\vec{k}, \vec{r} + \vec{R})$ into the KS equation, *i.e.* Eq. (1.15), a new set of eigen-equations are obtained for a given $\vec{k}$. The computation is thus made much more plausible by considering one electron rather than the order of Avogadro's number. The complete solution is given by simply multiplying a wave vector $\vec{k}$ to the phase factor of the solutions in a single reciprocal unit cell. Electronic wave functions at k points close to each other have similar results. Therefore, only a finite number of k points in a small region of the reciprocal lattice are required to determine the total energy of a solid, decreasing the computation load.

1.2.7 Plane Wave Basis Set

In order to solve the Kohn Sham equations, it is necessary to expand the KS orbitals using a particular basis set. Thus it is imperative to find a proper basis set to represent the KS orbitals. There are various options to be used as basis sets [51-53]. They have their own advantages and disadvantages. For a system in which periodic boundary conditions can be applied, the reciprocal space representation is more efficient, thus a plane wave (PW) basis set is a more obvious choice. Plane waves are exact eigenfunctions of the homogenous electron gas. An advantage of using PW basis sets is that they are independent of the atom type or positions. They are also easy to transform from the real to reciprocal space through fast Fourier transform (FFT). Plane waves form complete basis sets composed of simple mathematical functions. The completeness of basis sets can be controlled easily by adjusting only the kinetic energy cut-off, E_{cut}. Using the PW basis set, the single particle KS orbital in Eq. (1.34) can be expanded as:

$$\psi_i(\vec{k}, \vec{r}) = \sum_{\vec{G}} c_{i,\vec{G}+\vec{k}}(\vec{k}) \frac{1}{\sqrt{V}} e^{i(\vec{G}+\vec{k})\cdot\vec{r}}, \tag{1.36}$$

where $\vec{G}$ is the reciprocal lattice vector and is the coefficient of the PW basis set. The sum is the overall wave vectors (spatial frequencies) with the correct periodicity. Each wave vector represents a point in the reciprocal-space, and each Fourier basis function is a plane wave propagating in that space. In principle, an infinite number of plane waves are needed for the expansion. In practice, the plane wave basis sets are truncated to include only PWs that have kinetic energies smaller than E_{cut}, where

$$E_{cut} = \frac{1}{2}|\vec{k} + \vec{G}|^2. \tag{1.37}$$

1.2.8 The Pseudopotential Approximation

The core electrons of an atom, which are located close to the nucleus are highly localized due to the strong Coulomb attraction between the nucleus and electrons. On the other hand, the valence electrons are much more delocalized compared to the core electrons. In order to consider the contribution of all the electrons, their wavefunctions have to be expanded over plane wave basis sets. This expansion of the core wavefunctions requires a large number of plane waves. The rapid oscillations of the valence states in the core region due to the orthogonality with the core electrons, require more plane waves with higher kinetic energy. Many of the various properties of a material depend on the bonding of the atoms with the neighbouring atoms. Only the valence electrons take part in the bonding and thus allowing one to approximate the core electron interaction and ionic potentials with a pseudopotential which acts on a set of pseudo wave functions, rather than on the true valence wavefunctions. Thus, a high energy cut-off is not required for the plane wave expansion. Lesser number of plane waves will be needed to construct the KS orbitals and hence reduce the computational cost. The (pseudo)potential and pseudo-wave function and the all-electron counterpart must be identical outside the cut-off radius, r_c. These requirements are shown

schematically in Fig. 1.2. With the pseudopotential approximation, only valence electrons outside r_c are considered explicitly. The pseudo-wave functions in the core region are node-less. The cut-off radius must be properly chosen such that there is no overlap between the neighbouring atoms in the core regions.
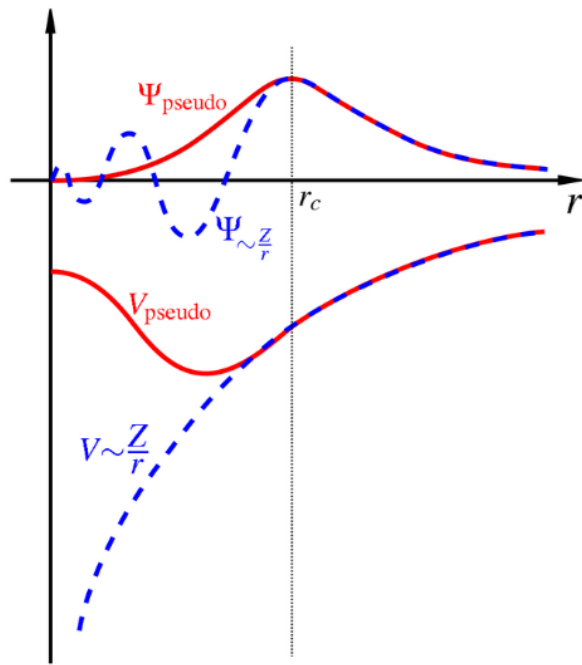
Figure 1.2 All-electron valence wave function and electronic potential (dashed blue lines) plotted against distance, r, from the atomic nucleus. The corresponding pseudo-wave function and potential is plotted (solid red lines). This figure has been taken from http://en.wikipedia.org/wiki/Pseudopotential.

In 1994, the all electron scheme called Projector Augmented Waves (PAW) was developed by Blöchl [54]. While it has the numerical advantages of pseudopotential methods but nevertheless retains the physics of all-electron calculations. The correct nodal behaviour of the valence-electron wave function is also represented. On adding all-electron partial waves to the total wave functions, the corresponding pseudo-waves need to be subtracted. Therefore, mathematically, the reconstructed all electron wave function is a sum of the pseudo-wave function outside the core

region and the all electron partial wave function inside the core region with the corresponding

pseudo partial wave function in the core region subtracted. The reconstructed KS wave function

can be written as

$$\psi_n(\vec{r}) = \tilde{\psi}_n(\vec{r}) - \sum_\alpha \tilde{\psi}_n^\alpha(\vec{r}) + \sum_\alpha \psi_n^\alpha(\vec{r}). \qquad (1.38)$$

1.2.9 Self-consistent Field Cycle

The ingredients needed to solve the KS equations have been described in the preceding

sections. The method of solving the KS equations will be described now. The ground-state electron

density and ground-state total energy can be solved self-consistently using the pseudopotential,

PAW method. The general algorithm is illustrated in the flow chart in Fig. 1.3. An initial electron

density, $\rho(r)$ is constructed from superposition of the electron densities of non-interacting atoms in

the system. Using the initial charge density, a set of KS equations including kinetic energy and V_{eff}

are constructed. At this point, the KS equations are solved at each specified and interpolated point

in the Brillouin Zone. The wave functions that are used are described by a finite set of plane waves

and are truncated at the kinetic energy cut-off, E_{cut}. On solving the KS equation, a new electron

density and potential are constructed. If the initially guessed charge density and the newly

calculated charge density are close to each other within a pre-set tolerance, it means that

convergence has been achieved and further calculations are stopped. If convergence is not

achieved, the new calculated charge density replaces the initial one and this self-consistent cycle

keeps running until convergence is achieved. This self-consistent method of solving the KS

equation has been illustrated in Fig. 1.3. The DFT calculations have been carried out using the

software, VASP, the Vienna *ab initio* Simulation Package [55-58], and the PAW potentials.

Initial Guess
$\rho(\mathbf{r})$

Calculate Effective Potential
$\upsilon_{\text{eff}}(\mathbf{r}) = V_{\text{en}}(\mathbf{r}) + \int \frac{\rho(\mathbf{r}')}{|\mathbf{r}-\mathbf{r}'|} d\mathbf{r}' + V_{\text{xc}}[\rho(\mathbf{r})]$

Solve Kohn-Sham Equations
$\left[-\frac{\hbar^2}{2m_e} \nabla_i^2 + \upsilon_{\text{eff}} \right] \psi_i = \varepsilon_i \, \psi_i$

Evaluate the Electron Density & Total Energy
$\rho(\mathbf{r}) = \sum_i |\psi_i(\mathbf{r})|^2 \rightarrow E_{\text{tot}}[\rho(\mathbf{r})] = \ldots$

Converged?

Output Quantities
$\rho_0(\mathbf{r}), \, E_i[\rho_0(\mathbf{r})] \rightarrow$ Forces, Eigenvalues, ...
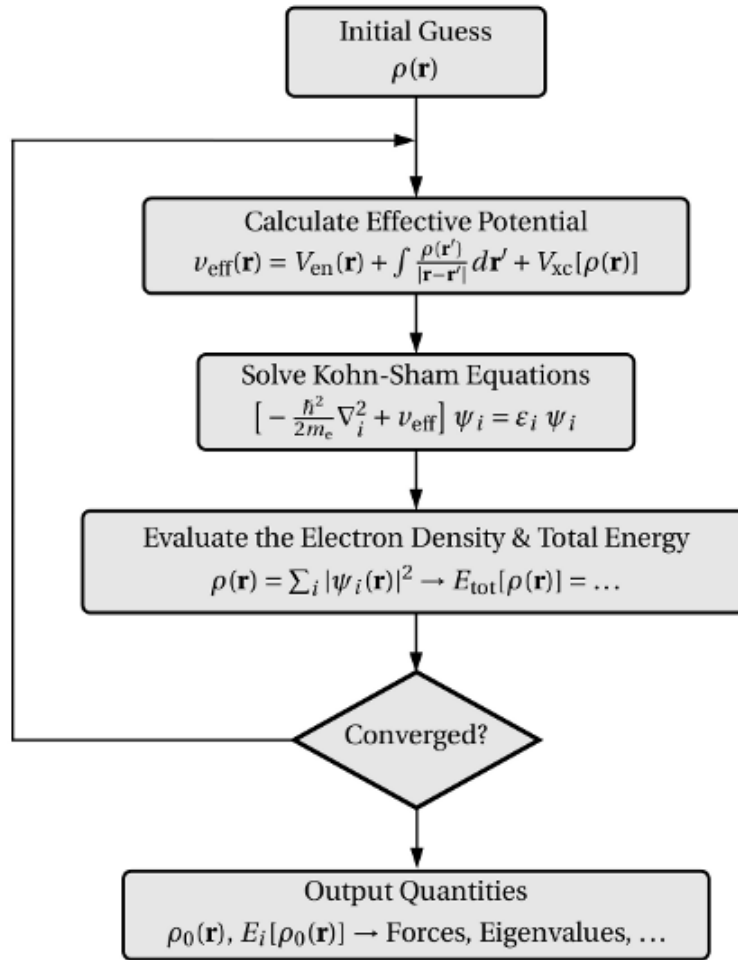
Figure 1.3 Step by step procedure of the working of the KS self-consistent calculation. This figure has been taken from http://www.iue.tuwien.ac.at/phd/goes/dissse14.html.

1.3 Molecular Dynamics

As described above, in DFT the primary concern is the electronic motion with respect to the potential energy surface (PES). The motion of the nuclei is not described using DFT. To improve material simulation, it is necessary is to describe the motion of the nuclei on the PES as well. Different atomic configurations correspond to different points on the PES. Since, every atom contains both electrons and a nucleus, the nuclear motion and configuration is also needed to completely describe the PES. The atomic configuration with the lowest energy is called the

thermodynamic ground state and is the global minimum. The mechanism behind the structural evolution of materials is contributed by the nuclear configuration and dynamics due to thermal and quantum effects. The method of molecular dynamics (MD) [27, 59-61] was used to study the movement of atoms on the PES at non zero temperature. Newtonian mechanics is employed to describe the motion of the nuclei which are treated as classical particles. MD simulations have been extensively used to investigate the structural, transport, and thermodynamic properties in materials science.

Due to the importance of the nuclear motion, MD provides us with both the positions and velocities of the nuclei. The macroscopic properties can be derived from these parameters. The mathematical space of these quantities is called the phase space. During the evolution of a system in time, the system goes through a series of such phase space points, collectively called an ensemble. The concept of ensemble is brought forward by statistical mechanics, which relates the macroscopic and thermodynamic properties (temperature, pressure, *etc.*) to the microscopic properties of the system. Using these fundamental thermodynamic quantities, further properties can be derived too. An ensemble has the same thermodynamic state but different microscopic states. The macroscopic thermodynamic properties are defined as an ensemble average, which is an average over a large number of micro states of the ensemble. Thus, an MD simulation generates a set of points in the phase space as a function of time according to the ensemble. The ergodic hypothesis states that the time average is equal to the ensemble average. The properties generated from the MD simulations are the time average of those respective quantities. In order to simulate real experimental conditions, any MD simulation needs to be performed under certain ensembles. The three commonly known ensembles are: microcanonical or *NVE* ensemble, canonical or *NVT* ensemble, and isothermal–isobaric or *NPT* ensemble. For each ensemble, the corresponding aforementioned thermodynamic variables are fixed during the MD simulation.

23

1.3.1 A Simple MD Program

Before we move onto the description of how an MD program works, we will present a general flowchart of a typical MD simulation as shown in Fig. 1.4. The flowchart gives a schematic of the MD algorithm.
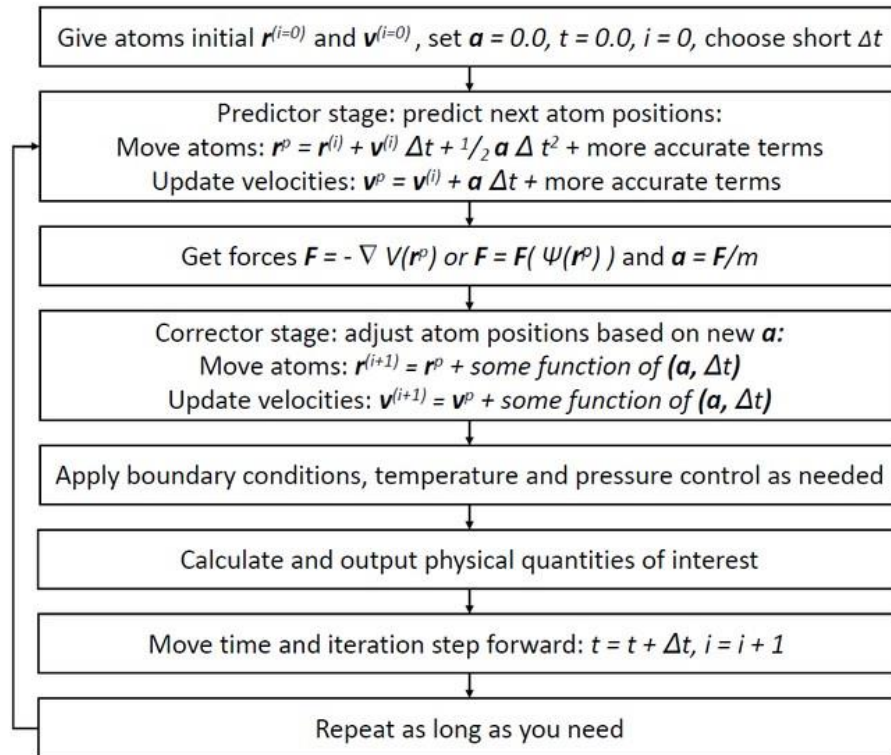
Figure 1.4 Schematic diagram of a basic MD code. This figure has been adapted from https://en.wikipedia.org/wiki/Molecular_dynamics.

As can be seen in the diagram in the first step, the initial positions and velocities at time $t = 0$ are defined. The initial velocities are set according to the Maxwellian distribution of equipartition relationship. Then the forces on each atom are calculated by taking the gradient of the electronic potential energy. Once the forces are obtained, one can integrate the Newton's equation of motion to get the positions and velocities. There are various algorithms that are used in MD. The two

commonly used algorithms for integration are, the Velocity Verlet (VV) algorithm and the Verlet Leapfrog (VF) algorithm. Both schemes can simultaneously evolve the velocity and position with time. The equations of the VV algorithm are written as:

$$\vec{v}_{n+1/2} = \vec{v}_n + \frac{\vec{f}_n \cdot \Delta t}{2m} \tag{1.39}$$

$$\vec{r}_{n+1} = \vec{r}_n + \vec{v}_{n+\frac{1}{2}} \cdot \Delta t \tag{1.40}$$

$$\vec{v}_{n+1} = \vec{v}_{n+1/2} + \frac{\vec{f}_{n+1} \cdot \Delta t}{2m} \tag{1.41}$$

The half-step velocity calculated from the force is used as the mean velocity between steps n and $n + 1$ to update the velocity and position. A similar approach is also used for the VF algorithm which also makes use of the half-step velocities. The velocity is given by,

$$\vec{v}_{n+1/2} = \vec{v}_{n-1} + \frac{\vec{f}_n \cdot \Delta t}{2m} . \tag{1.42}$$

The new position and velocity at the $(n+1)^{\text{th}}$ step is then given by,

$$\vec{r}_{n+1} = \vec{r}_n + \vec{v}_{n+1/2} \cdot \Delta t , \tag{1.43}$$

$$\vec{v}_{n+1} = \vec{v}_{n+1/2} + \vec{v}_{n-1/2} . \tag{1.44}$$

From MD, a time dependant trajectory of the atoms of the concerned system is determined from successive integration of the steps. The total time depends on the time required and set. Once the trajectory is obtained, exploiting the ergodic hypothesis, from the time average, many microscopic and macroscopic properties of the system are calculated. An MD calculation runs in a loop until the number of desired times steps in reached.

1.3.2 *Ab initio* Molecular Dynamics

The nuclei of most atoms can be treated as classical point-like particles, and their motions can be studied by Newton's laws; this forms the basis for classical MD. The forces on the atoms can be calculated quantum mechanically using the Hellmann-Feynman theorem, and this method is known as *ab initio* MD (AIMD). In AIMD the forces are calculated from the Hellmann-Feynman Theorem and is written as

$$\boldsymbol{F} = -\frac{dE}{d\vec{R}}, \tag{1.45}$$

where $\boldsymbol{R}$ is the nuclear spatial coordinate and the energy E can be obtained by solving the KS equations:

$$E = \langle \psi | H_e | \psi \rangle \tag{1.46}$$

From Newton's 2nd law and Eq. (1.45), one can get the Hellmann-Feynman force as:

$$\boldsymbol{F} = -\left\langle \psi \left| \frac{\partial H}{\partial \vec{R}_I} \right| \psi \right\rangle - \left\langle \frac{\partial \psi}{\partial \vec{R}_I} \left| H \right| \psi \right\rangle - \left\langle \psi \left| H \right| \frac{\partial \psi}{\partial \vec{R}_I} \right\rangle. \tag{1.47}$$

Since the ground state is the lowest energy state, it is the minimum point with respect to any variation of the wave function and thus the second and third terms vanish. This leads to an expression of the force on an ion, which is given by the expectation value of the gradient of the electronic Hamiltonian in the ground state. Once again, the AIMD simulations reported in this thesis were performed by using VASP.

1.4 Metadynamics

The science behind chemical reactions, phase transitions or protein folding was widely studied after the introduction of *ab initio* MD as discussed in the previous section. It bolstered the

predictive power of computational techniques by being able to identify possible new structures without any prior knowledge. However, standard MD is not efficient enough to simulate such processes due to the fact that many of the structural phase transitions are first order. In practice, such transitions are initiated by nucleation which start at the surface or structural defects. Due to the small systems used in simulations and mostly being perfect crystals, nucleation cannot be simulated. In reality, the structural defects occur naturally which pave the way for first order phase transitions reducing the transition barrier. But in computer simulations, the barrier which is high, requires a lot of energy to be crossed to the next global or local minimum. In order to overcome such high energy barriers, the system can be over pressurized and the contribution from the PV term increases the Gibb's potential. But such over pressurization leads to mechanical instability [62] and can also skip some of the intermediate metastable phases, thus missing out on more details about intermediate structures. This shortcoming was solved by Laio and Parrinello [63]. The metadynamics method enables the system to cross high free-energy barriers. This method employs biased potentials and adds them to the original free energy to lower the energy barrier and promote crossing. The biased potential, which is usually represented by a Gaussian function, is constructed from a few order parameters called collective variables (CV). The underlying principle of the metadynamics is illustrated in Fig. 1.5. In the illustration, the PES of the system is represented by the black curve. In Fig. 1.5b, it has been shown how Gaussians are added into the well to eventually give rise to an energy ladder which allows the system to reach the top of the potential well and descend into the next well. To give a cursory idea of the Gaussians filling up the potential well, approximate representations of the Gaussians have been shown in Fig. 1.5b, rather than showing the whole profile of the function. The local minima correspond to metastable phases. Thus, once a potential valley is filled, the other valleys can be explored.
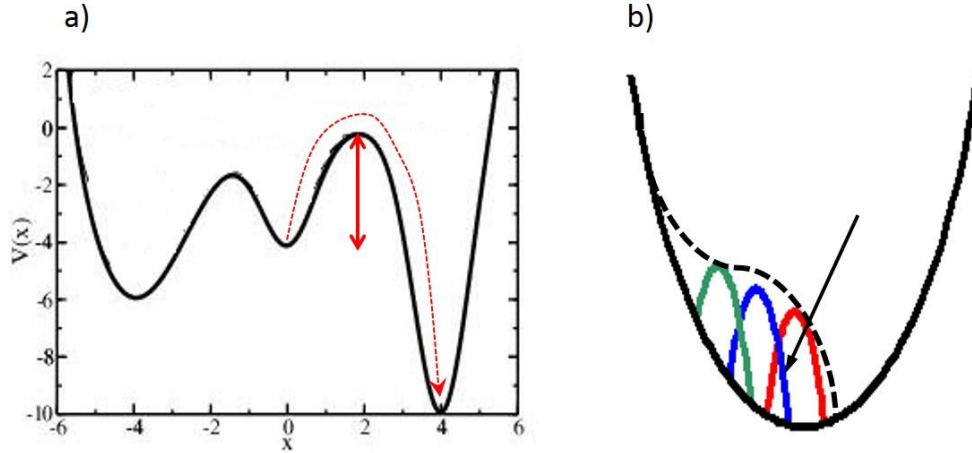
Figure 1.5 a) Underlying principle of the metadynamics method of crossing the energy barriers and b) Gaussians filling up a potential well to overcome the energy barrier (Courtesy Yansun Yao)

Different order parameters are chosen for specific properties. For metadynamics, the model box edges, $\mathbf{h} = (\mathbf{a},\mathbf{b},\mathbf{c})$ are chosen to be the order parameters arranged in the form of a 3×3 matrix. The $\mathbf{h}$ matrix contains the freedom of the cell parameters, the 3 cell lengths, 3 angles and 3 global rotations. Out of the 9 independent degrees of freedom (DOF), the 3 global rotations can be avoided by freezing them and thereby reducing the number of DOF to 6. The 3 global rotations are removed by constructing an upper triangular form of the $\mathbf{h}$ matrix. The evolution of this set of order parameters is written as:

$$\mathbf{h}^{t+1} = \mathbf{h}^t + \delta h \frac{\phi^t}{|\phi^t|} . \tag{1.48}$$

$\phi^t = -\frac{\partial G^t}{\partial \mathbf{h}}$ is the driving force, where G is the history-dependent Gibbs free energy. The Gibbs free energy is a function of the box edges, such that on varying the box edges, a thermodynamic state is reached. In order to avoid bringing the system to a state already traversed through, a

Gaussian function is added to the point already passed. Hence, the term history-dependent has been used. This history-dependent Gibbs potential is given as:

$$G^t(h) = G(h) + \sum_{t' < t} W e^{-\frac{|h - h^{t'}|^2}{2\delta h^2}} \ . \tag{1.49}$$

The force is then a sum of the thermodynamic forces. With the passage of time, this history-dependent potential fills up the valley and pushes the system out of the local minimum into the next minimum, which can be local or global. Each such minimum represents a phase which is either meta stable or the ground state. Thus, using metadynamics, one can traverse the whole energy contours, searching for the ground state configuration of the atoms. In the works presented in this thesis, the metadynamics simulations were carried out using the metadynamics code introduced by Martoňák *et al.* [64-65] interfaced with VASP.

1.5 Superconductivity

1.5.1 Qualitative Description of BCS Theory

Superconductivity, the property of a material to have negligible electrical resistance, is a many-body phenomenon in which the quantum coherence effects are manifested at the macroscopic scale. The first successful theory of superconducting states was put forward by Bardeen, Cooper and Schrieffer (BCS) [66]. The underlying concept of the BCS theory is that electrons with opposite momenta and spins close to the Fermi level form a pair, known as Cooper pair [67]. The mechanism of the formation of Cooper pairs is as follows. When an electron moves through a lattice, there is a lattice distortion with the positive charges crowding more around the moving electron, thus increasing the net positive charge density in that particular region. This positive charge cloud attracts any other electron in close proximity. Thus, pairing of electrons is

caused by small attractive interactions resulting from coupling with lattice vibrations. This attractive interaction, is called the Electron Phonon Coupling (EPC). If the strength of EPC is more than that of electron-screened Coulomb repulsion, then the resultant interaction between the electrons is attractive and superconductivity occurs. Such pairs of electrons move in a single coherent motion, giving rise to ideally zero electrical resistance in the material. This gives rise to the formation of bound-pairs of electrons, eventually stabilizing the system by a second order transition to superconducting states. The three major ingredients in the BCS theory are EPC, Coulomb repulsion, and the instability at the Fermi surface. Fig. 1.6 gives a schematic representation of electron-phonon coupling, according to BCS theory.
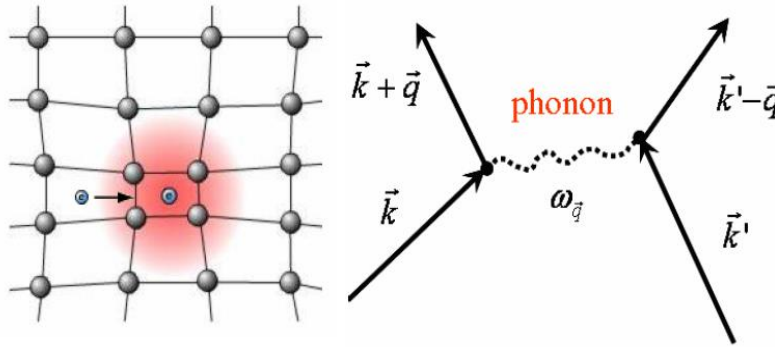
Figure 1.6 (Left) Formation of Cooper pair. A passing electron attracts ions which attract another electron. (Right) The interaction of two electrons with momenta $\vec{k}$ and $\vec{k}'$ that are coupled via exchange of a phonon. This figure has been taken from Ref. [68].

1.5.2 Superconducting Critical Temperature T_c from First Principles

In the strong coupling regime, the Migdal-Eliashberg theory [69-72] is an extension of the BCS theory. This theory relates the superconducting critical temperature to the underlying microscopic phenomena. In the Migdal-Eliashberg theory, the extent of the attractive electron-phonon interactions is quantified by the EPC parameter, λ. The electron-screened Coulomb

interaction, which is repulsive in nature is represented by the Coulomb pseudopotential, μ^*.

According to the Migdal-Eliashberg theory, the EPC is characterized for each phonon branch and

every phonon frequency. These are determined by the lattice dynamics of the material. A

comprehensive description of the superconducting state can be obtained from the Eliashberg

spectral function $\alpha^2 F(\omega)$ [73],

$$\alpha^2 F(\omega) = \frac{1}{2\pi N(\varepsilon_F)} \sum_{\vec{q}j} \frac{\gamma_{\vec{q}j}}{\omega_{\vec{q}j}} \delta\left(\omega - \omega_{q_j}\right) w(\vec{q}), \tag{1.50}$$

where $\omega_{\vec{q}j}$ is the phonon frequency of mode $(\vec{q}j)$ and $w(\vec{q})$ denotes the weight of phonon point $\vec{q}$

in the first BZ. $N(\varepsilon_F)$ is the DOS at the Fermi level ε_F. The phonon linewidth of mode $(\vec{q}j)$, is

given by

$$\gamma_{\vec{q}j} = 2\pi\omega_{\vec{q}j} \sum_{n,m} \int \frac{d\vec{k}}{\Omega_{BZ}} |g^j_{\vec{k}n,\vec{k}+\vec{q}m}|^2 \delta(\varepsilon_{\vec{k}n} - \varepsilon_F) \delta(\varepsilon_{\vec{k}+\vec{q}m} - \varepsilon_F), \tag{1.51}$$

where the volume integral is taken over the first BZ. The $\varepsilon_{\vec{k}n}$ and $\varepsilon_{\vec{k}+\vec{q}m}$ are the Kohn- Sham

eigenvalues with wavevectors $\vec{k}$ and $\vec{k}+\vec{q}$ in the nth and m^{th} band. The $g^j_{\vec{k}n,\vec{k}+\vec{q}m}$ is the electron-

phonon matrix element determined from the linearized self-consistent potential.

The Eliashberg spectral function $\alpha^2 F(\omega)$ provides with an understanding of which region

of the vibrational frequency spectrum contributes to the total EPC of the system. This quantity can

be measured by tunneling experiments. In theory, $\gamma_{\vec{q}j}$ and $\alpha^2 F(\omega)$ can be calculated from the EPC

strength $\lambda_{\vec{q}j}$ of each phonon mode $(\vec{q}j)$ by

$$\lambda_{\vec{q}j} = \frac{\gamma_{\vec{q}j}}{\pi\hbar N(\varepsilon_F)\omega^2_{\vec{q}j}}. \tag{1.52}$$

The attractive interaction in the system is represented by the EPC parameter λ, which is a weighted

average of $\alpha^2 F(\omega)$ over the entire vibrational regime,

$$\lambda = 2 \int_0^\infty \frac{\alpha^2 F(\omega)}{\omega} d\omega \approx \sum_{\vec{q}j} \lambda_{\vec{q}j} w(\vec{q}) . \qquad (1.53)$$

In Eq. (1.53), λ is approximated by a weighted average of $\lambda_{\vec{q}j}$ for all vibrational modes ($\vec{q}j$) in the first BZ where $\lambda_{\vec{q}j}$ is the EPC strength projected on each mode.

Once the $\alpha^2 F(\omega)$ and Coulomb pseudopotential μ^* are known, the superconducting critical temperature, T_c can be calculated by solving the Eliashberg gap equations. However, this is a cumbersome calculation. Therefore, McMillan constructed a simplified equation relating T_c and $\alpha^2 F(\omega)$, better known as the McMillan equation [74] in the field of superconductivity. The original form of the McMillan equation is

$$T_c = \frac{\omega_D}{1.45} exp\left(-\frac{1.04(1+\lambda)}{\lambda - \mu^*(1+0.62\lambda)}\right). \qquad (1.54)$$

Eq. (1.54) was found to work well for materials with $\lambda < 1.0$ but not for larger values of λ. Allen and Dynes introduced a successful modification of the McMillan equation [75-76], and this equation, known as the Allen-Dynes modification of the McMillan equation is given as follows,

$$T_c = \frac{\omega_{log}}{1.2} exp\left(-\frac{1.04(1+\lambda)}{\lambda - \mu^*(1+0.62\lambda)}\right), \qquad (1.55)$$

where ω_{log} is the logarithmic average of phonon frequency,

$$\omega_{log} = exp\left[\frac{2}{\lambda} \int_0^\infty \frac{d\omega}{\omega} \alpha^2 F(\omega) ln\omega\right]. \qquad (1.56)$$

The Allen-Dynes modification of the McMillan equation Eq. (1.54) is widely used equation for the estimation of T_c for materials that have an EPC parameter greater than one.

In order to calculate T_c from Eq. 1.55, λ and ω_{log}, can be obtained quite conveniently from the knowledge of $\alpha^2 F(\omega)$ (Eqs. (1.52) and (1.55)). The remaining term, *i.e.* the Coulomb pseudopotential μ^*, is approximated from a rescaled Coulomb repulsion parameter μ to include retardation effects [77] as follows:

$$\mu^* = \frac{\mu}{[1 + \mu \ln(T_F/\theta_D)]} , \tag{1.57}$$

where T_F and θ_D are the Fermi and Debye temperatures. The Coulomb repulsion parameter μ depends on the configuration of nuclei and is difficult to evaluate from first principles [78]. Thus an empirical value of μ^* between 0.10-0.13 is commonly used [79]. If the value of μ is not known, an approximate upper limit on μ^* can be calculated by setting μ to infinity [80, 81], and form elementary algebra, one can get the expression of μ^* as,

$$\mu^* = \frac{1}{\ln(T_F/\theta_D)} \tag{1.58}$$

The Debye temperature can be calculated from the semi-empirical equation [81]

$$\theta_D = 1.4 \frac{\hbar}{k_B} \sqrt{< \omega^2 >} , \tag{1.59}$$

where $<\omega^2>$ is defined as

$$< \omega^2 > = \frac{2}{\lambda} \int_0^\infty d\omega \, \omega \alpha^2 F(\omega) \tag{1.60}$$

In this thesis, the superconducting properties of selected high-pressure materials have been investigated using the Migdal-Eliashberg theory. The T_c of these materials was estimated using the Allen-Dynes modification of the McMillan equation Eq. (1.55). The vibrational frequency $\omega_{\vec{q}j}$, EPC strength $\lambda_{\vec{q}j}$, and Eliashberg spectral function $\alpha^2 F(\omega)$ were determined within the framework

of density functional perturbation theory (DFPT) using the electronic structure package Quantum

ESPRESSO [82].

1.6 Post Processing Methods

There are several dynamical properties that can be obtained from the trajectories gotten

from the MD simulations. Some of these properties are the autocorrelation function, mean squared

displacement, and pair correlation function, which can be calculated from the trajectory. Other

properties such as diffusion coefficient and coefficient of viscosity can be further computed from

the mean squared displacement and autocorrelation function, respectively.

1.6.1 Time-correlation Functions

The dynamics of a system can be described by the time correlation function. Time

correlation function describes the cause-and-effect relationship between two time-dependent

properties with the evolution of time. A time-correlation function, also known as the Green-Kubo

relation, is ideally independent of the time origin and is defined as:

$$C(t) = \lim_{\tau \to \infty} \frac{1}{\tau} \int_0^{\tau} A(t_0)B(t_0 + t)dt = \langle A(t_0)B(t_0 + t) \rangle. \qquad (1.61)$$

The $\langle ... \rangle$ term is the ensemble average, and A and B are the dynamic variables of interest (*e.g.*,

stress tensor, velocity, *etc.*). When A and B are the same variables, then C is called an auto-

correlation function. The auto-correlation function measures the extent to which $A(t_0+t)$ is

correlated to the initial value A at the beginning of the simulation. The value of correlation, C,

plotted as a function of time starts at a certain value and then decays to a lower value. This decay

is due to the interaction with the surroundings. One example of a time-dependent correlation

function is the stress autocorrelation function (SACF) as the stress is a direct manifestation of the

dynamics. For SACF, the *A(t)* in Eq. (1.61) is replaced with the stress tensor. At a chosen time origin t_0, the components of the stress tensor are $P_{XX}(t_0)$, $P_{YY}(t_0)$, $P_{ZZ}(t_0)$, $P_{XY}(t_0)$, $P_{YZ}(t_0)$ and $P_{ZX}(t_0)$. Since the stress in an equilibrium system exhibits periodic oscillations, the correlation Eq. (1.61) is expanded over a range of time. The process is then restarted to calculate another SACF, starting at a new time origin. In this way, one can compute a series of time frames and that can remove the erroneous dependence on the time origins. In our work, the SACF, $C(t)$ is calculated as

$$C(t) = \lim_{\tau \to \infty} \frac{1}{\tau} \int_0^\tau \langle P(0)P(t) \rangle dt \tag{1.62}$$

Since the stress in system is related to the force, the study of SACF can reveal interactions in a system. From SACF one can obtain other important dynamical properties of the system. Assuming that the SACF decays to zero, we can calculate the coefficient of viscosity, η, from numerical integration:

$$\eta = \frac{V}{k_B T} \lim_{\tau \to \infty} \frac{1}{\tau} \int_0^\tau \langle P(0)P(t) \rangle dt \,, \tag{1.63}$$

where *V* is the volume of the system, *T* is the absolute temperature and k_B is the Boltzmann constant. Although, here the focus is on the viscosity, first-principles calculations is plausible for other transport coefficients too such as the thermal conductivity, chemical inter-diffusion coefficients, *etc.* all of which contribute to the attenuation of sound in fluids.

1.6.2 Mean Squared Displacement

From an MD trajectory, it is possible to obtain information on how far an individual particle moves by calculating the mean squared displacement (MSD). MSD is defined as the square of the distance a particle has moved from its starting point within a time interval, *t*:

$$MSD = \langle |\vec{r}(t) - \vec{r}(0)|^2 \rangle \tag{1.63}$$

For a liquid, the plot of MSD against time is linear with a finite slope. It is possible to get the diffusion coefficient, D, from this slope. As propounded by Albert Einstein, the MSD is related to the diffusion coefficient of an *'N'* dimensional system as follows:

$$D = \frac{1}{2N}\frac{d}{dt}\langle|\vec{r}(t) - \vec{r}(0)|^2\rangle \qquad (1.64)$$

where $N = 1,2$ or 3.

1.6.3 Pair Correlation Function

Pair correlation function, also called radial distribution function (RDF), *g(r)* gives an estimate as to how the density varies as a function of the distance from a reference particle. Thus, it represents how atoms are radially packed around each other. It is one of the quantities that can be directly compared with experimental data. The RDF is defined as,

$$g_{\alpha\beta}(r) = \frac{dn_{\alpha\beta}(r)}{4\pi r^2 dr\, \rho_\alpha}, \qquad (1.65)$$

where $\rho_\alpha = \frac{N_\alpha}{V}$ is the number density of the particles of type α. V is the volume of the system. In Eq. (1.65), $dn_{\alpha\beta}(r)$ is the number of β atoms around α atoms within a radial distance of r and $r +$ *dr*. The RDF is plotted with respect to the radial distance, *r*. The position of the first peak indicates the distance of the nearest neighbour from the reference atom. In between r = 0 and the first peak, the RDF is equal to 0. This is a consequence of the 'hard sphere radius' of the atom, disabling the pair of atoms from approaching very close. The long-range interactions can also be determined from the peaks which are located at larger values of the radial distance. The peaks of a solid are always sharp whereas for a liquid, they are much broader due to the randomness. An example of the radial distribution function is given in Fig. 1.7. In Fig. 1.7b, the first peak in the RDF corresponds to the nearest neighbours while the broader second peak represents the more loosely packed second nearest neighbours.
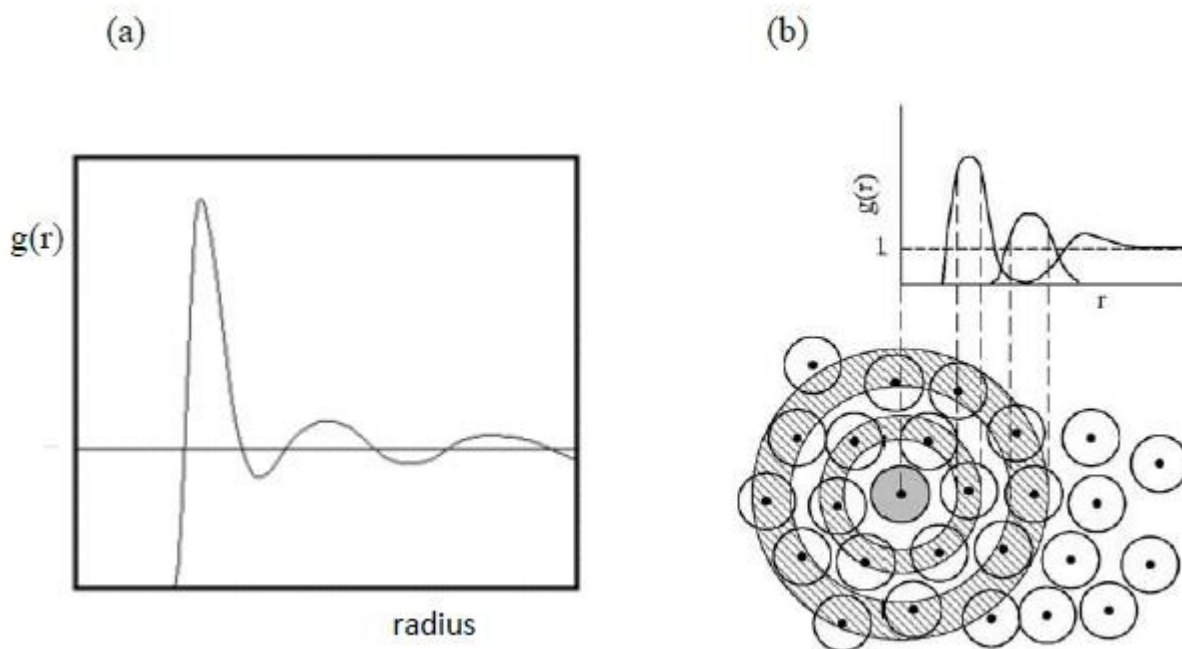
Figure 1.7 (a) Typical RDF of a liquid system. (b) Schematic diagram of a two-dimensional fluid and its corresponding RDF. This figure is adopted from Ref. [83].

1.7 Description of the Thesis

The aim of this thesis work is to predict and find out the various properties of novel materials using computational techniques. All the materials that have been discussed in this thesis were subjected to high pressure to discover any new phases with new characteristics. We have primarily studied structural phase transitions of crystalline as well as amorphous substances at high pressures and their thermodynamic, electronic and superconducting properties. The structural relaxations, molecular dynamics and electronic properties calculations were carried out using the Vienna *ab initio* Simulation Package (VASP). The phonons using linear response, vibrational properties and superconducting properties were determined using Quantum ESPRESSO.

Chapter 2 presents the results of a first order structural phase transition of aluminium triiodide (AlI_3) on compression, otherwise not reported in a recent experimental study. A high pressure monoclinic phase is predicted to exist above 1.3 GPa accompanied with a coordination change of aluminium. The coordination change resulted in the transformation from the ambient pressure 4-coordinated primitive monoclinic phase with space group *P2₁/c* to the monoclinic 6-coordinated structure with space group *C2/m*. Infrared effective charge intensities and Raman scattering tensors were obtained to characterize its spectroscopic properties. First-principles metadynamics simulations were employed to reconstruct this phase transition and provide the mechanism details for energetically favourable path from the ambient pressure *P2₁/c* structure to the predicted *C2/m* structure.

Chapter 3 presents the results of an extremely relevant and debated contemporary topic. In 2015, the superconducting phase of hydrogen sulfide (H_2S) was discovered at a pressure close to 200 GPa with a critical temperature of 203 K. Due to the lack of knowledge of the exact atomic structure which was responsible for this phase, many studies, both experimental and theoretical were carried out. In our study, we employed metadynamics at various high pressures and different temperatures to study the transition pathway and to find the desired structure. As expected, the compression pathway was responsible for different metastable structures. Out of the different structures we found, we reported a new structure whose simulated X-Ray diffraction (XRD) pattern matched well with the experimental finding. Further, superconductivity calculations were also carried out on this new structure whose results are consistent with that observed in experiment.

Chapter 4 deals with the superconductivity of the newly synthesized material, FeH_5 at 130 GPa and 200 GPa. The atomic nature of hydrogen in this structure sparked the interest to study the superconductivity as a high superconducting critical temperature was expected. But, contrary to the expectation, the critical temperature was not as high and a theory was put forward for our

observation. The theoretical conjecture that has been put forward in this chapter relates the phonon dispersion spectrum and the superconducting properties.

Chapter 5 presents an extensive study of Basalt at lower mantle conditions. In this chapter, we study both the glass and melt form of Basalt. Using *ab initio* molecular dynamics, the basalt was subjected to computational simulations at various high pressures. The phase transition, coordination change of the atoms and the transitions of the bulk modulus, density, velocity of sound, diffusion coefficient have been reported. Indeed, similar to other silicate glasses and melts, basalt also showed structural phase transitions at the similar pressure regions. The Si-O and Al-O coordination numbers increased as expected from 4 to 6. Various thermodynamic and transport properties have been reported for the different pressures.

Chapter 6 is an overall summary of the work that I carried out for my doctoral studies. It also addresses the prospective work that can be undertaken in the future.

Most of the work presented in this thesis has now been published in peer-reviewed journals or submitted for publication. The references are as follows:

1) Arnab Majumdar, Dennis D. Klug, and Yansun Yao, High Pressure Structural Changes in Aluminium Triiodide: A First Principles Study, *J. Chem. Phys*. **144**, 124507 (2016).

2) Arnab Majumdar, John S. Tse, and Yansun Yao, Modulated Structure Calculated for Superconducting Hydrogen Sulfide, *Angew. Chem. Int. Ed.*, **56**, 11390 (2017).

3) Arnab Majumdar, John S. Tse, and Yansun Yao, Superconductivity in FeH_5, *Phys. Rev. B* **96**, 201107 (2017).

4) Arnab Majumdar, John S. Tse, and Yansun Yao, Transformation and Superconductivity from a Molecular to Modulated Structure of Hydrogen Sulfide at High Pressure (Submitted).

A few other studies have also been published in which I contributed as a secondary author. These papers although have not been added as chapters in this thesis, but have been listed below to give an essence to the readers about the focus of our research group and the techniques and class of materials studied.

- Michael J. Greschner, Meng Zhang, Arnab Majumdar, Hanyu Liu, Feg Peng, John S. Tse, and Yansun Yao, A New Allotrope of Nitrogen as High-Energy Density Material, *J. Phys. Chem. A*, **120**, 2920 (2016).

- Shuangshuang Zhu, Feng Peng, Hanyu Liu, Arnab Majumdar, Tao Gao, and Yansun Yao, Stable Calcium Nitrides at Ambient and High Pressures, *Inorg. Chem.*, 55, 7550 (2016).

- Yansun Yao, Elissaios Stavrou, Alexander Goncharov, Arnab Majumdar, Hui Wang, Vitali Prakapenka, Albert Epshteyn, and Andrew Purdy, High-pressure Phase Transition of Alkali Metal−Transition Metal Deuteride Li_2PdD_2, *J. Chem. Phys*, **146**, 234506 (2017).

- Adebayo A. Adeleke, Michael J. Greschner, Arnab Majumdar, Biao Wan, Hanyu Liu, Zhiping Li, Huiyang Gou, and Yansun Yao, New single-bonded high-pressure allotrope of nitrogen, *Phys. Rev. B* **96**, 224104 (2017).

CHAPTER 2

STRUCTURAL CHANGES IN ALUMINIUM TRIIODIDE UNDER HIGH PRESSURE: A FIRST PRINCIPLES STUDY

A similar version of this chapter has been published as a research article in the Journal of Chemical Physics. The reference is as follows.

- Arnab Majumdar, Dennis D. Klug, and Yansun Yao, "High Pressure Structural Changes in Aluminium Triiodide: A First Principles Study", *J. Chem. Phys*. 144, 124507 (2016).

It has always been interesting to study the various properties of materials at extreme conditions like extreme temperatures and pressures. The reason for this interest lies in the fact that under different conditions, materials often show drastically different properties than what they possess at ambient conditions. On exerting pressure, mechanical work is done on the system (PΔV) which increases the enthalpy of the system. This additional energy is capable of overcoming energy barriers (bond energy) and leading to breaking of existing bonds and rearranging the atoms to new positions. Thus, structural phase transition occurs under high pressure. Therefore, high pressure *i.e.* a large amount of compression, leads to instability and further phase transition to a new structure. This new structure might have completely different electronic, optical, thermal, *etc.* properties owing to the new atomic arrangements. Even today it is not always possible to reach very high pressures experimentally but the compression process can be simulated on a computer quite easily. In this chapter the structural phase transition of the material that we have studied in detail is Aluminium triiodide (AlI_3). The ambient condition AlI_3 has been compressed and the compressed structure was subjected to *ab initio* metadynamics simulations to study the change in enthalpy if any, thus confirming structural phase transition of AlI_3 at high pressures. To confirm

our findings, the Raman activity was also calculated. Furthermore, the electronic structures were studied too, to see how the electronic properties change with pressure.

2.1 Introduction

Metal halides are a subject of interest as they offer a wide range of applications for example in the battery industry, solar cells, *etc*. Aluminum halides have gained recent attention due to the interest in studies of its structure both in the gas phase and in the solid form under high pressure [84-85]. Due to its wide range of applications, widespread research in the domain of aluminium halides has been conducted. Some of these applications include the use of aluminium bromide in water treatment, the usage of Aluminium bromide and chloride as catalysts in Friedel-Crafts Alkylation reactions and so on [86]. The introduction of the gas-phase electron diffraction (GED), gave way for gaseous aluminium halides to be extensively studied [84, 87-89]. Similar to other metal halides, aluminium halides have numerous applications too. For example, aluminium triiodide (AlI_3) is used in the first stages of the synthesis of AlN, a ceramic material with high thermal conductivity [90-91].

In the gaseous phase, the structures of aluminium halides are difficult to decipher by GED due to the presence of both monomeric and dimeric species. Intuitively, one can understand the structure of aluminium halides by the electronegativity of the halogens and the cation-to-anion radius ratio [85]. For example, the smaller anionic radii of fluorine and chlorine (1.15 Å and 1.67 Å) give way to the formation of 6 coordinated AlX_6 octahedrons in solid AlF_3 and $AlCl_3$ [92-93]. Bromine and iodine, on the other hand, have larger anionic radii (1.82 Å and 2.06 Å), which only enable the formation of 4 fold coordinated AlX_4 tetrahedrons in solid $AlBr_3$ and AlI_3 [92-93]. As already pointed out, in the vapor phase, aluminium halides can exist either as monomers (AlF_3), or

42

dimers (Al_2Cl_6, Al_2Br_6, and Al_2I_6), which decompose into monomers at high temperatures ($AlCl_3$, $AlBr_3$, and AlI_3) [84]. Both AlI_3 and $AlBr_3$ exist as molecular solids at ambient conditions [94-95]. They both contain double-bridged dimers, which can be viewed as pairs of AlX_4 tetrahedrons connected through a common shared edge (Fig. 2.1). In the rest of the chapter, in all the diagrams showing crystal structures, the pink spheres are Al atoms while the brown spheres denote I atoms. In the solid state, the halogen atoms are close-packed, forming a (distorted) hexagonal close packed (HCP) lattice as in $AlBr_3$ or a (distorted) face centered cubic (FCC) lattice as in AlI_3. In both the cases Al occupies 1/6 of the tetrahedral voids. Yao *et al*. suggested that on being compressed (*ca.* 0.4 GPa), $AlBr_3$ would transform from the dimer-based molecular crystal to a polymeric phase. In this phase transition the sp^3 bonded $AlBr_4$ tetrahedra would rearrange into extended arrays of $AlBr_6$ octahedrons [96]. At ambient conditions, AlI_3 crystallizes into a monoclinic structure (SG: P121/c1 (14)) with four formula units per unit cell [94]. In this structure, sharing of a common edge between two AlI_4 tetrahedrons gives rise to Al_2I_6 dimers. The bridging bonds are longer than the terminal Al-I bonds. A thorough inspection of this structure shows that the distorted FCC sublattice is formed by the iodine atoms, with cell distances and angles at near-to-ideal cubic values. Yet, $AlBr_3$ crystallizes in the same structure type, with the Br atoms forming a distorted HCP sublattice [95].
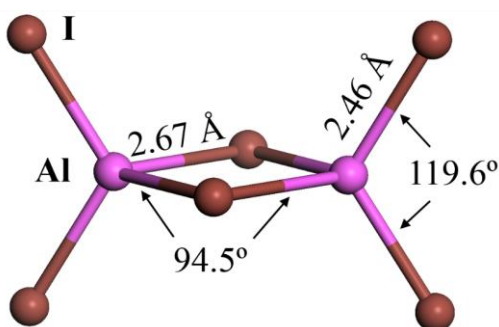
Figure 2.1 *P2₁/c* dimer structure of Al_2I_6 at ambient pressure. The bond angles and lengths indicated are those of the gas phase.

43

In this chapter, we report the investigation of crystalline AlI_3 at high pressure. Owing to the chemical similarity of iodine and bromine, a similar trend of high-pressure phase transitions like $AlBr_3$ may be expected for AlI_3 as well. Density functional based structural predictions, phonon and Raman spectra calculations along with first principles metadynamics simulations have been carried out to characterize the structural changes in AlI_3 under high pressure. In an experiment carried out by Stavrou *et al*. [85], the researchers suggested that an isostructural rearrangement of the monoclinically distorted FCC lattice of I atoms at ambient pressure to a standard FCC is possibly occurring in AlI_3 under high pressure. But the experimental equation of states indicates a sudden unexplained volume drop near 5 GPa that could probably have its explanation originating from the re-coordination of Al in the FCC lattice. This possible phase transition has been verified by us in this study. The Raman spectrum calculated also vouches for phase transition as will be discussed in section 2.3.1.

2.2 Computational Method

All the calculations in this study were done within the framework of Density Functional Theory (DFT) [97] by solving the Kohn-Sham equations [23]. The Vienna *ab initio* Simulation Package (VASP) [55] was employed to optimize the structures and obtain the enthalpies, pressure-volume relation, and hence the equation of state of AlI_3. For the pseudopotentials, the projector-augmented-plane wave (PAW) [54, 98] potentials were used. The Al and I potentials were considered with valence states of $3s^2 3p^1$ and $5s^2 5p^5$ utilizing the Perdew-Burke-Ernzerhof [46] exchange correlational functional and an energy cutoff of 240.3 eV. The Brillouin zone was sampled by using a 6×6×6 Monkhorst Pack k-point mesh [99]. Mechanical stability of the predicted structure was determined by phonon calculations using a finite displacement approach through a

combination of VASP and PHON [100] programs. These calculations were done with a 2×4×4 supercell and a 2×2×1 k-point mesh to obtain accurate interatomic forces. In order to study the phase transition, metadynamics [64-65] simulations were carried out in supercells with 8 AlI_3 units with a $2 \times 2 \times 2$ k-point mesh for Brillouin zone sampling. Each metastep consisted of a molecular dynamics (MD) simulation using VASP and the canonical (NVT) ensemble for a simulation time of 0.4 ps. Calculations of the Born effective charges for infrared activity were obtained with the ABINIT code [101] employing density functional perturbation theory (DFPT) from second-order derivatives of the energy. Calculations of the Raman spectrum and Raman tensors were obtained with DFPT [102] using Troullier-Martins-type pseudopotentials [103] with an $8 \times 8 \times 8$ k-point mesh sampling [99] of the Brillouin zone from the evaluation of the third-order derivatives of the energy.

2.3 Results

2.3.1 Structural Phase Transition

In order to compare which structure is energetically the most stable, different metal trihalide AX_3 structures have been considered in the present study as the candidate structures for AlI_3 at high pressure. These include the structures of GaX_3, BiX_3 [104-105], InX_3 [106-107], and BX_3 [108-110], as well as the predicted structures using the 'random search method' [111]. At 1 atm (ambient pressure), the experimentally known *P2₁/c* structure was found to be the most thermodynamically stable structure (Fig. 2.2). This structure consists of a distorted FCC lattice of iodine, which was also confirmed by Stavrou *et al*. [85] As expected for an FCC lattice, in Ref. [85], the authors reported that the iodine atoms are arranged in an ABCABC layer stacking, whereas the aluminium atoms occupy 1/6 of the tetrahedral sites and bond with adjacent iodine

atoms to form Al_2I_6 dimers. The aluminium atoms are 4-fold co-ordinated evident in the figure in which the dimers can be visualized as two AlI_4 tetrahedrons bonded along a common edge. With the same formula unit assignment, the same AlI_3 material with a hexagonal close-packed lattice of iodine (in the same *P2₁/c* space group) was also examined, which is the structure adopted by solid $AlBr_3$. This was done for confirmation and comparison of the energies of the two different structures with different iodine atom layer stacking. The two types of close-packed lattices (FCC and HCP) were found to have very similar energies, with the FCC slightly more favorable by a few meV/AlI_3. This similarity arises due to the very similar atomic density. Candidate structures consisting of Al_2I_6 dimers with other sequences of close-packing all have very similar calculated energies at 1 atm.
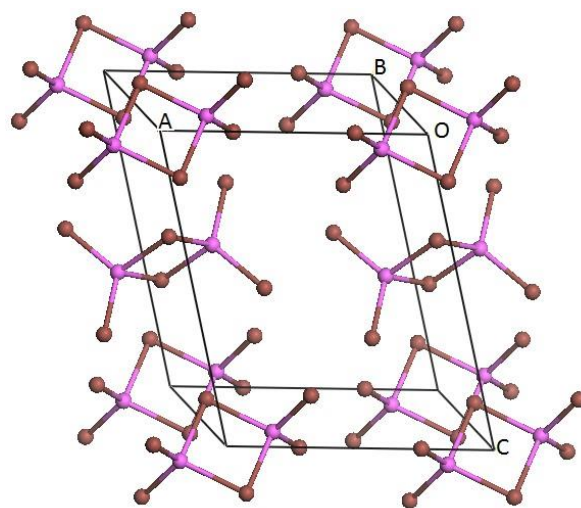
Figure 2.2 *P2₁/c* dimer structure of AlI_3 at ambient pressure. The pink spheres are Al atoms while the brown spheres denote I atoms.

Stavrou *et al*. [85] did not report any first-order phase transition of AlI_3 up to 50 GPa and rather suggested a second order continuous transition to an undistorted FCC lattice for the iodine atoms from the x-ray diffraction experiment. However, in our study, we identified a phase

transition at approximately 1.3 GPa. On reaching this pressure, a monoclinic $C2/m$ 6-fold coordinated structure, isostructural to solid $AlCl_3$ [112], was discovered to be more stable (Fig. 2.3).
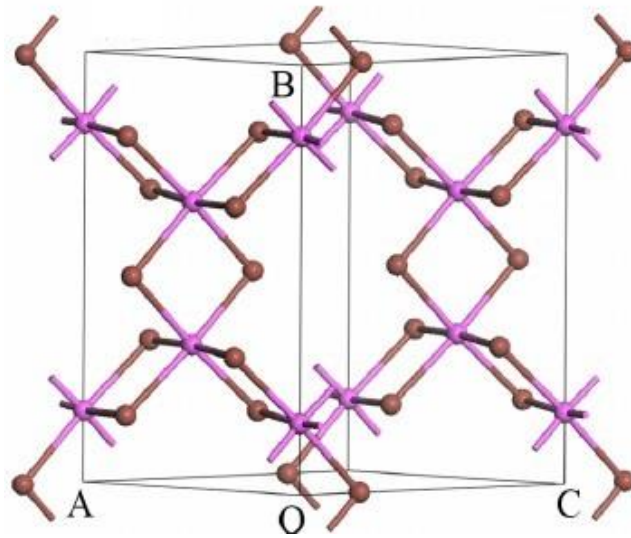
Figure 2.3 Polymerized $C2/m$ structure of AlI_3 at 2.4 GPa. The pink spheres are Al atoms while the brown spheres denote I atoms.

In the $C2/m$ structure, *i.e.*, after the structural phase transition from the $P2_1/c$ structure, the FCC lattice of iodine is retained but the aluminium atoms are now displaced to the octahedral sites. Due to the large size ratio of aluminium and iodine atoms, the iodine atoms dominate the x-ray diffraction (XRD) pattern. Since, both before and after the phase transition, the iodine atoms maintain the FCC sublattice, the x-ray diffraction patterns are similar, due to the fact that the diffraction patterns are mostly contributed by the iodine atoms. Therefore, from the XRD, no discernible profile difference was observed in the structures of AlI_3 at ambient and high pressures. However, a distinct discontinuity in the measured pressure-volume curve at approximately 4.3 GPa, indicate some structural changes. Using the predicted $C2/m$ structure as the high-pressure

phase, the discontinuity in volume can be well reproduced (Fig. 2.4), corroborating the theory of a

4-fold to 6-fold re-coordination of Al atoms.
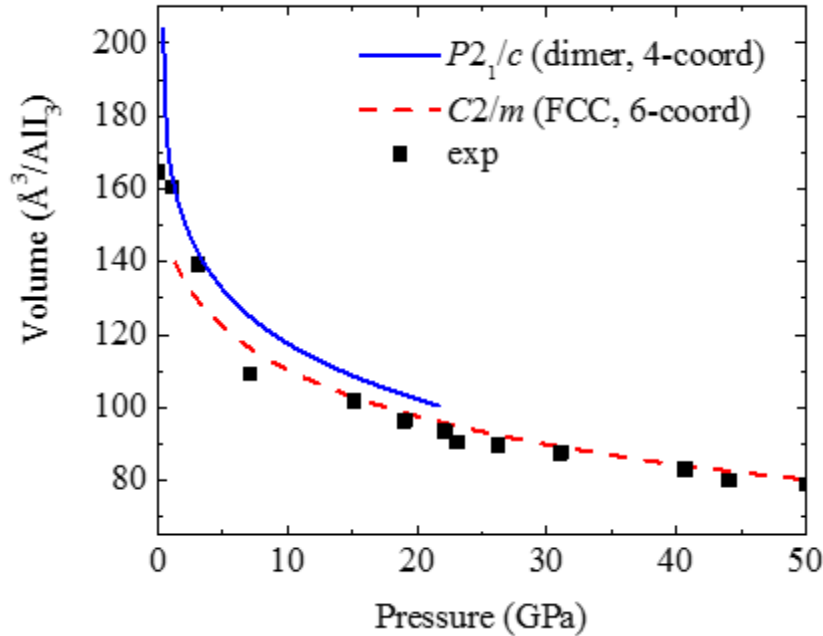
Figure 2.4 Calculated pressure-volume equations of state for the *P2₁/c* and *C2/m* structures compared with the experimental values. Experimental data were reported in Ref. [85].

Energetically, the enthalpy of the 6-fold *C2/m* structure becomes considerably lower than

that of the ambient 4-fold structure as the pressure is increased beyond the transition point (Fig.

2.5). For example, at 20 GPa, the *C2/m* structure is more stable than the *P2₁/c* structure by ~1

eV/AlI$_3$. Given such a large energy deficiency, it is therefore unlikely that the 4-fold structure can

be retained to 50 GPa. During the phase transition, the iodine atoms retain the FCC arrangement

but the aluminum atoms are expected to convert from their 4-fold coordinated environment to 6-

fold coordination and then occupy the octahedral sites as shown in Figs. 2.6a and 2.6b, and the

FCC sublattice of the iodine atoms is highlighted in red. On compressing the material, the

coordination number increases as inter-atomic distances decrease, leading to a loss of the sp^3

hybridization. The *d* orbitals of aluminium contributing towards the formation of 6-fold coordination. The 6-coordinated structures with the hexagonal close-packing of the iodine atoms are also energetically competitive to the FCC arrangement of the iodine atoms (Fig. 2.5), but they were found to have distinctly different diffraction patterns which were not observed in the experiment.
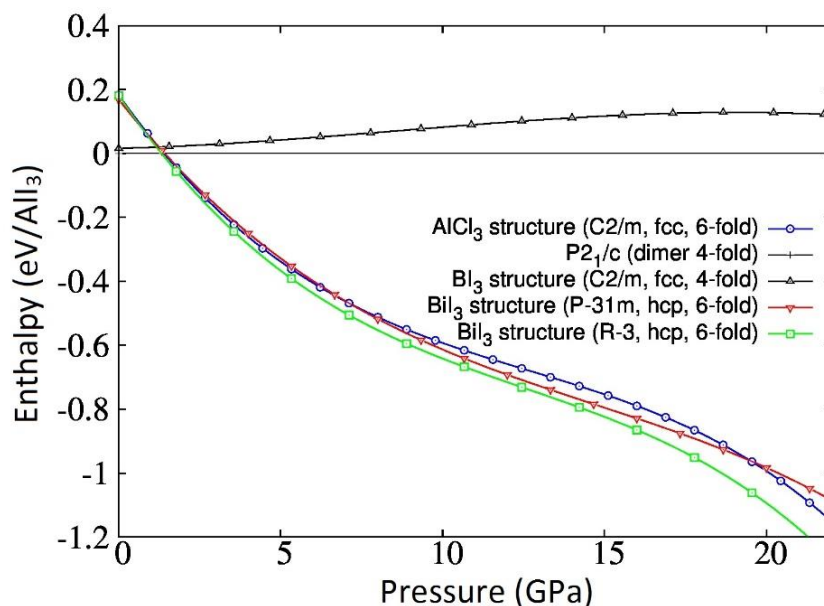
Figure 2.5 Enthalpy vs Pressure curve for the various structures of AlI_3. The 6-fold co-ordinated *C2/m* structure (blue open circle) is one of the most energetically competitive structures.
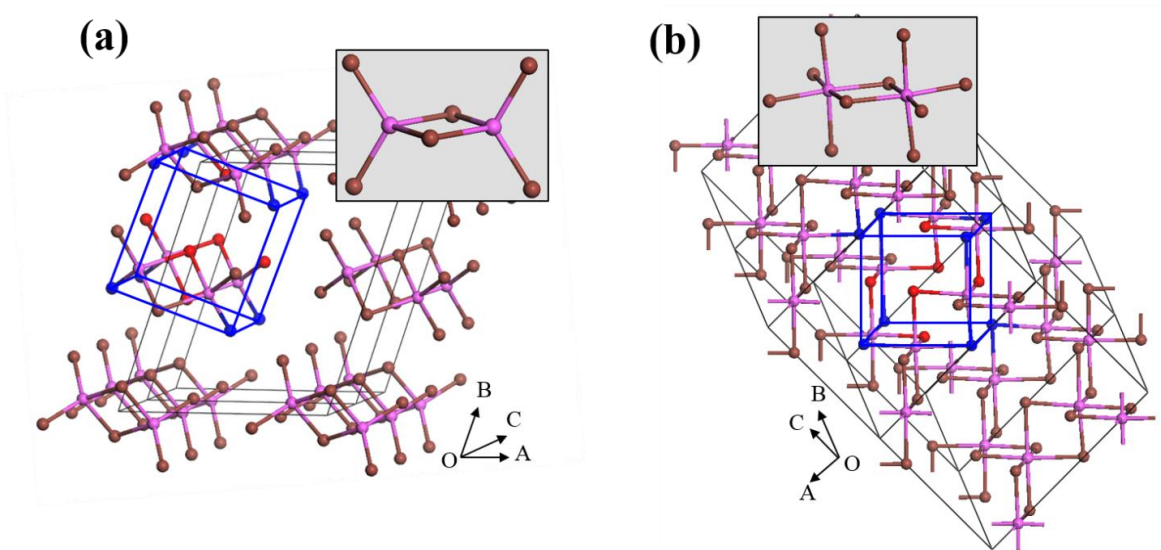
Figure 2.6 a) *P2₁/c* structure showing the tetrahedral position occupation of Al and b) *C2/m* structure showing the 6-fold co-ordination of Al in the octahedral position

From the present calculations, a volume drop of 9 percent after the phase transition is observed. After the transition to a *C2/m* structure the diffraction patterns from before and after the structural phase transition remain similar as the monoclinic angle approaches the high pressure value of 109.3˚ at 13.5 GPa from its calculated value of 144.6˚ at 5.3 GPa. The phonon band structures at approximately 20 GPa were calculated for all the structures and the *C2/m* (6-fold FCC) structure is shown to be dynamically stable (Fig. 2.7) providing a further support for the predicted *P2₁/c* → *C2/m* transition.
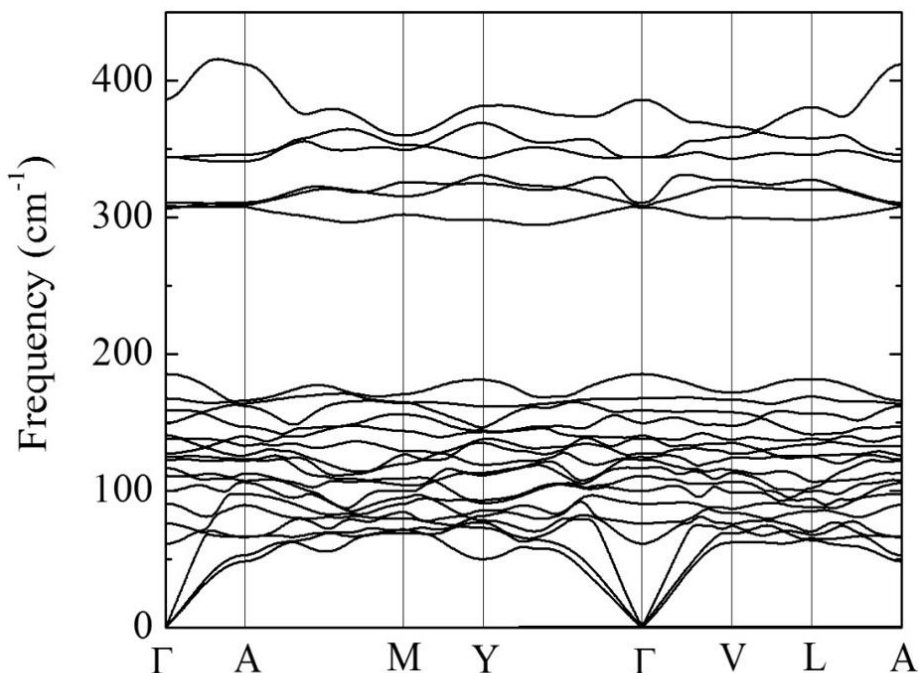
Figure 2.7 Phonon dispersion curve for the *C2/m* structure at 20 GPa.

The calculated phonon frequencies, Born effective charges for infrared activity and the Raman tensors for the *C2/m* structure provide additional predictions for experimental characterization of the predicted phase transition. Although both the *P2₁/c* and *C2/m* are monoclinic structures with a group-subgroup relationship, the *P2₁/c* structure will have essentially twice the number of vibrational modes including the three acoustic modes. All of the non-acoustic modes will be either infrared or Raman active for both of these structures. There are, for example at 4.8 GPa, 12 predicted Raman bands for the *C2/m* structure with the highest frequency Raman peak at 293 cm^{-1} and the strongest Raman peak at 149 cm^{-1} with its scattering intensity about 20 times greater for a randomly oriented powder sample than the next strongest Raman band at 104 cm^{-1}. There are infrared active modes up to about 365 cm^{-1} predicted with the strongest infrared bands at about 254 and 365 cm^{-1}. The *P2₁/c* structure in contrast will have its strongest Raman band at about

140 cm^{-1} at ambient pressure and is predicted to have many more infrared active modes as a result of the increased number of spectroscopically active modes for this symmetry. Table A1 (appendix) lists the calculated Born effective charges and Raman intensities for the predicted high-pressure *C2/m* structure at 4.8 GPa.

The pressure-induced phase transitions were simulated by employing metadynamics algorithms combined with *ab initio* molecular dynamics to examine the potential energy surface of AlI$_3$. The temperature was set to 300 K for the simulation along with several pressure conditions. The initial *P2$_1$/c* structure was taken as the starting structure and on running metadynamics simulation, the system was seen to be proceeding to nearby energy minima in potential energy surface along the low-energy pathway. This enabled the direct simulation of pressure-induced structural transformations of AlI$_3$ treading along all the pathways via several intermediate structures. The metadynamics simulation employed a Gaussian height of 225 kbar Å^3 and width of (15 kbar Å^3)$^{1/2}$. The simulation revealed a distinct phase transition at 22 GPa and 300 K (Fig. 2.8). The system was over pressurized to accelerate the phase transition. At the beginning of the simulation, the system undergoes primarily thermal vibrations, where the enthalpy stays nearly constant (metasteps 1-78).
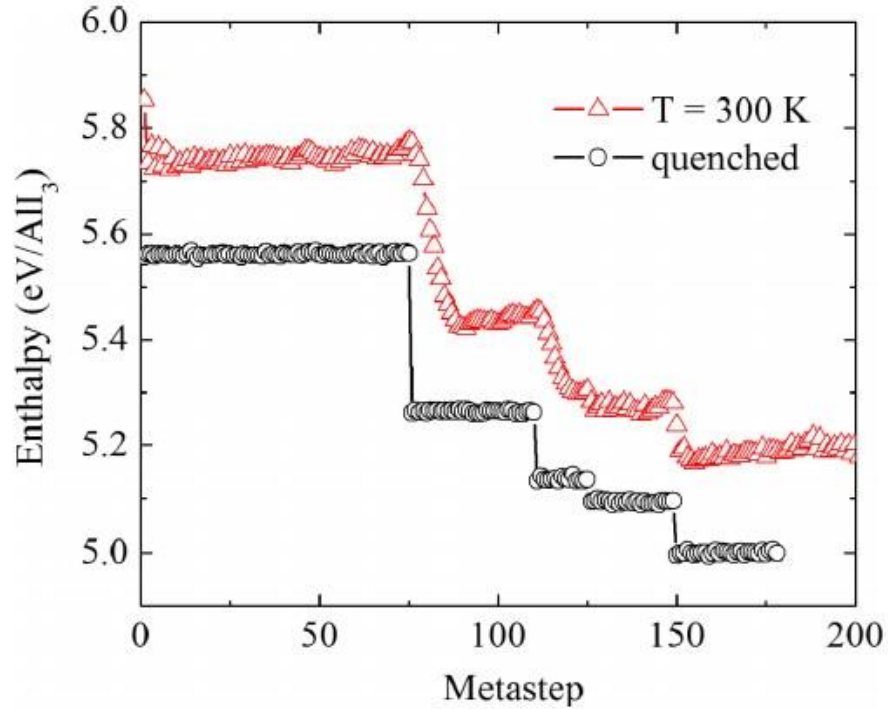
Figure 2.8 Metadynamics simulation at 22 GPa and 300 K showing the evolution of the enthalpy starting from *P2₁/c* structure and ending at the *C2/m* structure. Enthalpy evolutions for the simulation cells that are taken directly from the simulation (triangle symbols) and after the structural optimization (sphere symbols).

At the 78th metastep, the AlI$_3$ dimers start to polymerize in the unit cell (Fig. 2.9b) which causes a sharp decrease in enthalpy. By the 110th metastep the polymerization process comes to an end. There is another further enthalpy drop, and results in a largely-distorted 6-fold FCC structure (Fig. 2.9c). After another intermediate phase between the 122nd and 149th metastep (Fig. 2.9d), stabilization of the enthalpy was obtained at the 150th step with the *C2/m* structure formed (Fig. 2.9e). The enthalpy evolution in this phase transition shows a stepwise path (Fig. 2.8), where the plateau regions represent a progressive transformation from the dimer-based structure to the polymeric structure with distinct intermediate phases. In Fig. 2.9, the face-centered cubes are highlighted to emphasize that the FCC lattice of iodine are retained, where the 4-fold to 6-fold

conversion of the Al atoms is clear. Moreover, a systematic exploration of the potential energy surface at different P-T conditions using metadynamics revealed that the 6-fold structure with the HCP packing of the iodine atoms [104-105] is also a plausible structure of AlI_3 at high pressure, as seen in the equation of state (Fig. 2.5). This configuration was obtained at several pressures (14 and 26 GPa) starting from the $P2_1/c$ structure. The initial pressure-temperature conditions employed for the simulation or experiment can reach either HCP or FCC iodine atom structures due to the closeness in energy of these two structures in the free-energy surface. However, from experimental results [85], it is clear that the 6-fold fcc structure is the one consistent with the observed high-pressure form of AlI_3.
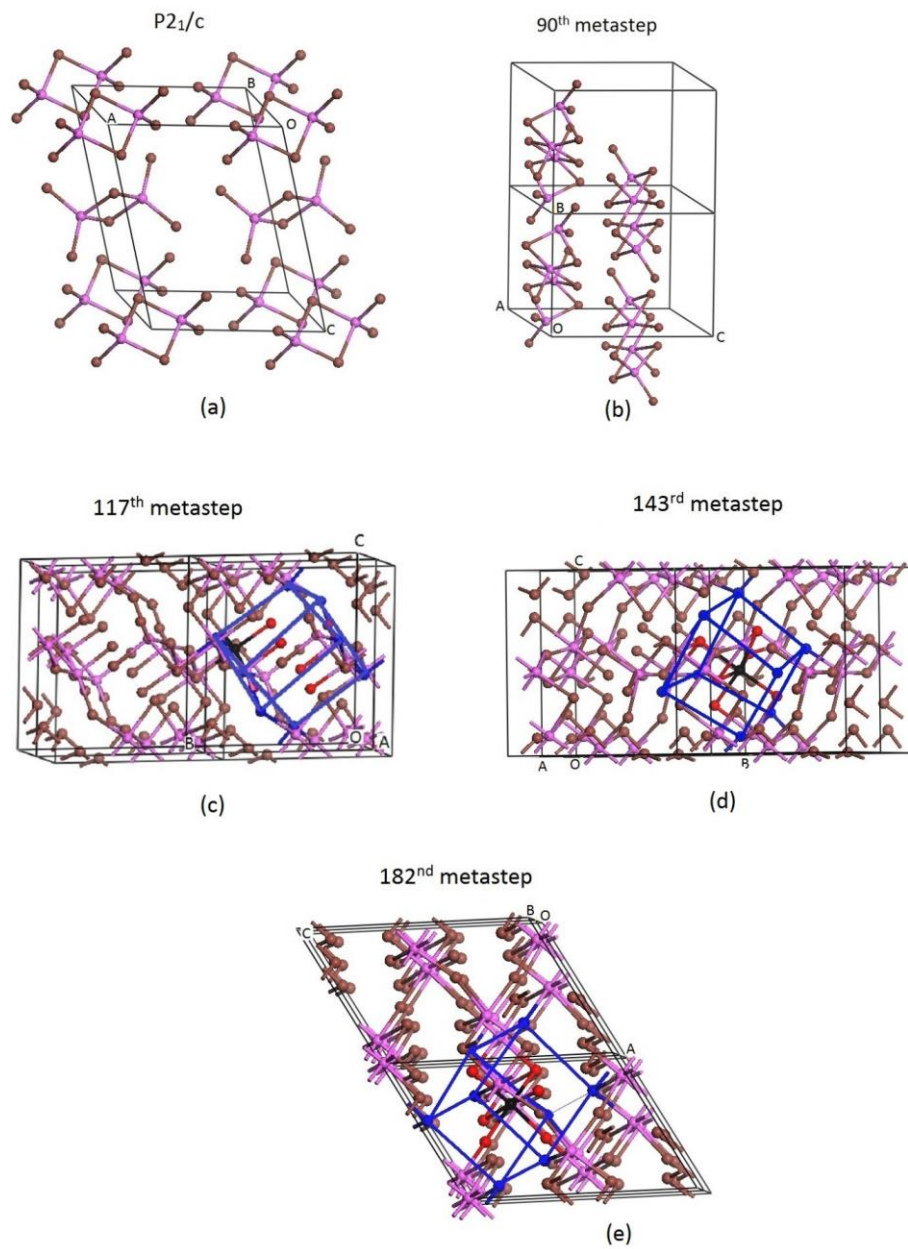
Figure 2.9 Low-energy pathway for the *P2₁/c* to *C2/m* structural transformation revealed in metadynamics simulation at 22 GPa and 300 K. (a) Original *P2₁/c* structure showing dimers. (b) The 90th metastep showing where the dimers cease to exist. (c) and (d) The 117th to 143rd steps showing the formation of the 6-fold coordination of Al in the FCC lattice of the iodine atoms.(e) The 182nd metastep, after relaxation, showing the full transformation to 6-fold co-ordination of the Al atoms.

2.3.2 Electronic Properties

AlI_3 in the ambient condition ($P2_1/c$) is a semiconductor with a band gap of approximately 2.2 eV. On compression, the calculated band gap gradually decreases as shown in Fig. 2.10. The electronic band structure of the $C2/m$ 6-fold co-ordinated structure is shown is Fig 2.11a and 2.11b for 10 and 53 GPa respectively. As evident from both Figs. 2.10 and 2.11, AlI_3 becomes metallic at around 50 GPa.
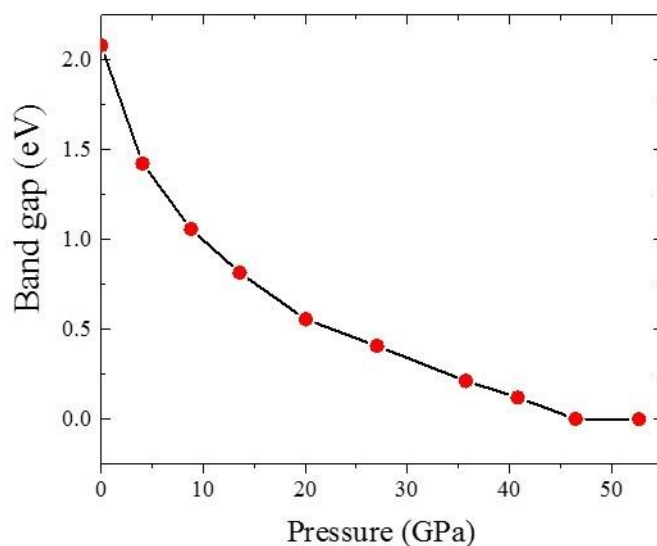
Figure 2.10 Bandgap vs Pressure using PBE XC functional. AlI_3 metalizes at approximately 50 GPa.
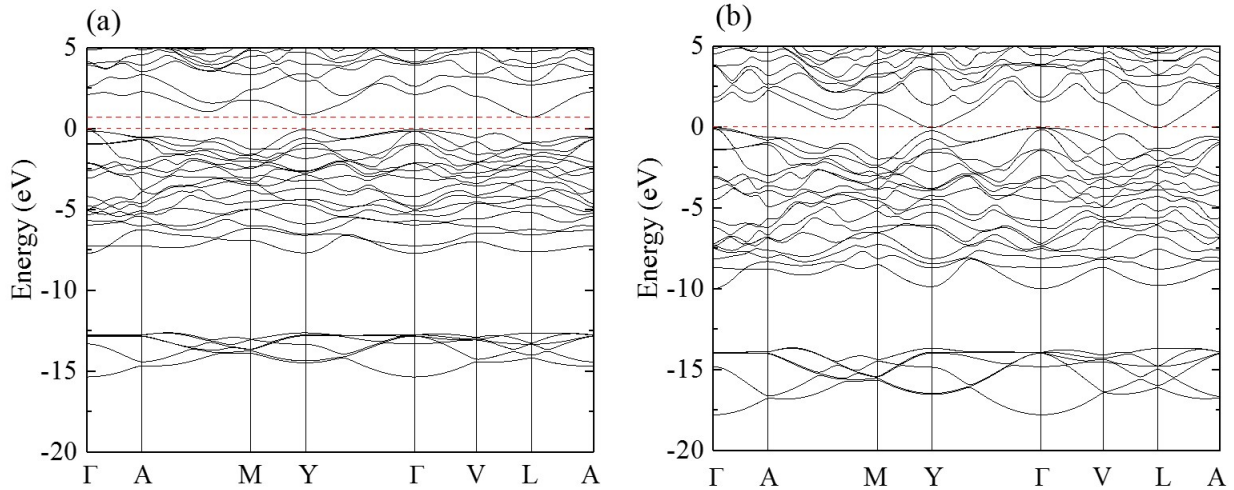
Figure 2.11 Electronic band structure of *C2/m* AlI$_3$ at a) 10 GPa and b) 53 GPa.

2.4 Conclusion

In order to explore for and identify phase transitions, density functional based structural predictions, phonon and Raman spectra calculations were performed along with first-principles metadynamics simulations on crystalline AlI$_3$ at pressures higher than the ambient pressure. As expected, the calculations predicted a clear structural metamorphosis under pressure to a stable face-centered monoclinic structure. Although, previously a single primitive monoclinic structure was taken into account to interpret experimental pressure dependent results, our study suggests that pressure induces a reconstructive phase transition from a *P2$_1$/c* primitive monoclinic structure to the face-centered monoclinic *C2/m* phase. The face-centered cubic lattice of the iodine atoms was maintained however, the aluminium atoms underwent an increase in co-ordination from four in the *P2$_1$/c* ambient pressure structure to six under high pressure. The predicted monoclinic *C2/m* structure at high pressure was determined to be dynamically stable from its calculated phonon dispersion relations and should be identifiable also from its predicted Raman or infrared spectrum. The very close energy of hexagonal close packing and face centred cubic close packing for iodine

atoms can be reached with metadynamics simulations employing different starting pressures but only the diffraction patterns for FCC packing have been observed experimentally, thus allowing us to conclude unambiguously about the crystal structure and space group of the compressed solid aluminium triiodide. This work was published and can be found in reference [113].

CHAPTER 3

PHASE TRANSITION AND SUPERCONDUCTIVITY OF HYDROGEN SULFIDE AT HIGH PRESSURE

A similar version of this chapter has been published as a research article Angewandte Chemie International Edition. The reference is as follows.

- Arnab Majumdar, John S. Tse, and Yansun Yao, "Modulated Structure Calculated for Superconducting Hydrogen Sulfide", Angew. Chem. Int. Ed., 56, 11390 (2017).

Superconductors give rise to electrical currents without loss and are used for applications like magnets in medical imaging. Other applications like large scale usage in electrical power generation and transmission, however, are limited as it is required to cool materials below a critical temperature T_c. Thus, the search for novel superconductors with higher T_c is still a very widely studied discipline. In the words of Vitaly L. Ginzburg in his autobiography *'On Superconductivity and Superfluidity: A Scientific Autobiography'*, high temperature and room temperature superconductivity, and metallic hydrogen were listed amongst the top three problems of the day that needed to be solved. Even after more than a decade, the pursuit is not yet over. The high phonon frequency modes of the light elements are responsible for enhancing electron-phonon coupling and elevating the critical temperature. It has been well established that under the influence of high pressures, many insulators and semiconductors will become metallic. Many experiments and theoretical studies have been performed on compressing hydrogen-rich materials. Since metallization is a precursor to superconductivity, it is convenient to deal with hydrides since it is expected that due to their electron densities, the metallization pressures will be reduced compared to pure hydrogen. In this chapter, one such hydride, compressed hydrogen sulfide (highly controversial topic currently) has been studied extensively for superconductivity at high pressure.

3.1 Introduction

The theory that was suggested by Ashcroft [79] that compressed metallic hydrogen-dominant alloys can be excellent superconductors paved the way for numerous theoretical predictions and extensive experimental investigations. In a dramatic breakthrough made in 2014, an unexpectedly high T_c of 203 K was observed in hydrogen sulfide (H_2S) compressed to 200 GPa [18]. The mechanism for such a high T_c, albeit unclear, is likely to be phonon-mediated from the isotope effect. Initially, this superconducting phase was assumed to be one of the theoretically predicted structures of the high-pressure polymorphs of H_2S [114]. From theoretical calculations carried out later on, it was brought to attention that H_2S is not thermodynamically stable at the experimental conditions and should dissociate into $H_3S + S$ or other hydrogen rich species [115]. For the sulfur hydride systems with H_3S stoichiometry, from the T_c calculations based on the BCS theory [66] hexagonal $R3m$ and cubic Im-$3m$ structures were thought to be possible candidates of the superconducting phase [115]. An unusual observation was the subtle variations in the measured T_c with applied pressure suggesting that more than one structural phase may be responsible for the superconductivity. To justify this observation, the self-alloying "Magneli" phases was proposed to model the continual growth of microscopic regions of H_2S and (superconducting) H_3S in the bulk crystal with varying pressure [116]. Experimentally, it was found that the pressure-induced structural changes depended strongly on the sample preparation procedure and compression sequences. Distinctively different XRD patterns were reported at similar pressure and temperature (following different thermodynamic paths) [117-120]. The measured diffraction patterns were assigned to mixtures of many theoretically predicted dissociated H_xS phases of various compositions. An exception is the simultaneous conductivity and diffraction measurements performed by Einaga *et al.* [119]. Following a *P-T* path similar to the previous superconductivity

studies, Einaga *et al.* took an H_2S sample in the diamond anvil cell that was first brought to 100 K at ambient pressure and compressed to 150 GPa; then further cooled to ~ 10 K and eventually the temperature was raised [119]. In this manner, they observed a similar trend of the T_c and obtained much simpler diffraction patterns which were assigned to the *Im-3m* H_3S structure and high pressure *β*-Po elemental sulphur. A drawback of this assignment is that the observed intensity ratio of the H_3S and S phases in the diffraction pattern does not support the 2:1 ratio for the dissociation products of $3H_2S \rightarrow 2H_3S + S$ [121]. From the inspection of the experimental pattern, the amount of S in the sample is substantially smaller. Goncharov *et al.* reported a very similar diffraction pattern of a reaction product synthesized directly from elemental sulfur and molecular hydrogen at 140 GPa but followed a different *P-T* path [120]. An observation is that the diffraction patterns of both the proposed *Im-3m* H_3S phases always show two weak peaks situated on either side of the strong lowest angle Bragg reflection with similar *d*-spacings and relative intensities. Guigue *et al.* performed a direct synthesis from the elements but were able to identify only an orthorhombic *Cccm* structure up to 160 GPa and challenged the hypothesis based on the *R3m* and *Im-3m* structures [122]. In view of the synthetic pathways and very different starting S:H stoichiometry, these weak reflections are unlikely to be just sulphur impurities. This raises the possibility that the observed products may be metastable and not the thermodynamic H_3S ground states as predicted by *ab initio* structural search. In this study, we took a different approach to explore possible structure(s) for the superconducting phase. Noting that the occurrence of metastable structures are not uncommon in experiments, in particular, at low temperature when there is not sufficient energy to overcome the activation barrier of bond breaking [121], we performed metadynamics simulations to explore energetically accessible metastable structures.

In this work, *ab initio* metadynamics calculations are performed at a broader P–T regime to trace the transformation pathway from the low-pressure molecular phase to the high pressure modulated structure have been reported. In particular, a stoichiometric Pc structure was identified. This structure was further studied for dynamical stability and superconducting critical temperatures, T_c following the observed trend of the long-sought 'low-T_c phase'. It has been shown from theoretical calculations that the Pc structure becomes dynamically unstable above 150 GPa, with softening of the transverse acoustic phonon modes near the boundary of the Brillouin zone. The phonon softening bolsters a reconstruction of the supercell along the y-axis leading to a 1:3 modulation of the original unit cell. The T_c of the modulated structure at high pressure is shown to be comparable to the measured T_c for the 'high-T_c phase' found experimentally. Therefore, in this chapter, the Pc structure is justified to be the underlying structure along the experimental compression path which is metastable and shows excellent T_c trends.

3.2 Computational Details

The new structures of H_2S at high-pressures were obtained using the metadynamics method [64] combined with the projector augmented plane-wave (PAW) method [98] as implemented in the Vienna *ab initio* Simulation Package (VASP) [55]. We employed the Generalized Gradient Approximation (GGA) for the exchange-correlation functional parameterized by Perdew–Burke–Ernzerhof (PBE) [46]. A kinetic energy cut-off of 280 eV was used for grid integration and for sampling the Brillouin zone (BZ) for which a ($16 \times 16 \times 16$) Monkhorst Pack (MP) grid [99] was considered. The metadynamics simulations were carried out in the pressure range of $80 - 200$ GPa, and in the temperature range of $80 - 200$K, starting from simulation supercells with various sizes. The scaled components of the edge vectors of the simulation supercells were used as collective variables [123-124]. First principles molecular dynamics (FPMD) simulations were performed

using the VASP program, employing an isothermal-isobaric (NPT) ensemble with Langevin dynamics as well as using an isothermal-isochoric (NVT) ensemble. Topological analysis of the charge density was carried out using quantum theory of atoms-in-molecules method introduced by Bader [125-126]. Phonon calculations were performed using the Quantum ESPRESSO package [82] with norm-conserving pseudopotentials and an energy cut-off of 80 Ry. Individual phonon matrices were calculated on a $4 \times 2 \times 2$ q-point mesh with an $8 \times 8 \times 8$ k-point mesh for BZ sample. The electron-phonon coupling (EPC) parameter and logarithmic average of the phonon frequencies obtained between 100 to 130 GPa have been calculated within the framework of the Bardeen-Cooper-Schrieffer (BCS) theory [66].

3.3 Results and Discussion

3.3.1 Structural Analysis

Metadynamics simulations were carried out at three temperatures (80 K, 200 K and 300 K) at 80, 100, 150, 190, and 200 GPa. The theoretically predicted *Pmc2$_1$* structure of H_2S was used as the initial structure, *i.e.*, structure precursor, in the simulation. Previously, the *Pmc2$_1$* structure (Fig. 3.1a) was calculated to be the lowest enthalpy phase for H_2S between 65 and 80 GPa [114].
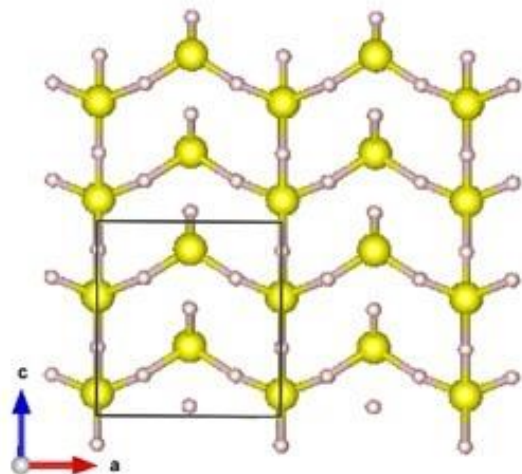
Figure 3.1 The *Pmc2₁* structure optimized at 80 GPa. Big (yellow) and small (white) spheres represent S and H atoms, respectively.

In the metadynamics simulations, several new structures of H_2S were identified at different *P-T* regions. The first thing that one notices from the simulations is that the structural morphologies of the metastable phases identified along the 80 K, 200 K and 300 K isotherms at 80 GPa, 150 GPa and 190 GPa are very different (Fig. 3.2) although they start from the same precursor structure. This is a clear result of the changes in the potential energy surfaces of compressed H_2S at different *P–T* points. At 80 GPa and 80 K, the polymeric *Pmc2₁* structure transforms to a monoclinic structure, with a *Pc* space group, composed of zigzag S-H-S chains and H_3S molecules. In this structure, valence electrons are partially transformed from the H_3S molecules to the S-H-S chains forming nominally SH^- and H_3S^+ ions. The electrostatic attractions between the SH^- and H_3S^+ lead to the stabilization of this structure. In comparison, on increasing the temperature to 200 K, the extended chain structure is not formed. The morphology that H_2S now takes up is a molecular crystal consisting of H_2S-HSH molecules. The H_2S-HSH is a polar molecule in which one H_2S is cationic and the other moiety is anionic. At 300 K, longer, zigzag molecules are seen in the solid (outlined by the red dash box).
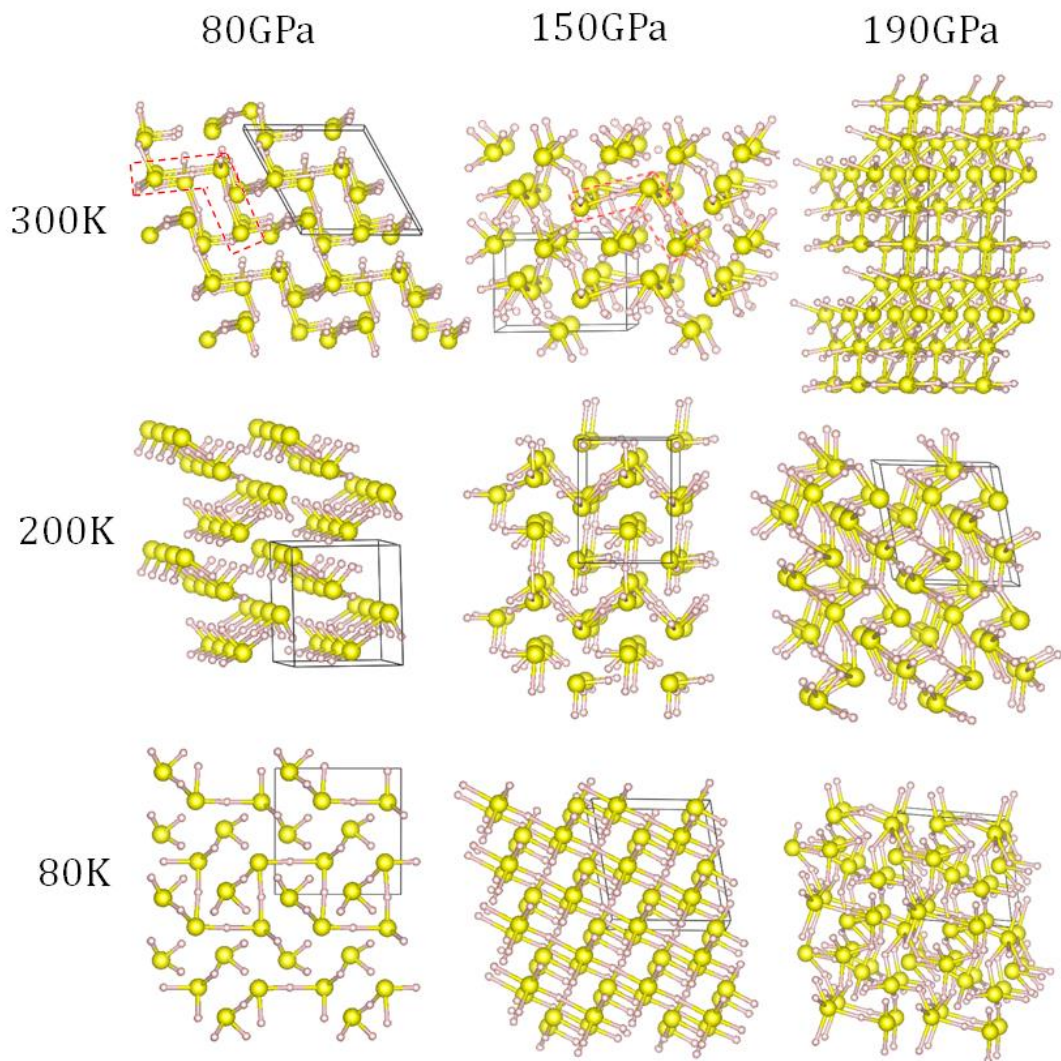
Figure 3.2 Different crystal structures of H_2S obtained from the different metadynamics simulations carried out various different pressures and temperatures, starting from the *Pmc2₁* crystal structure. Big (yellow) and small (white) spheres represent S and H atoms, respectively.

Clearly, reducing the temperature enhances the intermolecular interactions in the solid which drives the crystal structure to a higher dimensionality, from a 0D molecule to a linear chain structure. Similar changes of the dimensionality can also be expected when the pressure is increased. At 150 GPa and 80 K, no molecular species can sustain in the structure in which only linear S-H chains are observed. At 200 K, the H_2S-HSH molecules formed at the same temperature

but low pressure (80 GPa) are now linked to form a 3D extended framework. At 300 K, traces of the dimerized H_2S-HSH units can still be discerned but the molecular units are more densely packed. At 190 GPa and 80 K, a 3D framework with S-H-S linkages is formed. The structure is stabilized by the electron-deficient multicenter S-H-S interactions when neighboring sulfur atoms are linked by a common hydrogen atom. In the linkage, electrons are delocalized leading to a metallic state. A similar morphology is observed at 200 K. However, at 300K, a 3D framework built solely of S atoms is formed. In this structure, the S atoms are directly bonded to each other rather than bypassing a hydrogen atom.

One interesting structure that was obtained at 100 GPa and 80 K was a new low-enthalpy structure with the *C2* space group (Fig. 3.3).
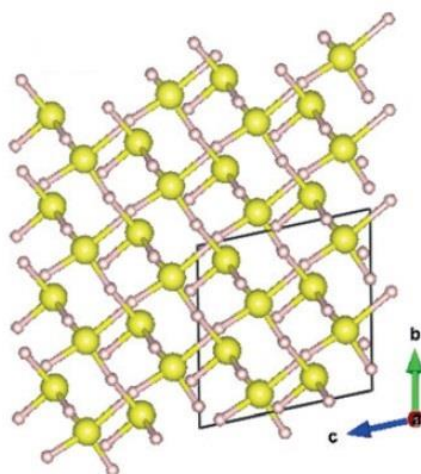
Figure 3.3 *C2* structure obtained from metadynamics at 100 GPa and 80 K.

The *C2* structure enters the phase diagram initially as metastable but it becomes progressively more stable as the pressure increases. The enthalpy of the *C2* structure becomes lower than the *Pmc2$_1$* structure near 90 GPa, and by 160 GPa, it is degenerate with the enthalpies of the *P-1* and *Cmca* structures. The latter two structures were previously established lowest-enthalpy structures of H_2S in this pressure region. Thus, we consider the *C2* structure as another

66

candidate for the ground-state structure of H_2S at high pressure, which is linked to the precursor *Pmc2$_1$* structure through a low-energy transition path. Interestingly, in the *C2* structure the S atoms form diatomic pairs similar to that in disulfide groups. The neighboring S-S pairs are bridged by H atoms which extend in one-dimension to form infinite $[-S-H-S-]_\infty$ chains, with the rest of the H atoms intercalated in between. Extended chain structures immediately indicate an electron delocalization, which, not surprisingly, yields a metallic ground state for the *C*2 structure. Even though the *C*2 structure was identified, and the structure itself is an interesting topic, it may not be the primary contributor to the high T_c. Previous experimental and theoretical studies suggest that H_2S decomposes in the Mbar region to several S-H compounds, which are responsible for the sudden rise of superconductivity [117-119]. The considered decomposition products include H_3S, H_5S_2, H_4S_3, HS_2, and heterogeneous H-S mixtures. Among which, a cubic structure of H_3S (*Im-3m*), made of two interpenetrating SH_3 perovskite sub-lattices, has been featured prominently. The explanation for the experimental XRD and T_c based on the *Im-3m* structure is generally acceptable [127]. On the other hand, ambiguity still remains in this interpretation; in particular with respect to the difficulty of locating the hydrogen atoms by x-ray diffraction could not be resolved. The hydrogen positions in the *Im-3m* structure were not conclusive. A strong evidence for discrepancy appeared in the experiment by Einaga *et al.* [119], where the measured volumes of H_2S and D_2S are constantly larger (~ 3%) than the theoretical estimate using the *Im-3m* structure, indicating the composition of hydrogen in the compound may be different. Moreover, the decomposition of $3H_2S \rightarrow 2H_3S + S$ implies that the XRD intensity ratio of H_3S and S should be close to 2:1, but this was not always the case in previous experiments [121]. Thus, there could be other interpretations of the decomposition processes and the experimental XRD patterns.

The instability of H_2S was confirmed by the metadynamics simulation, which indeed showed a tendency of dissociation of H_2S in the Mbar region. Remarkably, it was revealed that

67

H_2S could in fact be self-ionized into a $(SH)^{\delta-}(H_3S)^{\delta+}$ structure without losing the basic body-centered cubic (BCC) motif. This structure was identified at 80 GPa and 80 K, and characterised as a monoclinic structure with the *Pc* space group (Fig. 3.2). In Fig. 3.4, the drops in the enthalpy with respect to metasteps during the metadynamics simulation gives way to the structural phase transformation from *Pmc2₁* to *Pc*, indicating the transformation to a more energetically stable structure.
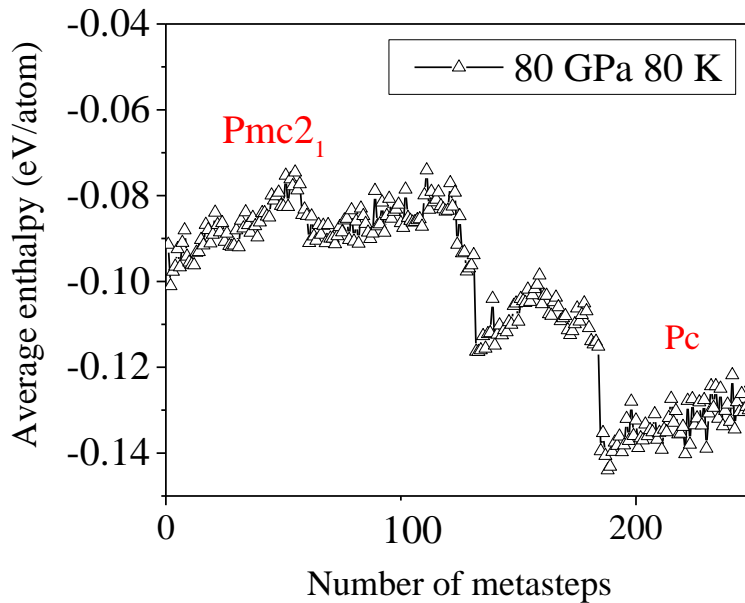
Figure 3.4 Metadynamics simulation at 80 GPa and 80 K showing the evolution of the enthalpy starting from *Pmc2₁* structure and ending at the *Pc* structure.

In the *Pc* structure the S atoms form a distorted BCC lattice. Three H atoms are bonded to each body-center S and form a positively charged H_3S molecule. The other H atoms are located between corner S atoms, forming extended, negatively charged $(SH)_\infty$ chains. Bader Charge Analysis revealed that the amount of charge transfer to the S-H chain is about $\delta=0.41e^-/SH$ (calculated at 80 GPa), which is also responsible for the electrical conductivity. A particularly interesting feature of this structure is the asymmetric S-H-S bond lengths, which could be

associated with the quantum effects of hydrogen, analogous to the O-H-O bond in ice X [128]. The calculated distinct S-H lengths are 1.46 and 1.60 Å, respectively, at 80 GPa. The self-ionized Pc structure still maintains the H_2S composition. Its volume is also larger than pure H_3S at the same pressure which could yield a better volume comparison to the experiment. We note that the dissociation process of H_2S discovered here is apparently analogous to that of H_2O, *i.e.*, $2H_2O \rightarrow H_3O^+ + OH^-$. The dissociation of H_2O is a rare event at ambient conditions but not uncommon at high pressures. The H_2S itself, was also suggested to dissociate dynamically, in a short time period, to SH^- and H_3S^+ species into the high-pressure phase V (around 35 GPa) [129]. The Pc structure on the other hand is dynamically and mechanically stable as shown by the absence of imaginary frequencies in the calculated phonon dispersions (Fig. 3.5b). The enthalpy of this structure, however, is higher than stoichiometric H_2S structures with regular H-S bonding (Fig. 3.5a), indicating that it is metastable.
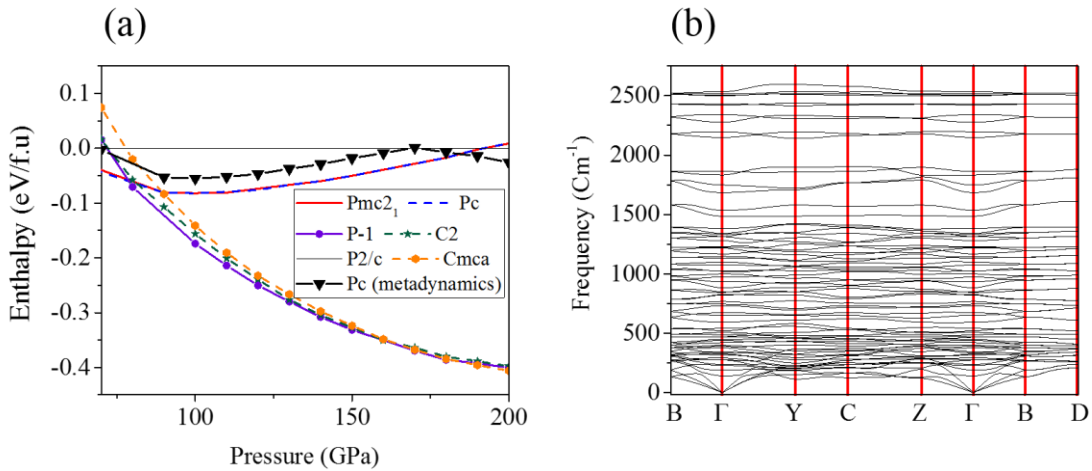
Figure 3.5 a) Enthalpy vs pressure for different H_2S structures, with the $P2/c$ structure as the zero-enthalpy reference. b) Phonon dispersion relation for the Pc structure calculated at 120 GPa.

On the face of it, a higher enthalpy may strike as a manifestation of dissociation, which is nevertheless not unexpected, but the dynamic behavior of the structure, in particular the motions of the hydrogen atoms, are rather critical to the superconductivity. It has been shown in sample

hydrides that strong electron-phonon coupling is often associated with the lattice instability, where enhanced atomic vibrations couple strongly with the perturbed electrons [130-131].

To examine the dynamic behavior of the $(SH)^{\delta-}(H_3S)^{\delta+}$ structure under pressure, FPMD simulations were carried out on a model structure at 200 GPa and 200 K, in both NPT and NVT ensembles. The model structure was constructed in an ideal 4×4×4 bcc supercell of sulfur, with all lattice distortions removed to mimic the experimental conditions. The hydrogen positions in the BCC lattice were adopted from those in the *Pc* structure (the fractional coordination). The dynamics of the model structure has been examined from visualization of the atomic trajectories. Fig. 3.6a shows the equilibrated trajectories over 20 ps collected in the NVT simulation. In this ensemble, the volume and shape of the supercell were fixed, and the S atoms are found to vibrate about the ideal BCC lattice points. The H atoms, on the other hand, show a high degree of mobility and undergo rapid diffusions in the cell. It appears that the H atoms from the SH^- and H_3S^+ species are no longer distinguishable under dynamic conditions. All H atoms form a coherent group and move about the lattice in a mobile but ordered manner. The structure factor derived from the NVT trajectories shows a close resemblance to a BCC lattice with slight thermal distortions. The model structure remains stable and does not transform to any other structures during the simulation time, which is normally expected for an NVT simulation. The NPT simulation, in which all degrees of freedom of the model structure are allowed to change, reveals a subtle deformation of the bcc lattice. The plot of the temporal atomic positions shown in Fig. 3.6b shows that under dynamical conditions, a quarter of the unit cells in the supercell undergo tetragonal distortions (shown in green), while the others maintain the cubic form (shown in blue). In the equilibrated structure, tetragonal unit cells are aligned in slabs and alternate with cubic regions in a 1:3 ratio, forming a modulated structure with a quadrupled period.
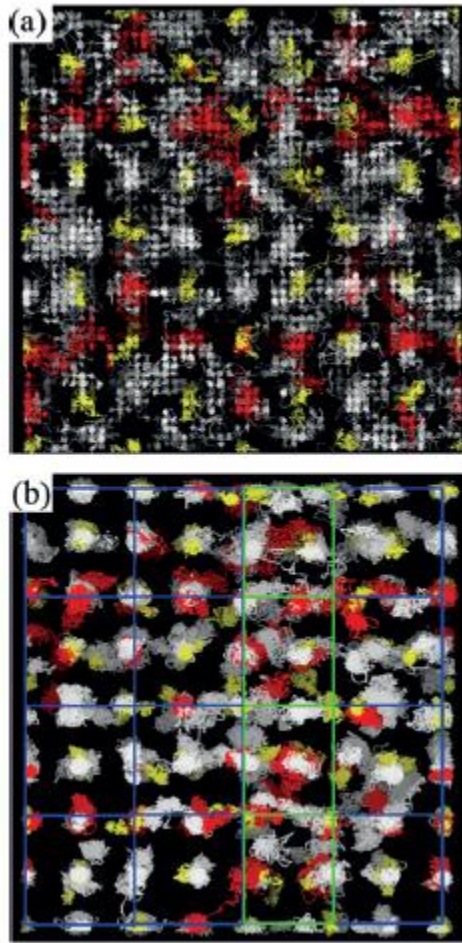
Figure 3.6 Thermal trajectories of the model structure at 200 GPa and 200 K over 20 ps, in a) NVT and b) NPT ensemble. The S atoms are colored yellow. The H atoms initially belonging to the [-S-H-S-] chain are colored red and H_3S molecules are colored white.

Compared with fixed-cell structure, the atomic mobility in the modulated structure is generally reduced which could be understood from the energy equipartition among a greater degree of freedom in the NPT ensemble. However, in the tetragonal region, the mobility of hydrogen is actually enhanced, which is visibly larger than that in the cubic region. These 'hot regions' are most probably responsible for the transport properties of the modulated structure. Significantly, the modulated structure discovered here bears similarities to the previously proposed Magnéli phases

of hydrogen sulphide systems [116]. In the Magnéli phases, slab-like H_2S and H_3S regions stack alternatively and form long-periodic modulated crystals. The difference, however, is that the modulated model discovered here still maintains the H_2S stoichiometry while the successive Magnéli phases must imply gradual loss of S which again would result in a volume mismatch to the experiment. This point is already exemplified in Ref. [116], where the theoretical results of Magnéli phases at a lower pressure (150 GPa) had to be used to compare with the experimental data at high pressure (173 GPa). Moreover, the Magnéli phases as variable composition mixtures do not match the observed XRD pattern, and therefore at this point they only serve as hypothetical models.

A key justification for predicted structures is that they should match the experimental XRD pattern of the high-T_c phase. The matching has been carried out numerous times by different groups using theoretical structures with various stoichiometry. A generally accepted interpretation, for example, as shown recently by Einaga *et al.* [119], is that the experimental XRD pattern of the high-T_c phase corresponds to a mixture of H_3S (BCC structure) and S (β-Po structure), in which the H_3S component is responsible for the high T_c. Here, we demonstrate that the XRD pattern can be sufficiently interpreted by the modulated structure of H_2S, without introducing the assumption of the decomposition $2H_2S \rightarrow H_3S + S$. Since the tetragonal-cubic modulation only represent a motif, several trial structures were generated using different tetragonal to cubic ratios in the supercell, from 1:9 to 9:1. In Fig. 3.7, the constructions are exemplified by three structures with the ratios of 1:3, 1:5, and 1:9, where the tetragonal and cubic regions are colored in red and yellow, respectively. For convenience, the H atoms are removed from the cells since their contribution to the XRD pattern is negligible.
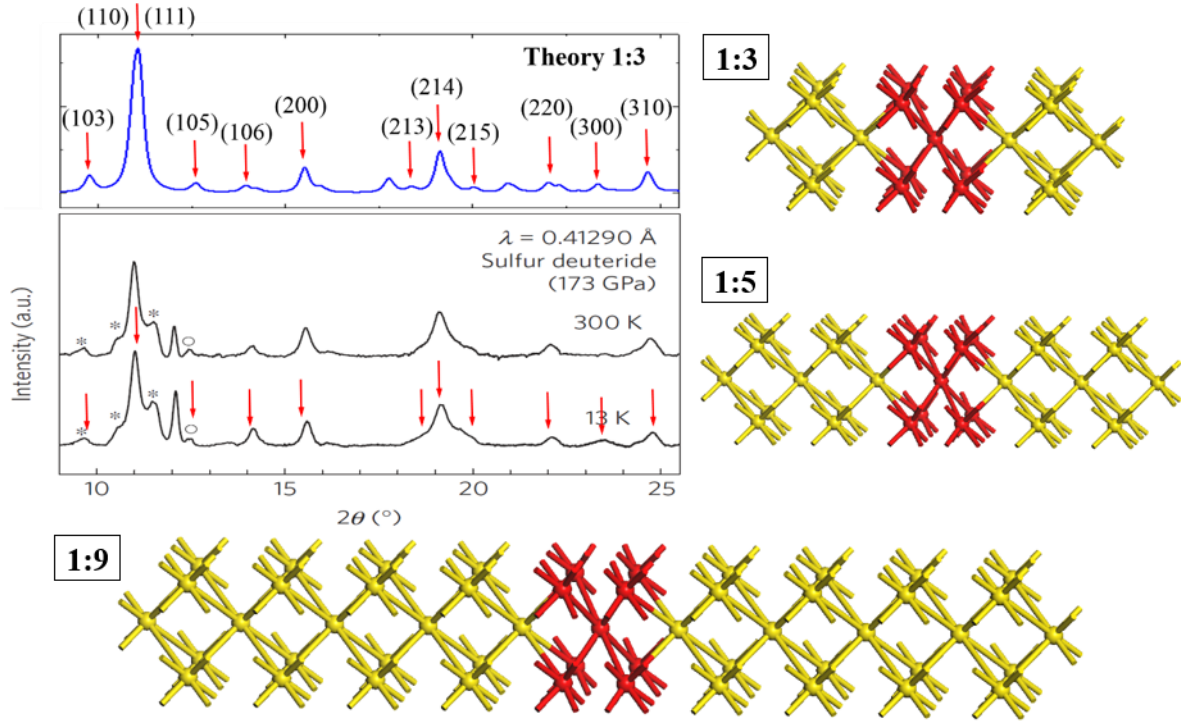
Figure 3.7 The simulated XRD pattern using a 1:3 modulated structure and experimental patterns. Modulated structures with 1:3, 1:5, and 1:9 ratios are shown. The tetragonal and cubic regions are in red and yellow respectively. The experimental XRD is adopted from Ref. [119].

From the trials, we found that the 1:3 realization fits remarkably well with the experimental XRD pattern (obtained at 173 GPa and 13 K) (Fig. 3.7). Significantly, the ratio here is same as that found in the FPMD calculations and unlikely to be just a mere coincidence. The 1:3 structure has the $P4/mmm$ space group. The structural parameters used for matching the experimental XRD are, $a = 3.06$ Å, $c = 11.91$ Å, with S atoms located at $1c$: 0.5, 0.5, 0.0; $1d$: 0.5, 0.5, 0.5; $2h$: 0.5, 0.5, 0.7727; $2g$: 0.0, 0.0, 0.6363, and $2g$: 0.0, 0.0, 0.0909. Specifically, the weak peak around 9.8° is from the (103) reflection, which overlaps with a peak from the gasket. The broad band centered on 11.1° contains two peaks, (110) and (111). The weak peak near 12.6° is from (105) and overlaps with a peak from phase IV of S. The peak around 14.2° is (106), which was previously interpreted as a peak from the β-Po structure of S. The broad band centered on 19.1° contains three peaks,

(213), (214), and (215). This band was previously interpreted as combined H_3S and β-Po peaks. The three peaks above 22° are (220), (300), and (310), respectively. In view of the comparison between the simulated and experimental XRD, the peaks have outstanding agreements not only in the 2θ positions but also in relative intensities.

3.3.2 Superconducting Properties

To understand how the Pc structure evolves to the modulated $(SH)^{\delta-}$ $(H_3S)^{\delta+}$ structure at high pressure, the mechanical and electronic properties of this structure were investigated at selected pressures between 80 to 180 GPa. At 80 GPa, the Pc structure turned out to be a semiconductor with a band gap of about 0.3 eV (Fig. 3.8a). The calculated electronic density of states (DOS) shows the S-H-S chains are the main contributors compared to the H_3S cations near the Fermi level (Fig. 3.8b). The small band gap is due to the asymmetrical S-H-S bonds along the chain. In the conduction band (consisting of S-H antibonding states), both the chain and the cation S atoms contribute almost equally. At 100 GPa, the band gap closes with the lowest-energy conduction band crossing the Fermi level forming an electron-pocket near the Γ point. Therefore, the Pc structure becomes metallic at the onset of 100 GPa.
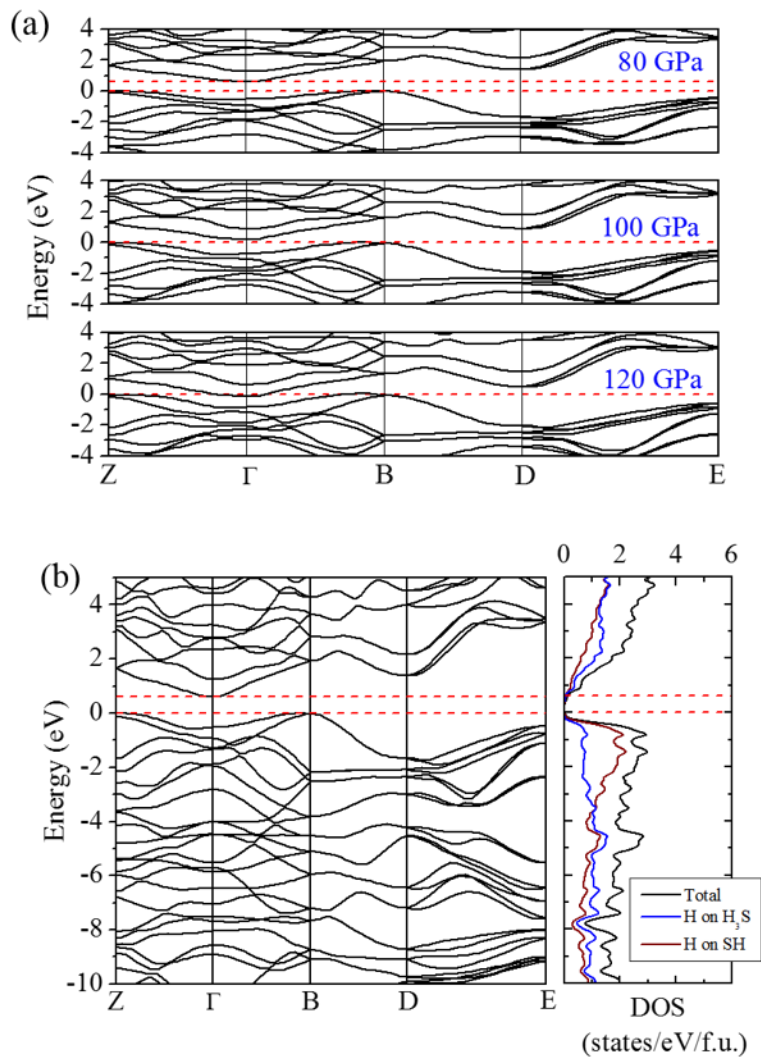
Figure 3.8 (a) Evolution of the electronic band structure of the *Pc* structure near the Fermi level at 80, 100 and 120 GPa using PBE XC functional. (b) Electronic band structure and projected DOS of the *Pc* structure at 80 GPa. The black curve represents the total DOS of the H_2S system. The red curve indicates the DOS of the H atoms belonging to the S-H-S chain while the blue curve indicates the DOS of the H atoms of the H_3S cations.

The delocalization of the electrons in the *Pc* structure upon increasing pressure made the structure unstable starting at 150 GPa as revealed by the softening of acoustic phonon branches. At 180 GPa, the acoustic vibrational bands become imaginary at about one-quarter of the phonon

vectors from the $\Gamma \rightarrow Y$ and $C \rightarrow Y$ symmetry directions (Fig. 3.9a). The appearance of the imaginary modes at the particular points mentioned above hints that the *Pc* structure may reconstruct to a supercell close to the 1:3 ratio along the Y-direction as found in the *NPT* MD calculations. Thus, the formation of the 1:3 modulated structure in this pressure range cannot be a mere coincidence. It is a result of the intrinsic instability of the H_2S structure. From the projected vibrational DOS (Fig. 3.9b), it can be seen that the imaginary phonon modes mainly arise due to the large amplitude motions of the H and S atoms in the S-H-S chains.
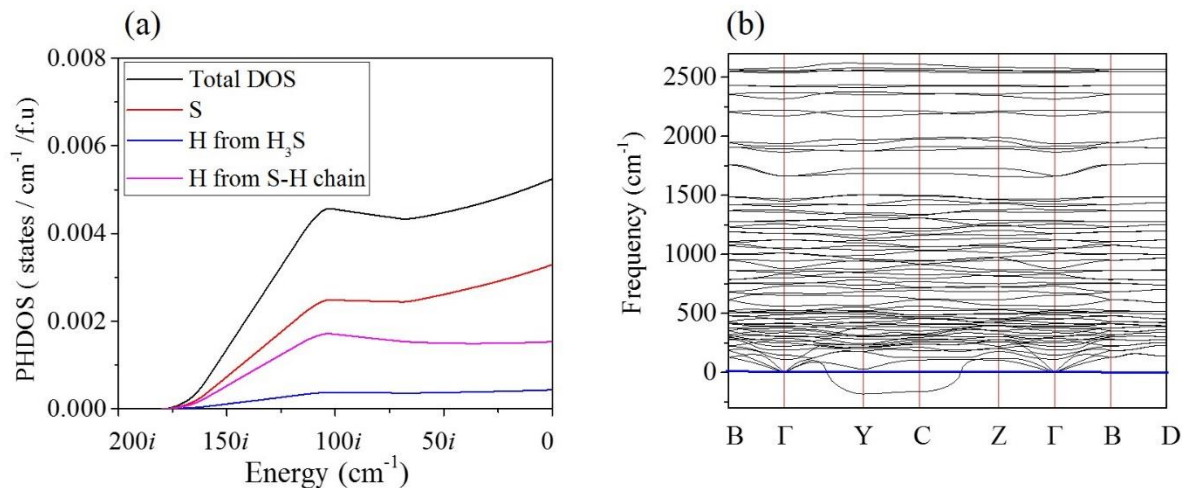
Figure 3.9 (a) Total and atom projected vibrational density of states of the *Pc* structure at 160 GPa. (b) Phonon dispersion of the *Pc* structure curve at 180 GPa.

The instability revealed in the electronic structure of H_2S is corroborated by the results of FPMD simulations performed on a model with the S and H atoms in the *Pc* structure in a *NVT* ensemble. At 120 GPa, all of the H atoms in the *Pc* structure vibrate about the respective atomic sites and the basic zigzag chain and H_3S molecules is maintained. However, when the pressure is increased to 160 GPa, the motions of the H atoms become highly mobile making it difficult to identify the chain and the molecule. From Fig. 3.10, it is quite obvious that there are collaborative

hopping motions between different H sites. The high-mobility motions of the H atoms substantially softened the vibrational modes and change the long-range order in the structure.
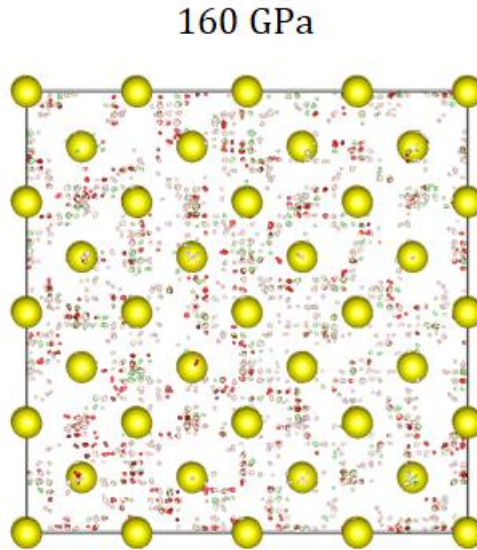
Figure 3.10 Temporal positions of the S and H atoms indicated by different colours at different slices from molecular dynamics simulation (see text) showing the rapid hopping motion of the hydrogen atoms at 160 GPa.

It is should be noted that in the *NVT* calculation the simulation cell is kept fixed so the S atoms are more or less staying at the lattice sites. If the unit cell vectors are allowed to evolve, a modulation of the supercell will occur following the soft phonon modes. Experimentally, superconductivity was observed in compressed H_2S at pressures as low as 110 GPa. Referred to as the 'low-T_c phase', this superconducting phase is achieved by cold compressing (at around 100 K) the H_2S sample to high pressures [18, 119]. The T_c of the 'low-T_c phase' ranges between 33 and 150 K when the pressure is increased from 110 to 200 GPa. Experimentally, little is known about the chemical composition and structure of this phase. The theoretical results presented above show unambiguously that there is a direct connection between the low-pressure polymeric structure (*Pmc2₁*) and high-pressure modulated structure *via* the intermediate *Pc* structure. If there is a clear

connection between the *Pmc2₁*, *Pc* and the modulated structure, the question that one asks is whether the *Pc* structure in this pressure region is superconductive and, if so, would the T_c also agree with the experimental observations for the 'low-T_c phase'? For this purpose, the superconducting properties of the *Pc* structure in the stable pressure range were investigated using the phonon-mediated strong coupling Migdal-Eliashberg methodology [69-71] based on the BCS theory [66].

The electronic band structures of the *Pc* structure (Fig. 3.8a) reveals the simultaneous occurrence of curve (dispersive) and flat (diffusive) bands near the B symmetry point and close to the Fermi level. This is a favorable condition for strong-electron coupling [132-133]. The electron-phonon Eliashberg spectral function $\alpha^2F(\omega)$ and integrated EPC parameter λ calculated at 120 GPa have been shown in Fig. 3.11a. From the figure, the strength of the EPC in the *Pc* structure is weighted more heavily in the low-frequency region where the primary contribution is by the S-H-S vibrations within the zigzag chains. At 120 GPa, the value of λ estimated by integrating $\alpha^2F(\omega)$ is about 1.6. To this integrated value of 1.6 of the λ, more than 80% is contributed by the low-frequency vibrations below 1000 cm⁻¹. The high-frequency S-H vibrations of the H_3S molecules (above 2000 cm⁻¹), on the other hand, have very insignificant contribution to the EPC. Up to 1500 cm⁻¹ there is strong coupling of H and S vibrational modes. The bands from approximately 500 to 1500 cm⁻¹ can be attributed to S-H-S bending modes. From the EPC distribution, it is reasonable to suggest that the superconductivity of the *Pc* structure mainly arises in the S-H-S chains, rather than in the H_3S molecules. This also agrees with the band structure of the *Pc* structure in which the electronic states around the Fermi level are primarily occupied by the S-H-S chains (Fig. 3.8b).

The T_c, ω_{log} and λ for the Pc structure at 100, 110, 120, and 130 GPa were estimated using a nominal value of 0.1 for the Coulomb pseudopotential μ^* (Table 3.1) making use of the Allen-Dynes modification of the McMillan equation [76]. The calculated T_c of the Pc structure is remarkably in very good agreement with the experimentally observed T_c in the 'low-T_c phase', from the compression of H_2S at low temperatures [18]. The T_c remains almost constant on increasing the pressure from 100 to 130 GPa as the λ increases but the ω_{log} decreases. Significantly, the characteristic ω_{log} is found to decrease with pressure in this pressure range.

P (GPa)	λ	ω_{log}(K)	T_c (K)
100	1.49	380	42
110	1.56	356	42
120	1.64	344	42
130	1.75	332	43

Table 3.1 The calculated λ, ω_{log}(K) and T_c(K) for the Pc structure.

At higher pressures, the S-H stretch and H-S-H bent vibrations mix more efficiently in the mid-frequency region which enhances the EPC strength λ. Moreover, the electronic density of states at the Fermi level also increases slightly with the pressure as the metallicity increases in the structure. However, overall, the T_c of the Pc structure remains almost constant at 42 K due to the decreasing ω_{log} factor. The estimated T_c of the high pressure Pc structures are comparable to the reported theoretical values for H_xS species like H_5S_2 and Magnéli phases [116, 133] and the $Cmca$ H_2S phase [134].
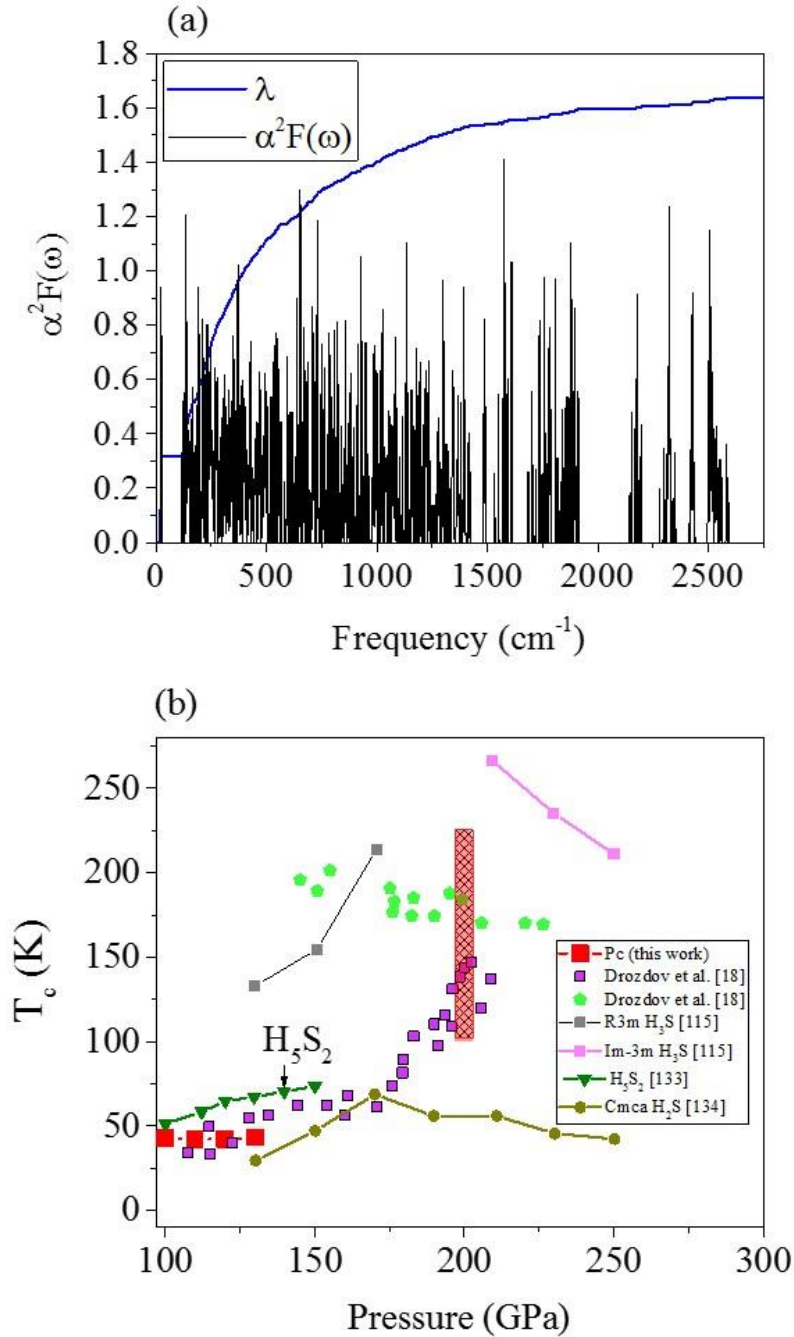
Figure 3.11 (a) The Eliashberg phonon spectral function $\alpha^2F(\omega)$ and the electron-phonon integral $\lambda(\omega)$ of the *Pc* structure calculated at 120 GPa. (b) T_c phase diagram of various H_xS species. The red squares represent the value of T_c for the *Pc* structure reported in this work in the pressure range of 100 to 130 GPa. The shaded red region indicates the range of values of T_c at 200 GPa for the modulated 1:3 structure, calculated for the range of EPC parameter (λ) from 1.0 to 2.0. The open symbols denote experimental results.

We now shift the discussion to the 1:3 modulated structure. In this structure, the body-centered tetragonal and body-centered cubic unit cells are aligned along the Y-direction and alternate in a 1:3 ratio, forming a modulated structure with quadrupled period. In the 1:3 modulated structure, the H atoms undergo rapid diffusion, and the mobility is much higher in the tetragonal region than in the cubic region. The high mobility of the fluxional motion of the H atoms assists the phonons to pair electrons as per the BCS theory [66], whereas the large amplitude of these motions leads to the crossing of the Fermi level by the conduction bands. It is computationally not feasible to compute the strength of the electron-phonon coupling on such a large and dynamic structure. However, according to conventional BCS theory of superconductivity, only electronic levels (occupied and unoccupied) situated within a few meV at the vicinity of the Fermi surface are responsible for electron-phonon process. Molecular dynamics calculations presented above show the H atoms of the H_3S moieties (not participated in the S-H-S linkages) are very mobile. Therefore, fluxional motions of these H may strongly alter the temporal electronic band structure near the Fermi level. To test this hypothesis, we computed the electronic structure of a model where all the atoms of the proposed 1:3 structure were fixed except one H atom closet to the S atom of the nearby SH rectangular meandering chain was allowed to move from its equilibrium position. The band structures within ±500 meV of the Fermi level at displacements of 0.0, 0.1 and 0.25 Å have been compared in Fig. 3.12a. The results clearly show that an electron pocket is formed along the $\Gamma \rightarrow Z$ direction when the H atom was displaced. The large amplitude motion of the H led to temporal fluctuations of the unoccupied electron band at the Fermi level. The simultaneous occurrence of steep and flat bands near the Γ point sets up a favorable condition for electron pairing through dynamic vibration of the Fermi level [132-133]. This is an indication of strong electron-phonon coupling. Without the fixed atomic positions, we can only make an order-of-magnitude

estimation of the T_c for the modulated structure. *NPT* FPMD simulation was carried out on the modulated structure at 200 GPa and 200 K for 20 ps, and then the vibrational density of states (*v*DOS) was calculated using the single-particle velocity autocorrelation function obtained from the atom trajectories, which captures both harmonic and anharmonic vibrations.
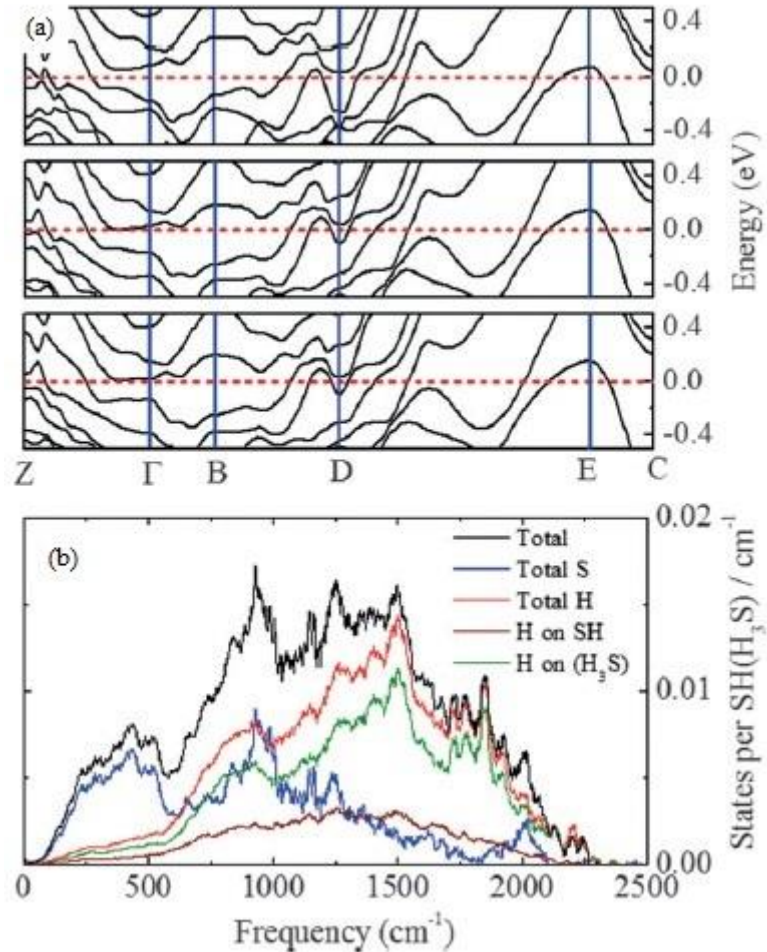
Figure 3.12 a) Band structures of the model structure with a single H atom in the SH chain displaced by 0 b (top), 0.10 b (middle), and 0.25 b (bottom). b) Total and projected vibrational density of states obtained from the trajectories shown in Fig. 3.6.

From the frequency distribution (*v*DOS) (Fig. 3.12b), the Debye temperature Θ from the harmonic approximation [135] for the 1:3 modulated structure was calculated to have a value of

1853 K. Due to the structural modulation, large unit cell and fluxional motion of the H atoms, it is not realistic to compute the λ explicitly. Therefore, several values of λ between 1.0 and 2.0 were selected at equal intervals, which are within the reasonable range for the λ predicted for H_2S and H_3S. The estimated values of T_c at 200 GPa, calculated using the McMillan equation [74] are given in Table 3.2.

λ	T_c (K)
1.0	107
1.1	123
1.2	137
1.3	151
1.4	163
1.5	175
1.6	185
1.7	195
1.8	204
1.9	213
2.0	221

Table 3.2. The estimated values of the critical temperatures of the modulated 1:3 structure corresponding to different EPC parameters ($\mu^* = 0.1$).

The estimated T_c for $\lambda \geq 1.5$ from 180-220K are obviously comparable with the experimental values for the 'high-T_c phase'. But, this estimation should be taken with caution since

this is only an order of magnitude approximation. Fig. 3.11b represents the phase diagram of the T_c for the Pc structure of H_2S and the comparison to other structures.

3.4 Conclusion

A modulated structure constructed from meandering SH chains and H_3S units is found from compressing a low pressure crystalline phase of solid H_2S using First-Principles metadynamics and molecular dynamics calculations under the experimental conditions, *i.e.* at 200K to 200 GPa. The calculated diffraction pattern matches well with experiment, particularly, reproduced the weak diffraction features previously attributed to sulphur impurities. This structural model conserved the elemental S:H atom ratio and need not to invoke the formation of a number of intermediate crystalline phases with different S-H stoichimetries. The hydrogen atoms are found to be highly mobile. Band structure calculations show the large amplitude H motions affect the temporal topology of the Fermi surface leading strong electron-phonon coupling. The structure is a strong contender for the high T_c superconducting phase.

In a previous study by Li *et al.* [114], the polymeric *Pmc2₁* structure, with a calculated diffraction pattern in good agreement with experiment, was proposed to be the most energetically stable structure of H_2S between 65 and 80 GPa. We therefore chose this structure as the precursor for the metadynamics calculations. Metadynamics simulations were carried out at 80, 100, 150, 190 and 200 GPa at 80K, 200K and 300K. In the case of 80 GPa and 80 K a distorted monoclinic *Pc* structure was obtained, a structure which had remarkable similarity to a structure already predicted by Gordon *et al.* [121].

The electronic band structure of the new crystal structure, *Pc* (acquired from metadynamics calculations) has been discussed in detail in this paper. Following the identification of the *Pc*

structure to be the prospective superconducting state, the electronic structure evolution, lattice dynamics, and electron-phonon coupling of this distorted monoclinic (*Pc)* and modulated structure have been studied at 100,110,120 and 130 GPa using density functional perturbation theory. The critical temperature was found to remain almost constant over the pressure range for the *Pc* structure at 42 K. As for the modulated 1:3 structure, a cursory calculation of the T_c from the Debye temperature gave values which match closely with those gotten from experiments. Therefore, no assumption of SH species with different stoichiometry is needed in this study. The 1:2 ratio between the number of sulfur and hydrogen atoms is sufficient for the description of the superconducting phase. The XRD and estimate of the T_c values calculated for the structures discussed in this chapter indicate that there is a very strong possibility that the *Pc* and modulated structures were the metastable structures synthesized in experiments. Some parts of this work has been published and can be found in Ref. [136].

CHAPTER 4

SUPERCONDUCTIVITY IN FeH$_5$ AT HIGH PRESSURES

A similar version of this chapter has been published as a research article in Physical Review B. The reference is as follows.

- Arnab Majumdar, John S. Tse, and Yansun Yao, "Superconductivity in FeH$_5$", Phys. Rev. B 96, 201107 (2017).

As highlighted in the previous chapter, high-temperature superconductivity at temperatures close to the room temperature is one of the most important and actively pursued frontiers in condensed matter physics. Pressure, is a thermodynamic parameter that can manipulate structures and properties. Therefore, the application of pressure on different materials and the subsequent changes or appearance of novel properties is widely studied. For example, under high pressures, bond lengths change leading to changes in electronic structures and eventual conversion to new phases otherwise unknown earlier. Since, high-temperature superconductivity promises to be one of the primary forerunners to tackle the global energy crisis, it is studied extensively with the hope of being applied soon. In this chapter, one such hydrogen rich material, *e.g.*, FeH$_5$ is investigated for high temperature superconductivity under high pressure.

4.1 Introduction

It was predicted by Ashcroft [137] that monoatomic solid hydrogen will become a superconductor with a high critical temperature (T_c) at a very high pressure. The reason behind this statement was based on several substantial scientifically rigorous arguments. Firstly, the vibrational frequency of the hydrogen atoms will be very high and secondly the Debye temperature associated

with the vibration modes will also be very high. These parameters, *i.e.* increased vibrational frequency and Debye temperature in turn lead to a strong electron-phonon coupling, thus enhancing superconducting potential. Although metallic hydrogen is theoretically a high-temperature conventional superconductor with an electron-phonon coupling strength parameter ($\lambda \approx 2$), however, current estimation shows that metallization of pure hydrogen may require a pressure over 500 GPa [138]. The metallization of hydrogen under compression has been reported in several experiments, but the conclusion is not unanimous and superconductivity was never observed [139-141]. The theory that main group polyhydrides with high hydrogen content are precursors for "pre-compressed" hydrogen was proposed by Ashcroft [79]. In these hydrides, the heavier elements enhance intermolecular interactions between the hydrogen species, inducing band overlapping and/or molecular dissociation, thereby lowering the metallization pressures compared to pure hydrogen. The Debye temperatures of these hydrides are also high which is another requirement for high T_c, and the heavy elements give rise to low frequency phonons which in turn enhance the λ as well. Several theoretical calculations done for covalent hydrides, based on the Bardeen-Cooper-Schrieffer (BCS) theory of superconductivity support this suggestion [11]. Among these studies, H_3S [115], CaH_6 [142], YH_6 [143], LaH_{10} and YH_{10} [144], and rare earth (Sc, La, Pr, *etc.*) hydrides [145] have been calculated to possess a T_c higher than 200 K. Recently, H_2S was compressed to 200 GPa and a T_c of 203 K was observed [18]. As discussed in the previous chapter, there is still no completely unambiguously determined structure of superconducting hydrogen sulfide at high pressure [119, 121,122, 136]. This lack of a confirmed knowledge of the exact crystal structure of various materials at high pressure, creates a lacuna in the proper understanding of the structural features and the superconducting mechanism of crystals. In this chapter, this is one of the gaps that we tried to bridge.

Recently, a FeH_5 polyhydride [36] was experimentally synthesized at 130 GPa by Pépin *et al*. by directly reacting Fe with molecular hydrogen in a diamond anvil cell with laser heating. The crystal structure of FeH_5 is tetragonal with *I4*/*mmm* space group *w*ith a long c – axis. The positions of the Fe atoms were determined from the x-ray diffraction pattern while the H atom positions were predicted from theoretical calculations. Since the shortest H…H separation in this structure is 1.31 Å (as compared to 0.73 Å in molecular H_2), therefore from a cursory examination, it can be concluded that the structure of FeH_5 has an atomic form of hydrogen. The absence of the hydrogen atoms in the molecular form and their arrangement in the form of puckered hexagonal layers is reminiscent of the puckered hexagonal ring structure of metallic hydrogen [146]. The new insight led to the speculation of potential superconductivity in FeH_5, which is verified from first principles electron-phonon calculations. In the subsequent sections, the structure of FeH_5 will be elucidated. This is followed by a discussion on the results of electron-phonon coupling calculations.

4.2 Computational Method

First principles electron-phonon calculations were performed at 130 and 200 GPa. The calculations were performed with the electronic package Quantum ESPRESSO [82]. Ultrasoft (PBE) pseudopotentials [46] for Fe and H were used with an energy cut-off of 80 Ry. Individual phonon matrices were calculated on a $4 \times 4 \times 2$ q-point mesh with a $12 \times 12 \times 2$ k-point mesh for Brillouin zone sampling. The electron-phonon coupling (EPC) parameter and logarithmic average of the phonon frequencies obtained for the abovementioned pressures were calculated within the framework of the Bardeen-Cooper-Schrieffer (BCS) theory [66]. The possibility of a high spin state at 130 GPa was also checked for, using GGA+U ($U_{eff} = U - J = 8.62$ eV, determined from linear response theory [147]) and HSE06 hybrid functional [148].

4.3 Results and Discussion

4.3.1 Crystal and Electronic Structure

The 'effective added electron' (EAE) introduced in Ref. [142] has been proven to be a powerful empirical concept to interpret the structure of hydrogen-rich polyhyrides. The basic concept on which this tool is used is that the electronegativity of molecular hydrogen is similar to that of group 13 and 14 elements [142, 149]. Other hydrides, for example, SrH_n and MgH_n have been successfully described by the EAE concept [150-151]. Electron doping has also been proposed as an effective approach to metallize hydrogen [152]. On being compressed to high pressures, metal atoms have the tendency to lose their valence electrons (donor) which are eventually accepted by the H_2, a process which is analogous to the formation of Zintl-Klemen compounds [149]. When the number of donated electrons exceeds that of receptor H_2, the donated electrons are transferred to the antibonding orbital of H_2, leading to complete dissociation of the molecules into hydrides (H^-). On increasing the number of H_2 electron acceptor, the formation of mixed hydride and polymeric-H (*e.g.* H-cages) moieties is expected. The structural motif of the high pressure forms of solid hydrogen start to emerge when the hydrogen concentration is increased considerably. Previously, this concept had been applied to describe the structural evolution and morphology of hydrogen-rich Ca [142] and Sr [149] hydrides at high pressure. It is expected that the Fe atom is likely to be in the divalent state (*vide supra*) and two valence electrons from each atom will be available for charge transfer for iron hydrides at high pressures. In the unit cell of FeH_5 [36], there are 4 Fe and 20 H atoms (or 10 H_2). Eight valence electrons from the Fe atoms can be transferred to and shared by 10 H_2. Thus, it is obvious to assume that 4 H_2 molecules will accept these electrons and completely dissociate leaving 6 H_2-like molecules. As speculated, indeed in FeH_5 there are 8 monoatomic H atoms ($4c$ (0, ½, 0) and $4e$ (0, 0, 0.4095)) with a minimum H…H

distance of 1.55 Å. On studying the remaining 12 hydrogen atoms located in $8g$ (0, ½, 0.185) and $4c$ (0, 0, 0.230), it is found that they are linked with a shorter H…H distance of 1.31 Å forming two independent graphene-like puckered hexagonal honeycomb layers (Fig. 4.1a). The electron localization function [153] shows (Fig. 4.1b) that there are weak electron localization (0.6) between H atoms forming the honeycomb layer.
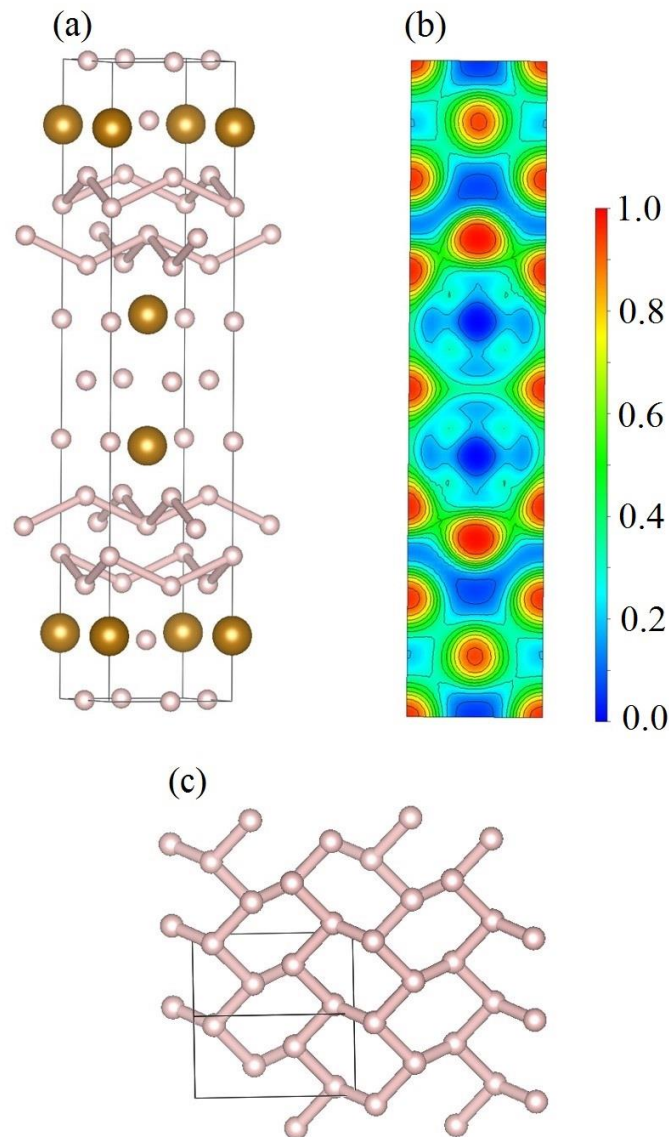

Figure 4.1a) Structure of FeH_5 showing the puckered hexagonal honeycomb layers. b) Plot of the electron localization function with the weak H…H "bonds" of the honeycomb layer highlighted. c) Structure of the high pressure *Cmca* atomic phase of metallic hydrogen [146].

A similar puckered hexagonal honeycomb layer has been predicted in the metallic and superconducting *Cmca* phase of solid hydrogen stable at pressures over 350 GPa [146] (Fig. 4.1c). The oxidation number of FeH_5 was computed following the procedure described previously [154] in order to validate the valence state of the Fe atom. The population of the Fe $3d$ orbital is computed from the projection of the converged total wave onto the atomic Fe d-wave function generated from the construction of the pseudopotential. Fe is found to be in the Fe(II) oxidation state with significant back donation to the Fe atomic orbitals from the surrounding H^- anions.

Cudazzo *et al.* theoretically predicted that the *Cmca* phase of solid hydrogen with a puckered hexagonal honeycomb structure is a high temperature superconductor at high pressure, with T_c = 242 K at 450 GPa [155]. In this structure, the H-H distance is very short at 1.10 Å. The puckered hydrogen layer seen in the *Cmca* phase of hydrogen is similar to that observed in FeH_5 (Fig. 4.1c). The shortest and longest H…H distance in the puckered hexagon of the abovementioned high-pressure phase of hydrogen were calculated to be 0.85 and 0.95 Å. This raised the concern that FeH_5 having a similar structural morphology, although with a longer H…H separation, may also be a potential superconductor. The electronic band structure that was determined in the experimental study [36] revealed that FeH_5 is indeed a metal (Fig. 4.2). The occurrence of steep and flat bands in the vicinity of the Fermi level hints towards possible superconductivity as the presence of flat and steep bands close to the Fermi level is a good indicator of superconductivity as pointed out in Ref. [132]. This further propelled us to determine if FeH_5 has superconducting properties at high pressure and has been discussed next in section 4.3.2.
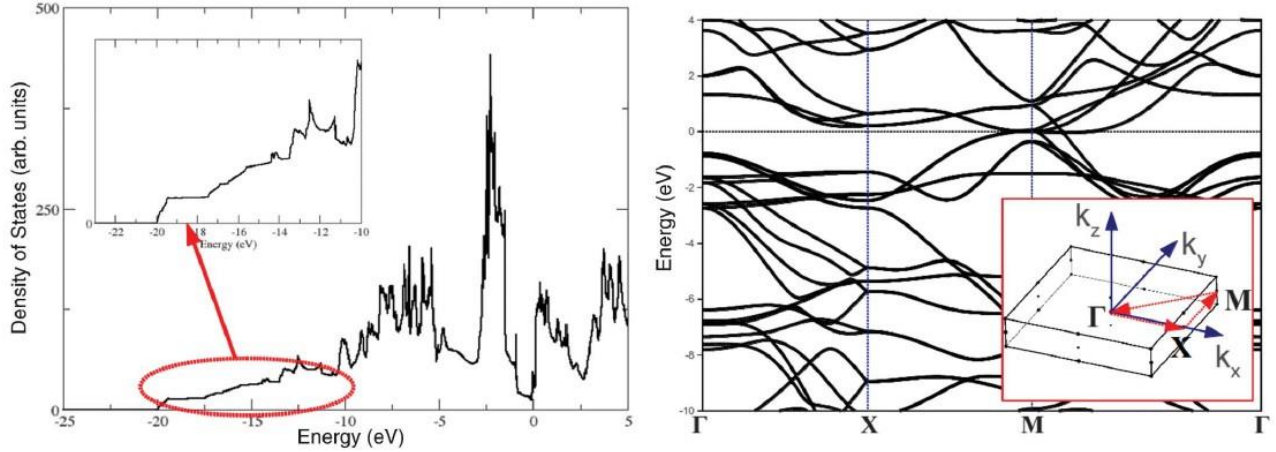
Figure 4.2. (Left) Electronic Density of States of FeH_5 at 147 GPa. (Right) Electronic band structure. This figure has been taken from Ref. [157].

4.3.2 Phonons and Superconductivity

Results of the phonon calculations have been summarized in Fig. 4.3. FeH_5 is seen to be stable at 130 GPa from the phonon band structure. The localized band due to the H...H stretch vibrations at 2250 cm^{-1}, is clearly separated from the translational and librational (bending) modes (Figs. 4.3a and 4.3b). Therefore, there is no strong mixing between the stretch and bent vibrations, which is a key ingredient for large electron-phonon coupling [73], making use of the entire vibrational spectrum, such as in high T_c superconducting polyhydrides H_3S, CaH_6, *etc*. On the contrary, for FeH_5, there is a broad distribution of the translational and librational modes of the hydrogen atoms from 0 to 2100 cm^{-1}. This broad distribution of electron-phonon interactions is reflected in the calculated Eliashberg spectral function, $\alpha^2F(\omega)$ as well (Fig. 4.3c).

Figure 4.3. Calculated phonon (a) band structure, (b) total and projected vibrational density of states and (c) the Eliashberg spectral function of FeH_5 at 130 GPa.
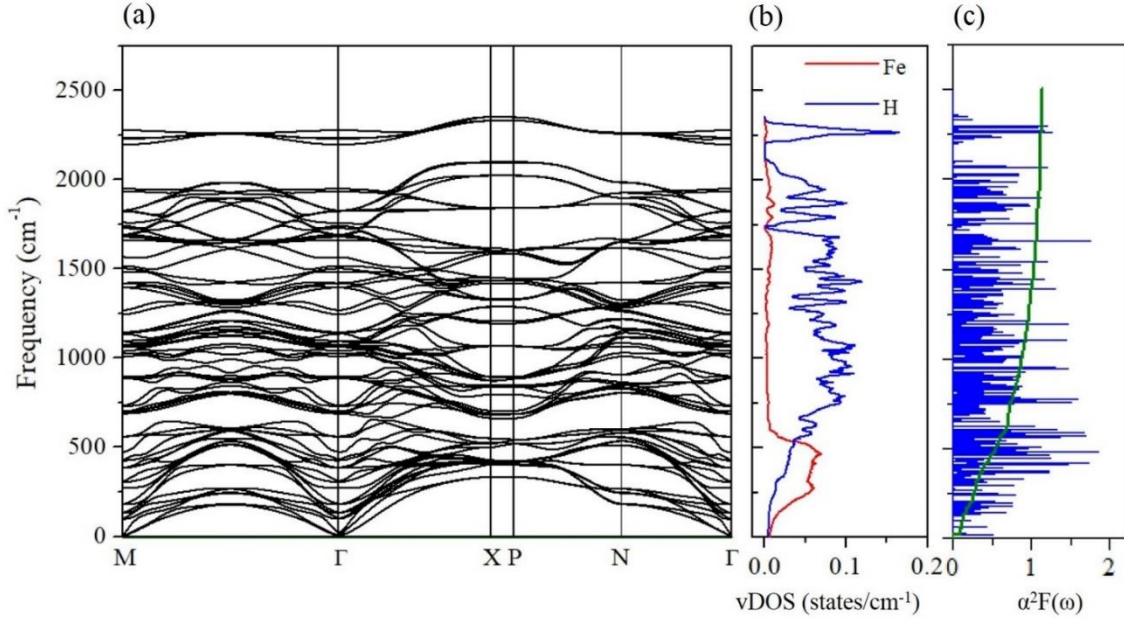
The electron-phonon coupling constant (λ) was 1.13 at 130 GPa and the logarithmic average phonon frequency ω_{ln} was calculated to be 426 cm^{-1} (614 K, or 52.9 meV). Employing the Allen-Dynes equation [76] with a Coulomb repulsion parameter $\mu^* = 0.1$, the estimated superconducting critical temperature was found to be approximately 51 K. Therefore, FeH_5 is indeed superconductive. However, the calculated T_c is much lower than expected and not close to the value predicted for the pure metallic hydrogen *Cmca* phase. From Fig. 4.3, it is evident that phonon modes below 650 cm^{-1} contribute the most to the electron-phonon coupling interactions. This value of 650 cm^{-1} is close to the cut-off frequency of the translational vibrations of the Fe atoms and dominated by the translations and librations of the H atoms in the puckered hexagonal honeycomb layers (8*g* and 4*e*). Compared to the contribution from the H atoms in the puckered hexagonal honeycomb layers, there is relatively small contribution from the monoatomic hydrogen (Fig. 4.4).
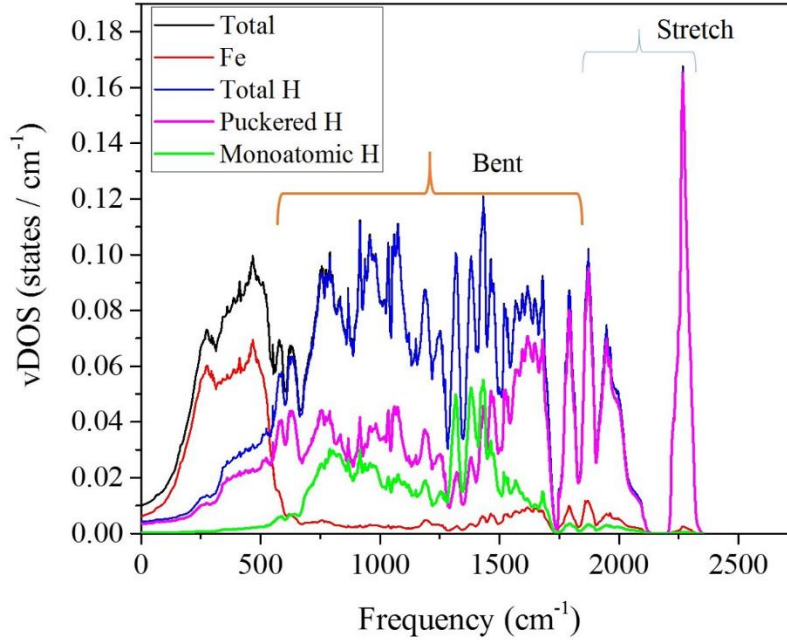
Figure 4.4. Vibrational density of states of FeH$_5$ projected into contributions from H-atoms at different Wyckoff positions.

A lower critical temperature in FeH$_5$ as compared to pure solid hydrogen and recently predicted high T_c polyhydrides (*e.g.* LaH$_x$, YH$_x$, *etc.*) [144] is not surprising. Firstly, H-H stretch and bent vibrations are well separated and Figs. 4.3b and 4.4 showing that these modes did not mix well. The area under the spectral function $A = \int_0^\infty \alpha^2 F(\omega)d\omega$ [73] is equal to 47 meV^{-1} which is much smaller than most high T_c hydrides, such as that in H$_3$S (118.5 meV^{-1}). Secondly, the optimum frequency estimated from the relationship $\omega_{opt} \approx 7k_B T_c$ of 375 cm^{-1} (44 meV) is far from the logarithmic average frequency ω_{ln} of 426 cm^{-1} (*vide infra*). In a recent study [156] it was shown that for polyhydrides with high T_c, a good mixing of the bent and stretched modes is an essential characteristic for ω_{opt} to match well with ω_{ln}. For FeH$_5$ at 130 GPa, the vibrational spectrum is not optimal for efficient electron-phonon coupling due to the relatively large H…H distance of 1.31 Å. Thus, FeH$_5$ structure is compressed to 200 GPa to reduce the H…H contact in order to increase the

mixing of the stretch and bent vibrations. On compressing to 200 GPa, the H…H distance decreased to 1.27 Å but the H...H stretch frequency increased to 2500 cm^{-1} (Fig. 4.5).
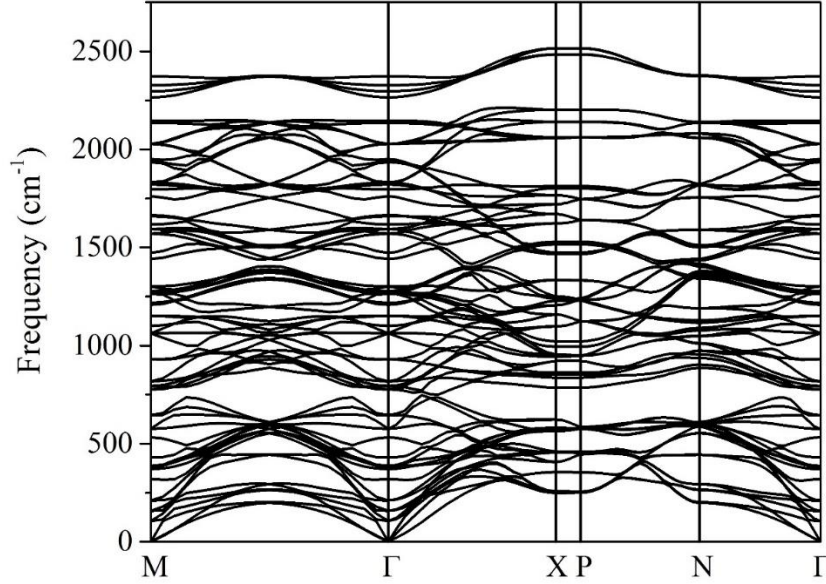

Figure 4.5. Phonon dispersion curve of FeH$_5$ at 200 GPa.

Although the overall phonon spectrum is shifted to higher energy the electron-phonon coupling parameter (λ) got reduced to 1.10, resulting in a lower T_c of 48K. In fact, our results are in very good agreement with the theoretical results obtained by Kvashnin *et al.* [157]. Firstly in Ref. [157], the authors also found a critical temperature close to ours and moreover the critical temperature decreased with increment in pressure. As the pressure is increased, the H...H stretch frequency increases and gets separated more from the bent modes therefore reducing the electron-phonon coupling over the entire spectrum. Instead of raising the average frequency ω_{ln}, it decreases to 600 K. The λ for 130 and 200 GPa have been compared in Fig 4.6. In addition, the electronic density of states at the Fermi level at 130 GPa was calculated to be 21.0 states/eV/f.u, which is higher than 19.5 states/eV/f.u at 200 GPa. The results are testimony to the theory that the electron-phonon coupling in FeH$_5$ is determined by a very sensitive balance of the mixing of stretch and

bent vibrations and not simply by taking into consideration the higher magnitude of the cut-off frequency of the stretch modes.
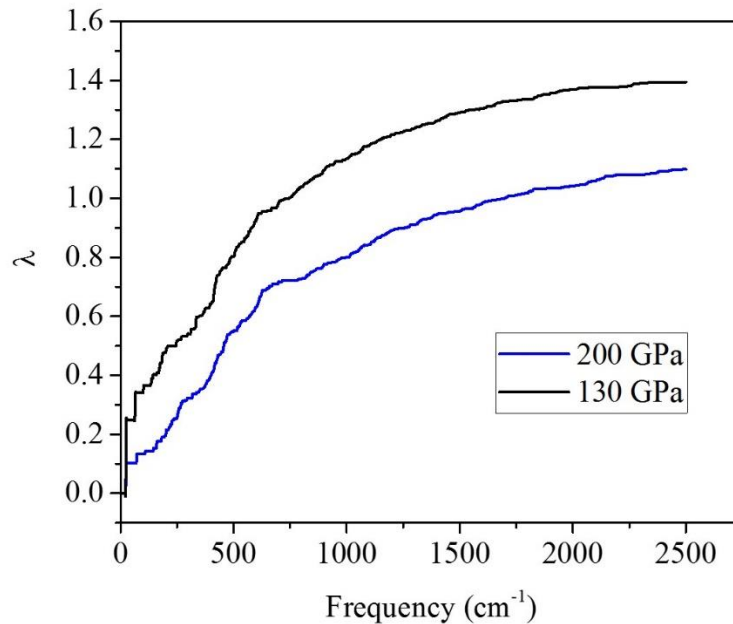
Figure 4.6. A comparison of integrated electron-phonon coupling parameter (λ) of FeH$_5$ at 130 and 200 GPa.

4.4 Conclusion

There are two important conclusions that can be drawn from the predicted superconductivity in FeH$_5$. Firstly, FeH$_5$ is the first high-pressure polyhydride consisting of atomic hydrogen in which the structure is unambiguously determined. The puckered nature of the hydrogen layers is very similar to that of the hydrogen atoms of the solid high pressure *Cmca* phase. From recent theoretical analysis by Tanaka *et al.* [156], the functional derivative of the Eliashberg functions of predicted high T_c metal polyhydrides established that this structural trait is an essential characteristic that utilizes most of the vibrational modes in superconducting hydrogen dominant polyhydrides, in their phonon band structures. Our results presented here are in good agreement

with the above suggestion in accordance with Ref. [156]. Thus, we have illustrated a clear path for a systematic design and engineering of potential high T_c hydrogen-rich superconductors. This work has been published and can be found in Ref. [158].

CHAPTER 5

CHANGE IN THE STRUCTURE AND PROPERTIES OF MOLTEN AND GLASS BASALT AT HIGH PRESSURES

The physical properties of constituent minerals in magma are responsible for the magmatic processes and the origin and stability of deep mantle melts and glasses. Amongst these, the most important ones are the silicate and aluminosilicate materials. SiO_2 (silica) is most abundant in silicates that account for the major portion of the Earth's mantle, including basaltic magma. Basaltic magma is the most common type of magma that erupts on Earth and other terrestrial planets. It is made up mainly of SiO_2 (49.97%), Al_2O_3 (15.99%), CaO (9.62%), and roughly equal amounts of FeO and MgO (~7%). It plays a primary role in the properties of minerals and melts at mantle conditions. Both experimental and theoretical studies have been carried out extensively on these types of materials. The results of these studies suggest that as pressure increases, the coordination between the cations and anions increases as well. These structural changes are responsible for rapid initial melt densification on compression thereby making basaltic (fine-grained volcanic rock) melts possibly buoyantly stable at various depths. Silicate liquids play an integral part at all stages of deep Earth evolution, ranging from formation of the different layers of the Earth billions of years ago to present-day volcanic activity. In order to model this multi-billion year process, one requires knowledge of the structural changes and compression mechanisms that take place in liquid and glass silicates and aluminosilicates at the extremely high pressures and temperatures within the interiors of the Earth. In recent years, structural and density information for silica glass were obtained up to very high pressures, which paved the way for getting data on the molten state too. The SiO_2 reference system holds great importance for understanding the

density, compressibility, and various other properties of the more complex silicate melt compositions that can be found in the deep interior of the Earth. In this study, we performed *ab initio* molecular dynamics calculations to mimic the mantle conditions. The glass structure of basalt was simulated at a temperature of 300 K while the molten state was studied setting a temperature of 2200 K. Structural changes, compressibility and transport properties have been reported in this chapter.

5.1 Introduction

Basalt is defined as a fine-grained igneous rock which is commonly seen in lava flow and is the most abundant type of rock that underlies the Earth's surface. It generally contains 49.97 % of Silica (SiO_2), 15.99 % of Alumina (Al_2O_3), 9.62 % of CaO, 6.84 % of MgO and 7.24 % of FeO as the major components [159]. TiO_2, MnO, Fe_2O_3, Na_2O, K_2O and P_2O_5 are also present in small concentrations. The majority of the Earth's ocean basins are underlain by basalt. Although basalt is much less common on continents and is predominantly found along ocean basins, lava flows and flood basalts underlie some of Earth's land surface too. The basalt found on Earth is formed in three different kinds of regions. They are oceanic divergent boundaries, oceanic hotspots and mantle plumes, and hotspots beneath continents. Oceanic divergent boundaries are locations above rising convection currents where plates move away from each other. This process gives rise to mid ocean ridges and a deep fissure opens up. The extremely hot mantle materials underneath rise up through this fissure as magma. The second type of region is the oceanic hotspot which is basically postulated to be a narrow stream of hot mantle rising from the Earth's core mantle boundary. Basalt production at these locations starts with an eruption on the ocean floor. Repeated eruptions can build the volcanic cone larger until it attains enough height and becomes an island. All the Hawaiian Islands were built up from basalt eruptions on the sea floor. The last kind of region is continental

plumes which are fissures or channels leading the basaltic material on to the Earth's continental surface. Silicate and aluminosilicate glasses and melts (components of basalt) have been at the forefront of research in the geo-physical/chemical community as they comprise the major portion on and beneath the surface of the Earth, lunar crusts and meteorites [160]. The addition of alkali or alkaline-earth cations (Li, Na, K, Ca, and Mg) brings about several changes in their properties, manifesting their importance in fields such as bioactive glasses, laser optics for initiating fusion reactions, thick-film packaging, optical discs, medical and dental implants, *etc.* [161-163] The experimental determination of structural properties of these materials at the mantle conditions is quite challenging [164-165]. Owing to the assumption that the glass (quenched melt) structure is similar to that of the melt at/near the glass transition, therefore to work around the experimental challenges, researchers study the corresponding glass phases and draw parallels with the properties that are characteristic of the relevant mantle melts [166-170]. Liquid silica is one of the most abundant components of geophysically important melts (magmas). In spite of the mantle mostly being solid, there are several studies which hint at the early stages of the Earth's mantle to be mostly molten [171-175]. At the core mantle boundary (~ 135 GPa, 4000 K and 2890 Km below the surface of the Earth), it has been proposed that partial melts exist [160, 174]. Knowledge of silicate and aluminosilicate liquids over the large range of pressure and temperature in the Earth's mantle is crucial to understand in order to better explain magma generation and transport, as well as the chemical and thermal evolution of Earth [176-177]. Recent models of a crystallizing magma ocean have shown the importance of the Earth's earliest evolution of some basic properties of silicate liquids at high pressure, including the density contrast with respect to coexisting solids [178]. It is very important to understand the origin and fate of the melts at various depths as they can give a lot of information, *e.g.* the density determines whether the melt will rise or sink and the diffusivity and viscosity are determining factors of the rate of cooling and transport of magma.

Despite a deep interest in understanding the structure and various properties of glasses and melts at mantle conditions and several studies, both experimental [166, 168, 170, 179-183] and theoretical [184-191] studies being available in literature, a clear and unambiguous explanation of the structural and density changes is yet to be put forward. In all the theoretical and experimental studies, it has been found that amorphous silicates and aluminosilicates (both glass and melt) undergo coordination changes on being subjected to pressure. Both silicon and aluminium with respect to oxygen atoms transform from a tetrahedral structure to an octahedral local environment. However, a rather exact pressure and temperature magnitude is not known for the onset of the structural changes. Scientists have been interested in fathoming whether four fold and six fold coordinated Al and Si atoms can exist simultaneously during the structural transition. Another intriguing hypothesis is the co-existence of five-fold coordination as an intermediate state along with the tetrahedrons and octahedrons [192]. This is important as the presence of five-fold coordinated Si and Al atoms has been proposed to be responsible for affecting the mobility.

The variation of density as a function of pressure is significant to model the earth's interior. The density profile can shed light on the solid–liquid density crossover, chemical stratification, *etc*. However, experimental data even on the density of melts and glasses at lower mantle conditions are limited rendering the comparison of melts and glasses difficult. As previously stated, density contrasts between silicate liquids and solid mantle essentially determine the stability and mobility of melt at depth [174, 193]. Structural metamorphosis on being compressed can influence the melt density, and other properties including the melt viscosity and element partitioning. Thus, reliable results (experimental and theoretical) are essential. The transport properties *e.g.* viscosity of aluminosilicate melts is one of the key factors that determines the dynamics of our planet and other celestial objects with similar rock formation that on Earth. It affects the equilibration between sinking metals and the surrounding silicate melts after an impact and strongly influences the

cooling time of the magma ocean of the early Earth gradually giving rise to solid rocks [194-195]. Some of the experimental and theoretical studies that have reported transport properties of silicate melts can be found in Refs. [196-202]

Due to the similarity in composition to natural magma, structural and transport properties of silicate and aluminosilicate glasses and melts have been a very interesting topic of research [203-206]. To have a more fundamental and detailed mechanism of structural change and transport of natural magma, besides difficult experimentation at the conditions of deep interior, first principles computation is performed on compositionally simple systems. Natural melts represent multi-component systems consisting of CaO, MgO, Fe, Fe_2O_3, Na_2O, K_2O, Al_2O_3, TiO_2 and SiO_2. Certain minerals such as diopside ($CaMgSi_2O_6$) and anorthite ($CaAl_2Si_2O_8$) (melt and glass) have been studied both experimentally and theoretically [207-211], together giving a comprehensive explanation of structural changes and transport properties associated with densification.

In this chapter, a basalt system consisting of CaO, MgO, Al_2O_3 and SiO_2 has been subjected to AIMD simulations. The glass system was studied at 300 K and at pressures ranging from 0 to 80 GPa. Similarly, the melt system was studied at a similar pressure range as that of the glass and 2200 K. The main goal of this chapter is to unravel the structural transition, *i.e.* coordination and bond length changes, and relating the structural properties to the density, bulk velocity of sound and the transport properties of both glass and molten basalt at conditions mimicking that of the deep mantle region.

5.2 Glass

5.2.1 Computational Method

Ab initio Molecular dynamics simulation was carried out on a model basaltic glass system. Constant volume and constant temperature (NVT) canonical ensemble was employed along with Nosé thermostat [211]. The simulations were carried using the VASP program [55-57]. The electron orbitals were expanded in the plane wave (PAW) basis set and the PBE [46] functional was used. The kinetic energy cut-off of the plane wave was 400 eV. The interatomic forces are computed for all the time steps from a fully self-consistent solution of the electronic structure to the Born-Oppenheimer surface, within the finite temperature formulation of density functional theory. The stoichiometry of the basaltic material studied was $Ca_{22}Mg_{14}Al_{16}Si_{44}O_{148}$. A cubic supercell with a total of 244 atoms was considered. Owing to the large size of the unit cell and computational limitations, we ran all the simulations using just one k-point (Γ) to sample the Brillouin Zone. For this glass system, simulations were performed at approximately 0, 4, 8, 12, 14, 25, 36, 47, 58, 68 and 79 GPa and 300 K. The time step that was used for the integration of the equation of motions was chosen to be 1.0 fs. All AIMD simulations were performed for at least 50 ps.

5.2.2 Results and Discussion

5.2.2.1 Convergence

In order to compute reliable equilibrium properties, MD simulations ran for more than 50000 fs. But before we could perform any analysis on the trajectory of the atoms stored, we checked the convergence of our calculations. As already mentioned, calculations were performed in the NVT ensemble; therefore, the volume was constant. It is necessary to check for convergence

of the temperature, pressure and energy. Fig. 5.1 shows the plots of the temporal evolution of these quantities at 4 GPa. It can be seen from the pressure and energy graphs, that approximately after 10000 fs, the calculation has converged. Therefore, the first 10000 steps were removed and all subsequent calculations were done using the remaining number of steps. This is good practice to see if the values are converging to the numbers desired. For example in Fig. 5.1a, it can be confirmed that the temperature is indeed very closely oscillating about 300 K giving an average of 300 K. Similarly for pressure (Fig. 5.1b), the isotropic stress has converged to an average value of 4 GPa after approximately 10000 fs.
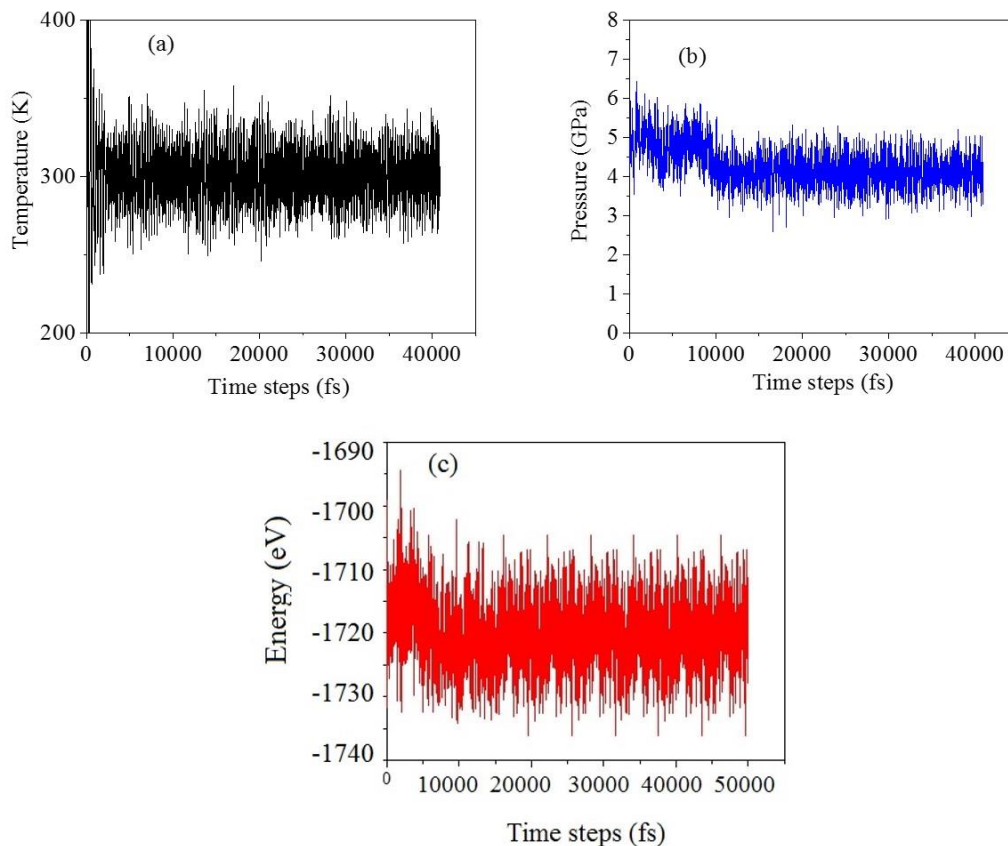

Figure 5.1 a) Temperature vs time, b) Pressure vs time, and c) Energy vs time to confirm the convergence of the calculations of basalt glass at 4 GPa and 300 K in an NVT ensemble.

5.2.2.2 Structural Transformation

We will show that there are several transitions by studying the structures of the basaltic glass. From Fig. 5.2a, it is evident that the Si atoms are 4 fold coordinated with oxygen atoms at ambient pressure forming SiO_4 tetrahedrons. When compressed, the coordination number remains 4 until 15 GPa. Above 15 GPa, the average coordination number increases at the cost of the four fold coordination. As shown in Fig. 5.2c, there is a mixture of five and six fold coordination. This mixed coordination is observed until 47 GPa at which the remaining four fold coordination is gradually replaced by six fold coordination. Above 47 GPa, the predominant number of nearest oxygen neighbours of silicon is six. This indicates the completion of the gradual structural transition of the glass from four to six fold coordination. The coordination change with pressure is shown in a separate section later on.
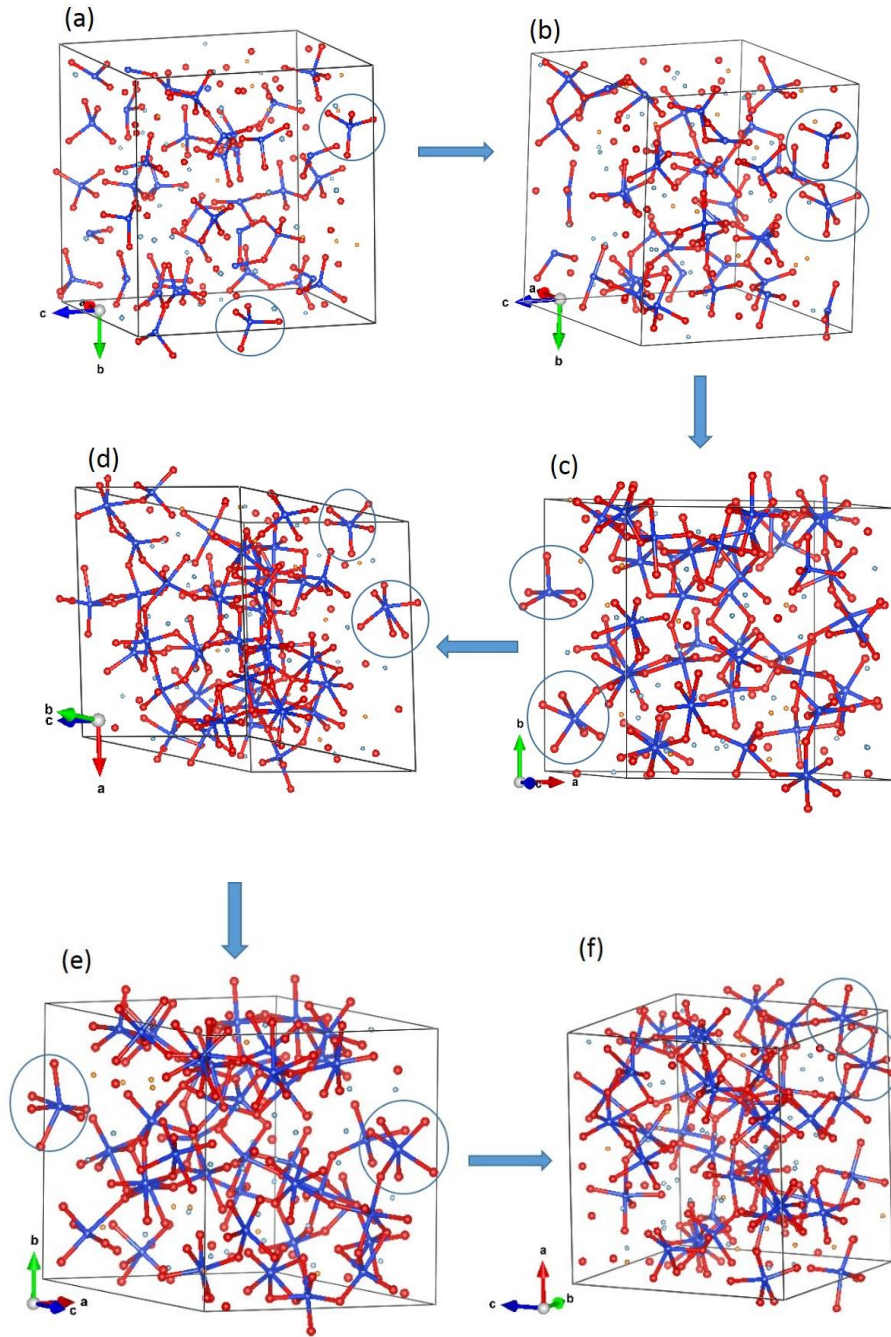
Figure 5.2 a-f) Snapshots of the structure of Basalt glass at 0, 14, 36, 47, 68 and 79 GPa respectively. The blue sphere are Si and the red spheres are O. The structural transition of the Si-O coordination has been shown with increasing pressure.

The structural change with respect to the aluminium and oxygen bonding has been shown in Fig. 5.3. For aluminium, like other aluminosilicate glasses [207], the change of coordination from 4 to 5 occurs in a very narrow pressure range. As can be seen in the sequential diagram below (Fig. 5.3a-f), that by 15 GPa, the four fold coordination drops sharply and Al atoms become mostly six-fold coordinated with oxygen atoms. This six-fold coordination, however doesn't change rapidly and gives rise to AlO_6 octahedrons within a small pressure window. A small concentration of five-fold coordinated aluminium atoms can be seen between 15 and 69 GPa. At around ~70 GPa, a considerable amount of seven fold coordination can be seen, hinting that at greater pressures, transition to even higher coordination may occur.
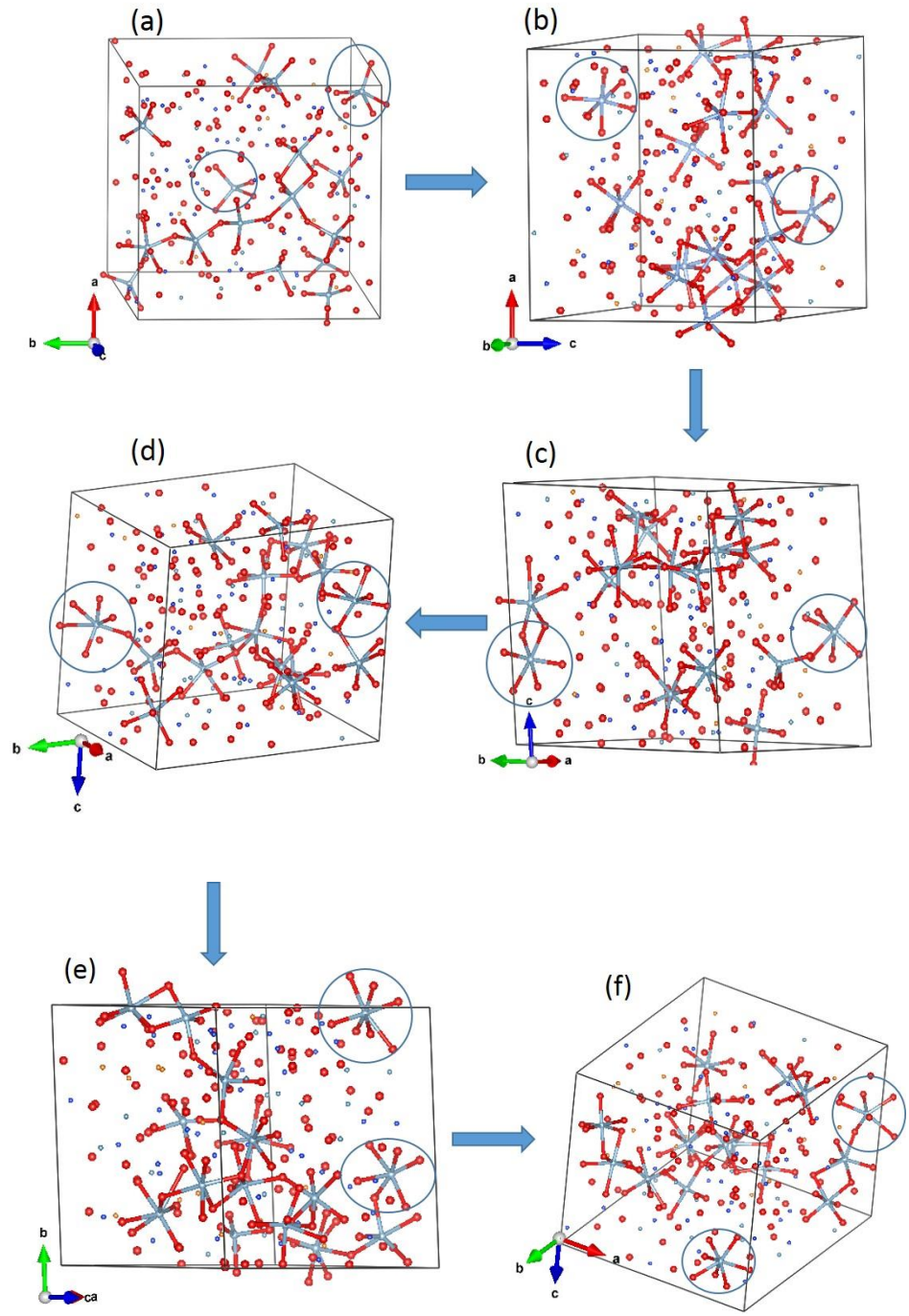
Figure 5.3 a-f) Snapshots of the structure of Basalt glass at 0, 14, 36, 47, 68 and 79 GPa respectively. The blue spheres are Al and the red spheres are O. The structural transition of the Al-O coordination has been shown with increasing pressure.

5.2.2.3 Radial Distribution Function

A closer examination of the nearest neighbor structure is revealed in the plots of the Radial Distribution Function (RDF). The calculated RDF displays well-defined sharp first peak for all cation–anion pairs. The RDF of Si-O are plotted in Fig. 5.4a for all the pressure points at which simulations were performed. The nature of the RDF matched extremely well with those in Refs. 168 and 214 for the case of SiO_2 glass. The first peak represents the nearest neighbor distance and the area underneath a peak of the RDF provides the information of the coordination number. The cation-oxygen bond length is a characteristic parameter of the network structure of amorphous silicate and aluminosilicate materials. In this case the Si-O bond length is shifted to a lower value from ambient to 15 GPa and the reverse trend is observed at higher pressures. The Si-O bond length of the basalt melt at ambient pressure is 1.63 Å and decreases to 1.61 Å by 15 GPa where the four fold coordination of the Si atoms is still dominant (*vide infra*). This is to be expected as, with compression, the bonds are shortened. However, once the structural change to high Si-O coordination commences, the bond length increases to accommodate more neighboring oxygen atoms. At 25 GPa and higher pressure, when the transition from SiO_4 to SiO_6 is largely completed, the silicon-oxygen distance is 1.66 Å. Then it decreases gradually with increasing pressure as the material gets compressed and there is no drastic change in the coordination. The nearest neighbour Si-O distances are plotted in Fig. 5.4b and compared with the results from other studies [191, 207 and 214]. The trend of the values that we obtained from our MD simulations are in very good agreement with other silica glasses. Anorthite ($CaAl_2Si_2O_8$) glass has also been considered for comparison as it an aluminosilicate containing calcium thus mimicking our system to a good extent. In essence, the initial dip in the bond length till 15 GPa is due to compression, followed by an increase in the bond length (till 25 GPa) which signifies coordination change or structural

transition. Increase in coordination number is always marked by an increase in the bond length. From 25 to 70 GPa, the Si-O distance remains almost unchanged. At higher pressures there is another dip which is once again due to the reduction in the volume of the octahedron structure.
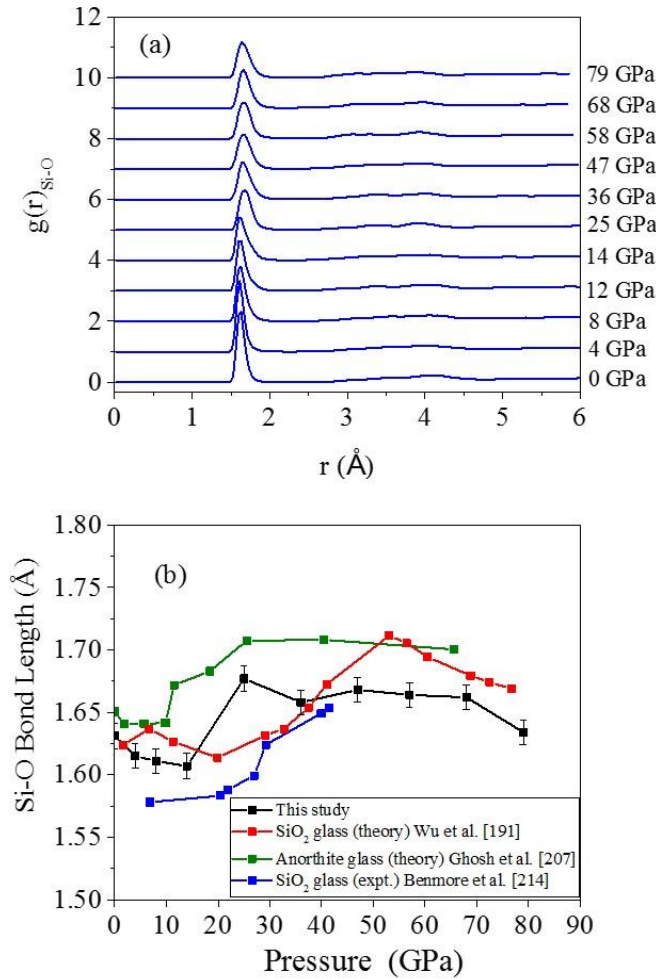

Figure 5.4 a) The RDF of Si-O at increasing pressure and b) Si-O bond length vs pressure for basalt glass.

Fig. 5.5a shows the RDF for Al-O. At 0 GPa, the Al-O bond length is 1.75 Å and shifts to a higher value at 15 GPa. This is expected and will become even much clearer in the next section when the coordination numbers are plotted as a function of the pressure. The above trend is similar to that observed for Si-O bonds, *i.e.* on compression from 0 to 15 GPa, the tetrahedron polyhedral almost disappear accompanied by the emergence of five and six fold coordination. From 0 to 15

GPa, there is a rapid fall in the four fold coordination but the five-fold coordination is mainly present. To fit in more nearest neighbours, the Al-O bond length increases to approximately 1.81 Å. However once the transition to the octahedron (AlO$_6$) phase was completed, the bond length decreased to 1.75 Å once again due to decrease in volume. One would expect the bond length to decrease on further compression. On the contrary, we notice that even at 58, 68 and 79 GPa, the bond length remained almost constant at 1.75 Å. Even at the emergence of seven-fold coordination (*vide infra*). The nature of the evolution of the Al-O bond length is illustrated in Fig. 5.5b.
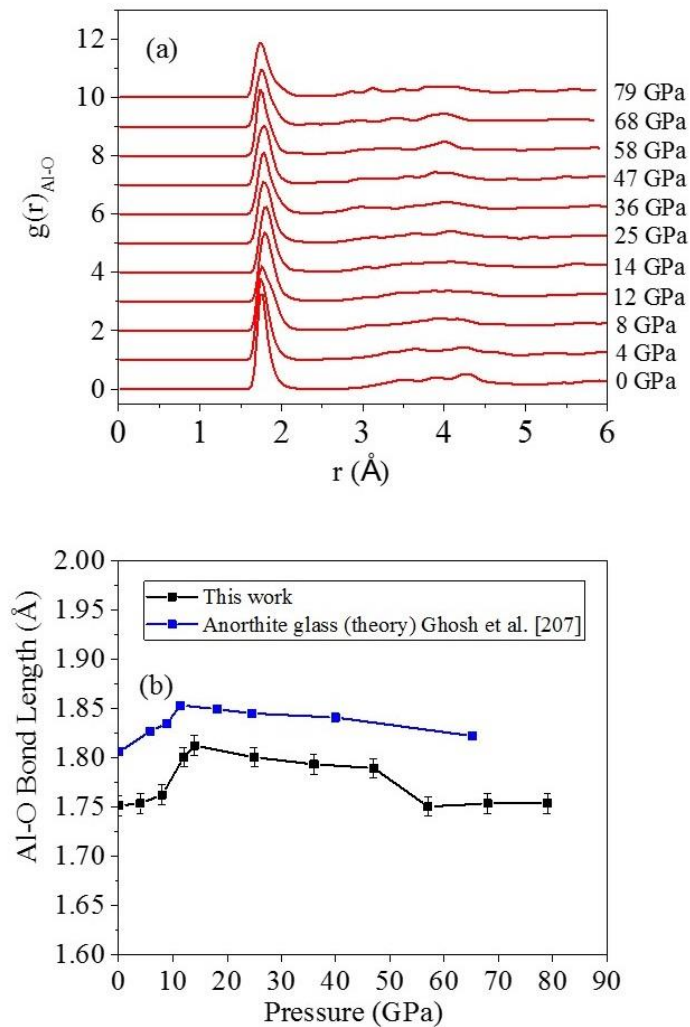
Figure 5.5 a) The RDF of Al-O at increasing pressure of basalt glass and b) Al-O Bond Length vs Pressure of basalt glass.

From Fig. 5.6a and b, it is evident that unlike Al and Si, the bond length between calcium and oxygen keeps decreasing with pressure. Specifically, after 20 GPa, the bond length falls much faster. Once again this trend is in agreement with the results obtained by Ghosh *et al.* [207]. The average Ca-O bond length at ambient pressure is 2.29 Å and it remains almost constant up to 20 GPa. Above 20 GPa, Ca-O distance starts decreasing with pressure. Although, both for anorthite glass [207] and our work the MD simulations were performed at 300 K, it can be noted that for Si, Al and Ca, there is consistently a 0.5-1 Å difference in the bond lengths. This is possibly due to the fact that different approaches have been used to interpret the bond lengths from the RDF. Therefore, the difference is approximately constant and the trend gives useful information about the coordination environment. Notably, in crystalline anorthite, Ca maintains a distorted polyhedral surrounding with seven nearest-neighbor oxygens that have an average bond distance of 2.49 Å [215].
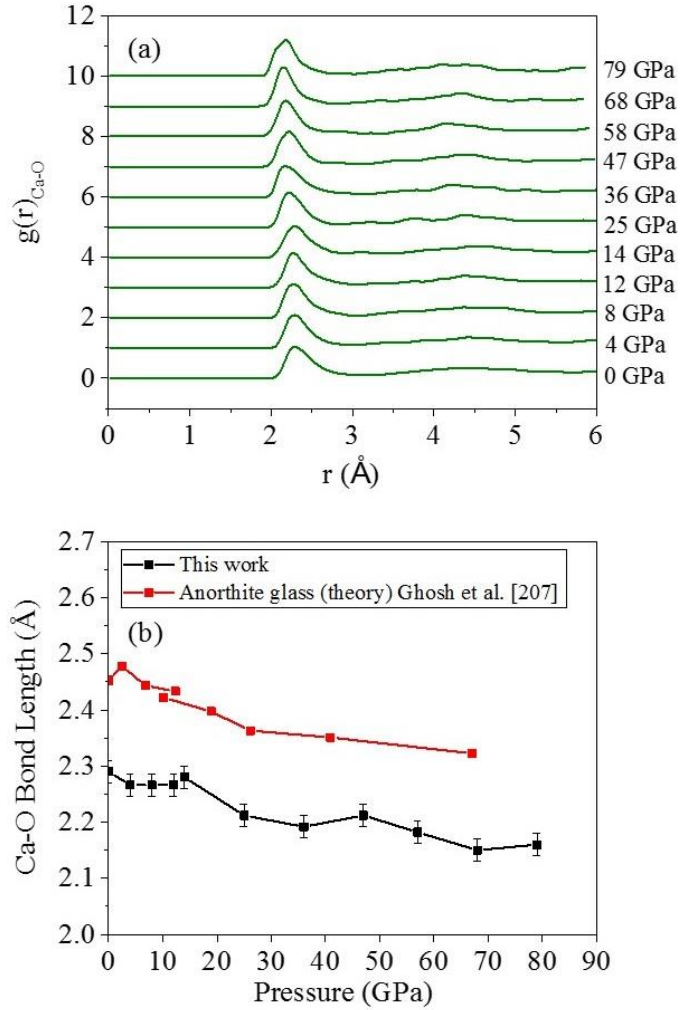
Figure 5.6 a) RDF of Ca-O with increasing pressure and b) Change in Ca-O bond length with increasing pressure for basalt glass.

Similar to Ca, the bond length of magnesium and oxygen atoms in the glass structure also almost constant until approximately 25 GPa and then starts to decrease owing to the compression. After around 25 GPa, the Mg-O bond length falls steeply and attains a comparatively stable value of roughly 1.89 Å. This trend and the bond lengths match well with the Mg-O bond lengths found for diopside melt in a theoretical study by Sun *et al.* [208]. The Mg-O bond length in our basalt system has been compared to that of diopside ($CaMgSi_2O_6$). Hence, chemical formula wise, it is

close to basalt and suitable for comparison. Unlike Si and Al, the bond lengths of Ca and Mg with oxygen are much longer due to the larger ionic radii.
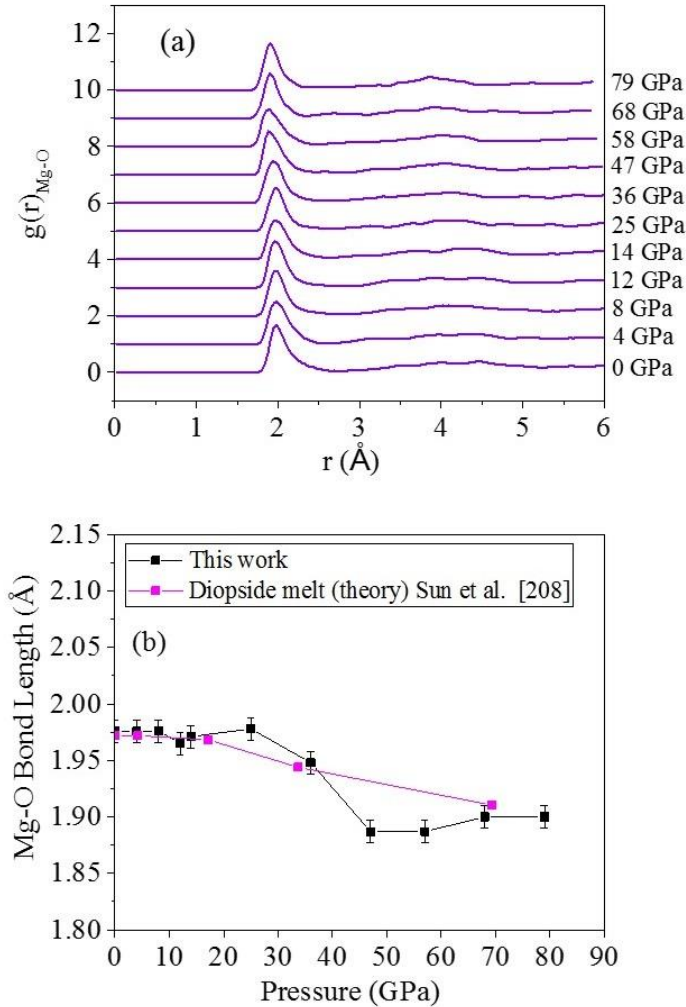

Figure 5.7 a) RDF of Mg-O with increasing pressure and b) Change in Mg-O bond length with increasing pressure for basalt glass.

5.2.2.4 Coordination Number

It is believed that in silica and alumina, the glass structure is largely controlled by cation–anion bonding so the structural changes due to pressure, temperature and composition can be better

characterized in terms of coordination environments consisting of different cations and anions. As pressure rises, the calculated mean Si–O coordination increases relatively gradually initially from fourfold (at zero pressure) to six fold at high pressure in a remarkably similar way for the basaltic compositions studied in Ref. 165. It is essential to study coordination change of the cations with respect to oxygen atoms to better understand the structural, thermal and transport properties. Densification at lower pressures is attributed to the flexibility of the silicate network but has a limit because eventually atoms are so closely packed that further compression involves bond shortening and coordination changes. Structural transformations are due to the increased stability of the higher cation-anion coordination at high pressures. The evolution of the coordination number of silicon atoms with respect to oxygen atoms is shown in Fig. 5.8a. The basaltic glass like most other silicate glasses has four fold Si coordination with oxygen at ambient pressure. With the onset of densification, from approximately 15 GPa, there is clearly a mixed four and five-fold coordination. This is apparent in Fig. 5.2, where the structural change of the unit cell was shown at consistent pressure intervals. The coordination number increment from four keeps happening smoothly up until 40 GPa, after which it becomes a mix of five and six fold coordination which is somewhat similar to silicate glass [216]. At higher pressures, above 50 GPa, the transformation from four fold (tetrahedron) to six fold (octahedron) coordination is largely completed. The average coordination has been plotted in Fig. 5.8b. The increment of the value from 4 to 6 is rapid between 0 and 15 GPa and above 15 GPa the increment is more slow. This increase in the coordination number will manifest its effects on other further properties (density, compressibility, *etc.*) too as will be seen in the following sections.
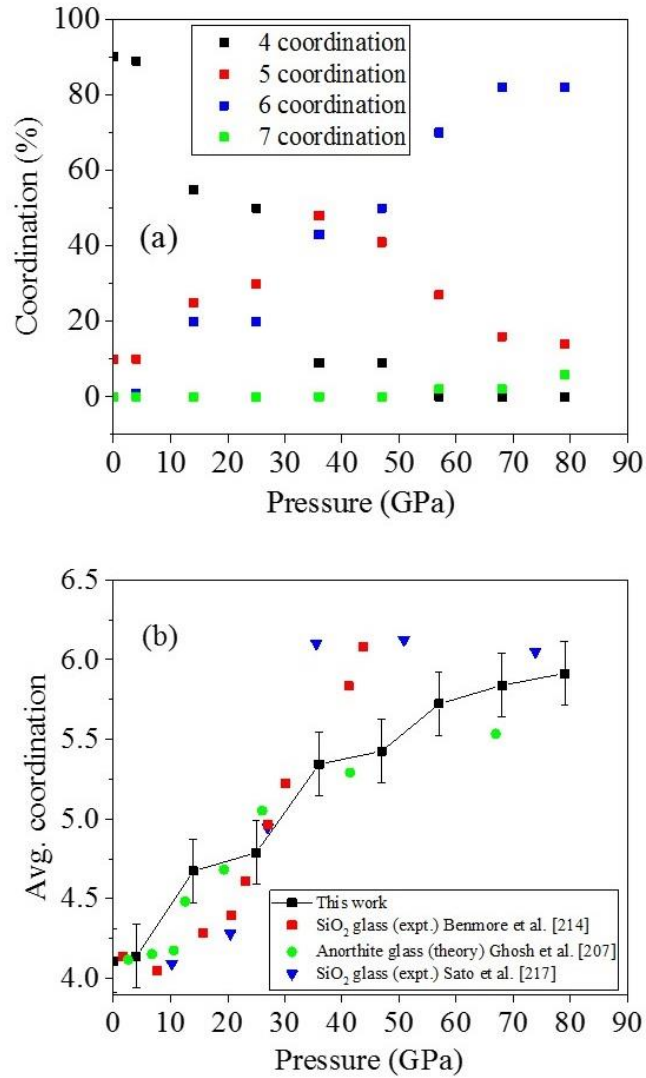
Figure 5.8 a) Coordination percentage vs pressure of Si atoms with respect to O atoms, b) Average Si-O coordination number vs pressure compared with other works dealing with silicate glasses.

The aluminium coordination number change with respect to oxygen atoms is much sharper compared to Si atoms, as is evident in Fig. 5.9a. For alumina or aluminosilicate materials, at ambient pressure, there is a mixture of both four and five-fold coordination of Al atoms with O atomns. The Al-O bond is not only longer than the Si-O bond, but weaker too. In several studies, continuous breaking and reforming of Al-O bonds has been observed. This leads to an undulation

in the usual increment or decrement of the five-fold coordination of the Al atoms. By 15 GPa, the four fold coordination has almost vanished and the five-fold coordination becomes dominant. This is in agreement with the literature for aluminosilicate liquids [218]. Above approximately 50 GPa, seven coordination can also be seen to be arising and by 80 GPa, it comprises a considerable percentage of the coordination.
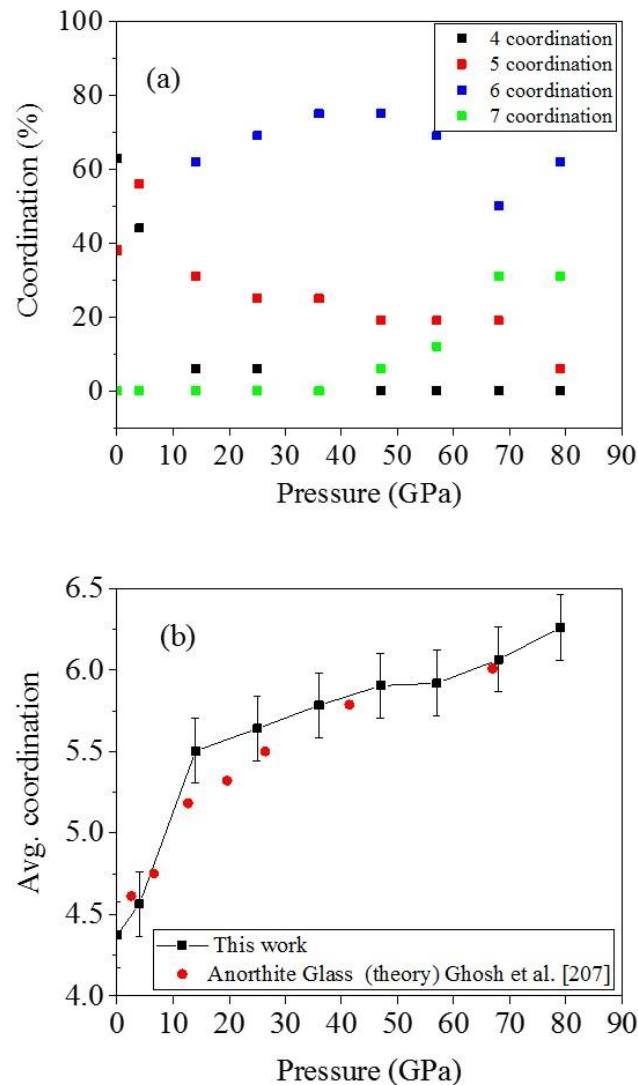

Figure 5.9 a) Coordination percentage vs pressure of Al atoms with respect to O atoms, b) Average coordination number of Al atoms vs pressure of basalt glass.

5.2.2.5 Equation of State (EOS)

The pressure-volume relation of basaltic melt is shown in Fig. 5.10. The points are fitted using the 4th order Birch Murnaghan (BM) equation of state which takes the form of Eq. (5.1).

$$P = 3K_0 f_E (1 + 2f_E)^{5/2} \left[1 + \frac{3}{2}(K' - 4)f_E + \frac{3}{2}\left(K_0 K'' + (K' - 4)(K' - 3) + \frac{35}{9} \right) f_E^2 \right]. (5.1)$$

K_0 is the zero pressure bulk modulus, K' is the pressure derivative of the bulk modulus, K'' is the second derivative of the bulk modulus with respect to pressure and f_E is the Eulerian strain and is given by,

$$f_E = \frac{\left[\left(\frac{V}{V_0} \right)^{\frac{2}{3}} - 1 \right]}{2}. \tag{5.2}$$

The fit results are as follows. The ambient pressure volume (V_0) is 3111 $\mathring{A}^3$, bulk modulus (K_0) is equal to 25.1 GPa and the pressure derivative of the bulk modulus is 5.0.
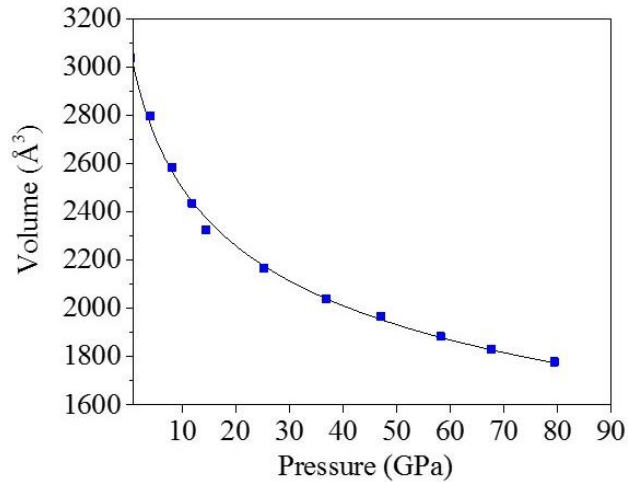

Figure 5.10 P-V curve of basalt glass fit with 4th order BM EOS fit.

Common EOS fits such as the Birch-Murnaghan or Vinet are of limited theoretical validity for glasses and melts, where densification occurs for a large part through configurational changes. However, they are useful for interpolation between data but extrapolations far beyond the experimental data are often erroneous. Below and above 15 GPa, the compression mechanisms are different. For pressures below 15 GPa, the volume falls sharply and this decrement becomes slower at higher pressures. This structural change is a gradual and continuous one.

Density measurements of amorphous material are key for constraining the density contrast in planetary interiors. Such information is extremely valuable to understand the internal dynamics and reproduce the thermo-chemical evolution and history of the different layers of the Earth and other rocky planets. As expected, from Fig. 5.11, the density of the basalt glass increases with pressure. Similar to the P-V curve, the increase in the density between 0 and 15 GPa (approximately) is much more rapid than at pressures above 15 GPa. This value is in agreement with both experimental and theoretical studies of silica [170, 191]. At higher pressures, the increase in the density is rather sluggish owing to high compaction, with an overall almost two-fold increase in the density within the pressure range of 0 to 80 GPa. In the investigated range of pressure points, no inversion of density was noted for the basalt glass either. From Fig. 5.11, it can be seen that the density obtained from our calculations is in excellent agreement with the density calculated in the simulations performed by Ghosh *et al.* for anorthite glass [207].
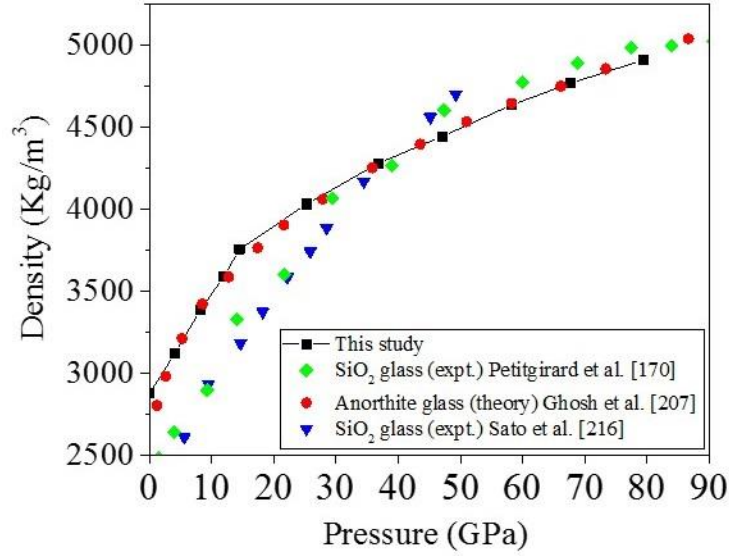
Figure 5.11 Change in density with pressure of the glass structures.

From the BM fit, the first order numerical derivative of the pressure with respect to the volume can be obtained. The pressure derivative is related to the bulk modulus via.

$$K = -V \frac{dP}{dV} \, . \tag{5.3}$$

The pressure interval where the pressure-volume curve is steep, the bulk modulus has a smaller magnitude. This is intuitive as at lower pressure the material can be compressed more, the isotropic compressibility is more. Bulk modulus is the inverse of compressibility. Between 0 and 15 GPa, the volume drop is very high and therefore the bulk modulus is low and the first derivative of the bulk modulus with respect to pressure (K') is 5.0451. In terms of bulk modulus, this pressure domain is characterized by bulk modulus values ranging between 25 and 422 GPa (Fig. 5.12).
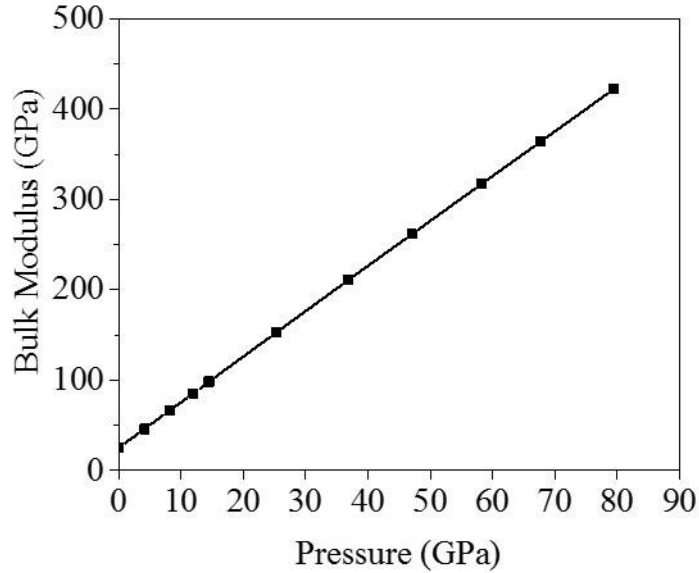
120

Figure 5.12 Bulk modulus as a function of pressure of basalt glass.

Despite excellent agreement in the equilibrium bulk modulus compared to the study by Ghosh *et al.* [207] for anorthite glass, the experimental (Ponitzsch *et al.* [212]) zero-pressure bulk modulus derived from ultrasonic measurements (4–10 MHz) is larger than that of the present study. The acoustic velocity is frequency dependent as found from ultrasonic measurements of silicate liquids [219]. The ultrasonic wave velocity values are higher, resulting in higher bulk modulus. This similar disparity has also been reported in the study of GeO_2 glass by Smith *et al.* [220] and SiO_2 glass by Zha *et al.* [221]

The velocity of sound at bulk is calculated from the formula,

$$v = \sqrt{\frac{K}{\rho}},$$ (5.4)

where K is the isothermal bulk modulus and ρ is the density. The bulk acoustic velocity increases linearly with pressure. From Fig. 5.13, one can see that the values obtained from our MD study is in very good agreement with magnitudes obtained from other MD studies.
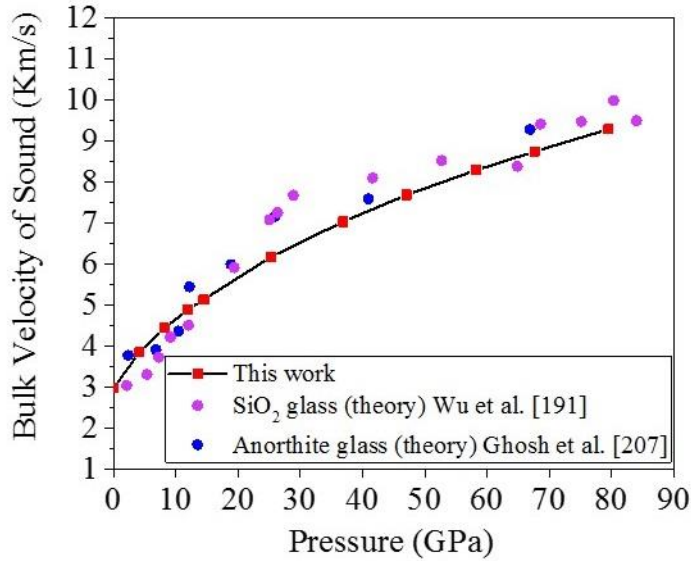
Figure 5.13 Pressure evolution of the velocity of sound of basalt glass.

Similar to the pressure vs density curve in Fig. 5.11, the bulk acoustic velocity rises steeply till 15 GPa (approximately) and eventually the curve becomes more flat at higher pressures. The rapid densification at lower pressures brings the molecules closer and makes it easier for them to vibrate and transfer energy longitudinally, thus making acoustic velocity higher too.

5.2.2.6 Electronic Properties

The electronic density of states (DOS) was determined for the basalt glass at all calculated pressures. Throughout the compression process, no transition to the metallic state was observed. Fig. 5.14 a-d shows the DOS at various pressure points. In fact, on the contrary, the band gap increases gradually from 2.90 eV at 0 GPa to 3.27 eV at 68 GPa.
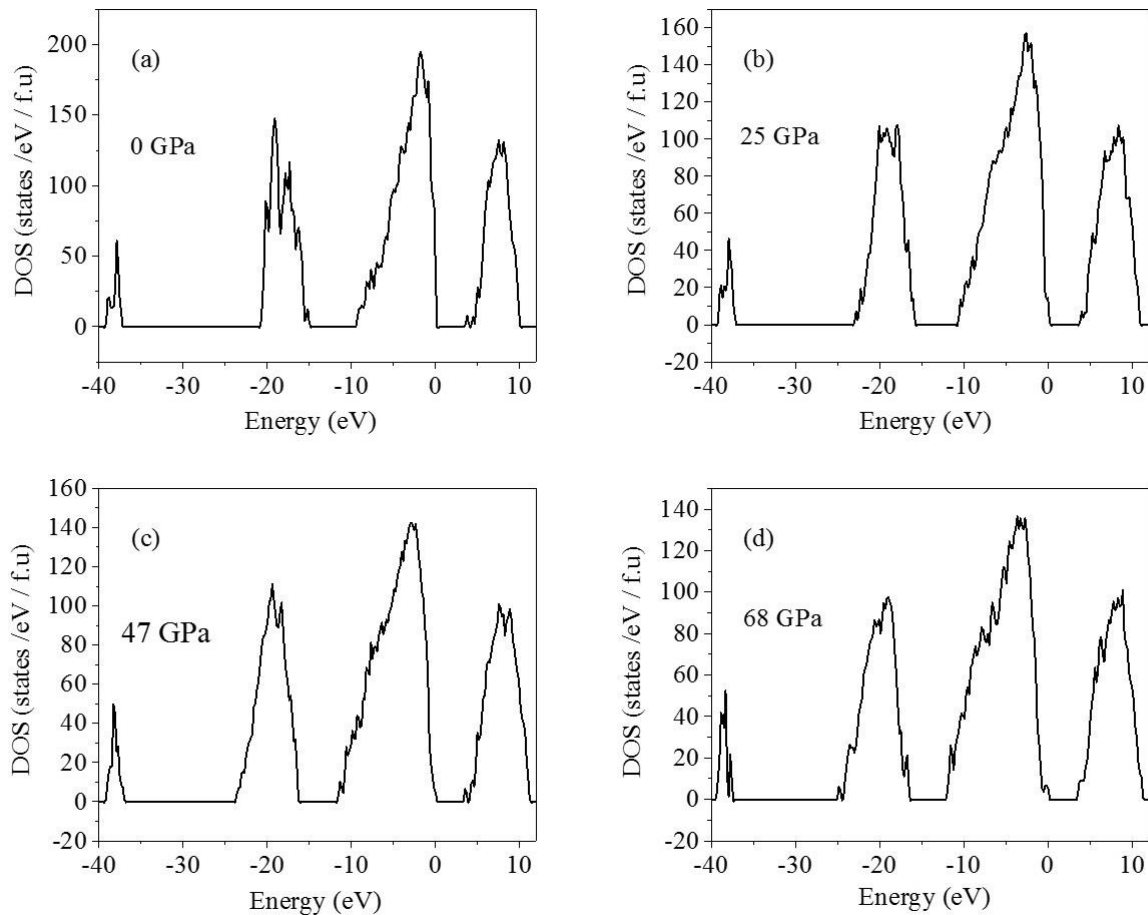
Figure 5.14 a-d) Electronic DOS of basalt glass at 0, 25, 47 and 68 GPa, calculated using PBE XC functional.

5.3 Melt

5.3.1 Computational Method

Same as basalt glass, *ab initio* MD simulation was performed on a model basaltic melt system. Constant volume and constant temperature (NVT) canonical ensemble was employed on a well equilibrated liquid generated from the melting of the solid along with Nosé thermostat [211]. The simulations were carried out using the VASP [55-57] program. The electron orbitals were expanded in the plane wave (PAW) basis set and the PBE [46] functional was used. The kinetic

energy cut-off of the plane wave was 400 eV. The stoichiometry of the basaltic material studied was $Ca_{22}Mg_{14}Al_{16}Si_{44}O_{148}$. The total number of atoms in the cubic unit cell was 244. Owing to the large size of the unit cell and computational limitations, we ran all the simulations using just one k-point (Γ) to sample the Brillouin Zone. For this glass system, simulations were performed at 0, 18, 23, 30, 38, 50, 62, 68 and 82 GPa and 2200 K, similar to the experimental conditions. The time step that was used for the integration of the equation of motions was chosen to be 2.0 fs. All AIMD simulations were performed for at least 50 ps.

5.3.2 Results and Discussion

5.3.2.1 Convergence

Similar to basalt glass, in order to compute reliable equilibrium properties of basalt melt, MD simulations ran for more than 50000 fs. But before performing any analysis on the trajectory of the atoms stored, we checked the convergence of our calculations. As already mentioned, calculations were performed in the NVT ensemble; therefore, the volume was constant. It is necessary to check for convergence of the temperature, pressure and energy. Fig. 5.15 shows the plots of the temporal evolution of these quantities at 0 GPa. It can be seen from the pressure and energy graphs, that approximately after 10000 fs, the calculation has converged. Therefore, the first 10000 steps were removed and all subsequent calculations were done using the remaining number of steps. This measure and care was taken for all the pressure points at which the molten structure of basalt was simulated. For example in Fig. 5.15a, it can be confirmed that the temperature is indeed very closely oscillating about 2200 K giving an average of 2200 K. Similarly for pressure (Fig. 5.15b), the isotropic stress has converged to an average value of 0 GPa after approximately 10000 fs.
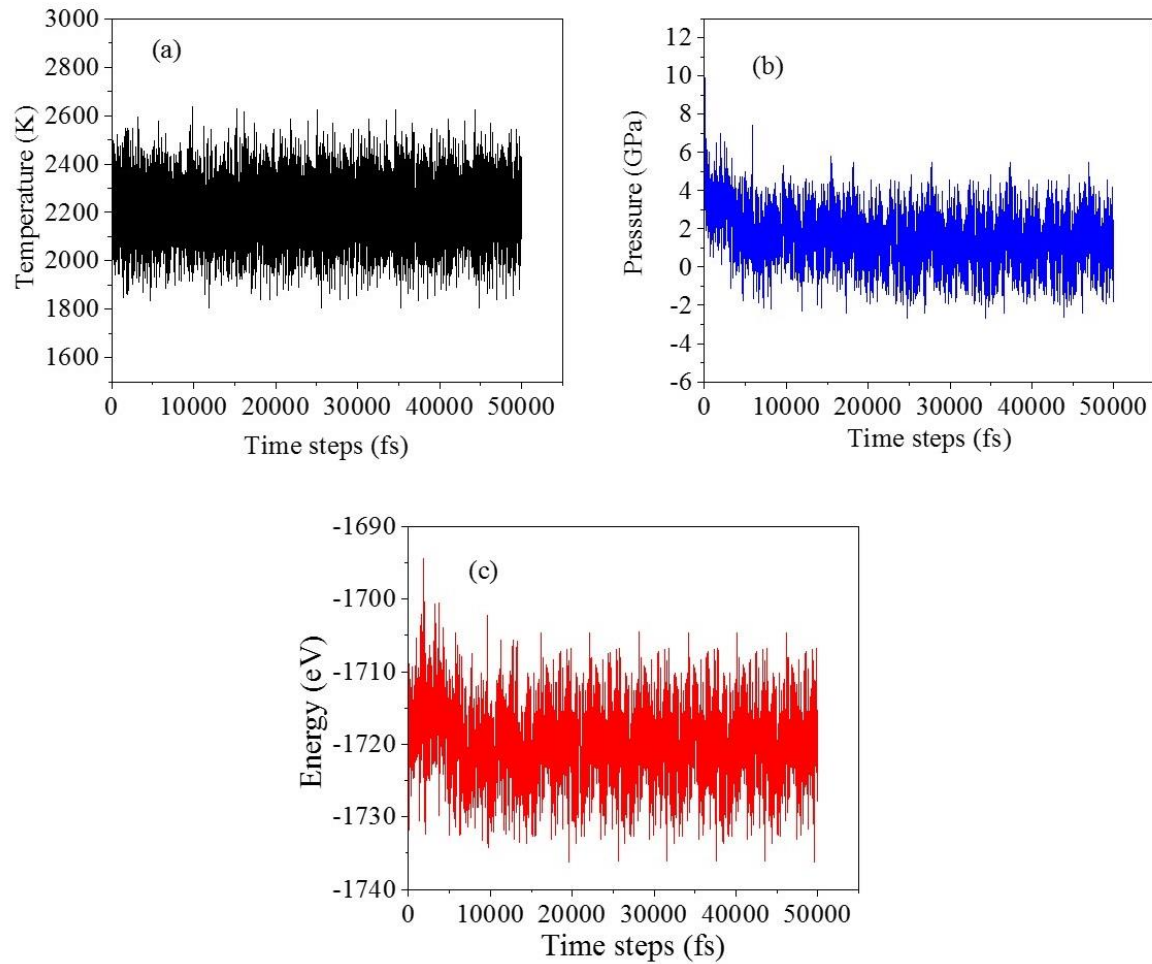
Figure 5.15 a) Temperature vs time, b) Pressure vs time, and c) Total energy vs time to confirm the convergence of the calculations of molten basalt at 0 GPa and 2200 K in an NVT ensemble.

5.3.2.2 Structural Transformation

We will show that there are several structural transitions from study of the structures transformation of the basaltic melt. The similarities between high pressure silicon and oxygen coordination for glass and melt are striking and this will be discussed in a later section. From Fig. 5.16a, it is evident that the Si atoms are 4 fold coordinated with oxygen atoms at ambient pressure forming SiO_4 tetrahedrons. When compressed, the coordination number remains 4 until 18 GPa. Above 18 GPa, the coordination number increases at the cost of the four fold coordination. As

125

shown in Fig. 5.16c, there is a mixture of four, five and six fold coordination. This mixed coordination is observed until 38 GPa at which the four fold coordination is gradually replaced by six fold coordination. Above 38 GPa, the predominant number of nearest oxygen neighbours of silicon is six. This indicates the completion of the gradual structural transition of the melt from four to six fold coordination.
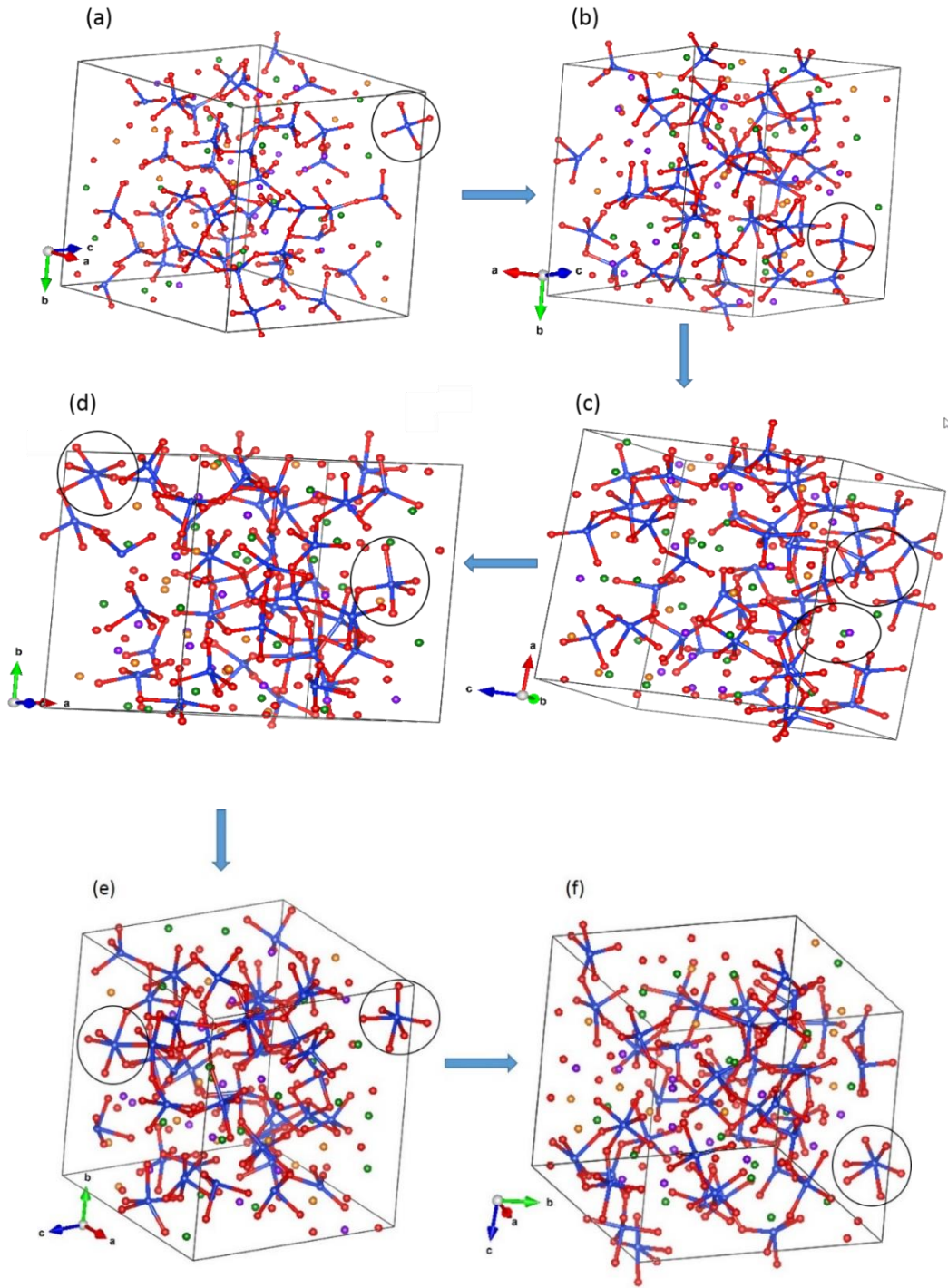
Figure 5.16 a-f) Snapshots of the structure of molten Basalt at 0, 18, 23, 38, 50 and 68 GPa respectively. The blue sphere are Si and the red spheres are O. The structural transition of the Si-O coordination has been shown with increasing pressure.

The structural change with respect to the aluminium and oxygen bonding is shown in Fig. 5.17. For aluminium, like other aluminosilicate melts [207, 219], the change of coordination from 4 to 5 again occurs within a very narrow pressure range. As can be seen in the sequential diagram below (Fig. 5.17a-f), that by 18 GPa, the four fold coordination drops sharply and Al atoms become mostly five-fold coordinated with oxygen atoms. This five-fold coordination, however doesn't change rapidly and gives rise to AlO_6 octahedrons within a small pressure window. Rather, even at 50 GPa, an equal mixture of five and six oxygen coordinated Al atoms are observed. Above 50 GPa, the number of nearest oxygen neighbours of aluminium gradually increases to six. At around ~70 GPa, traces of seven fold coordination can also detected, hinting that at greater pressures, transition to even higher coordination may occur.
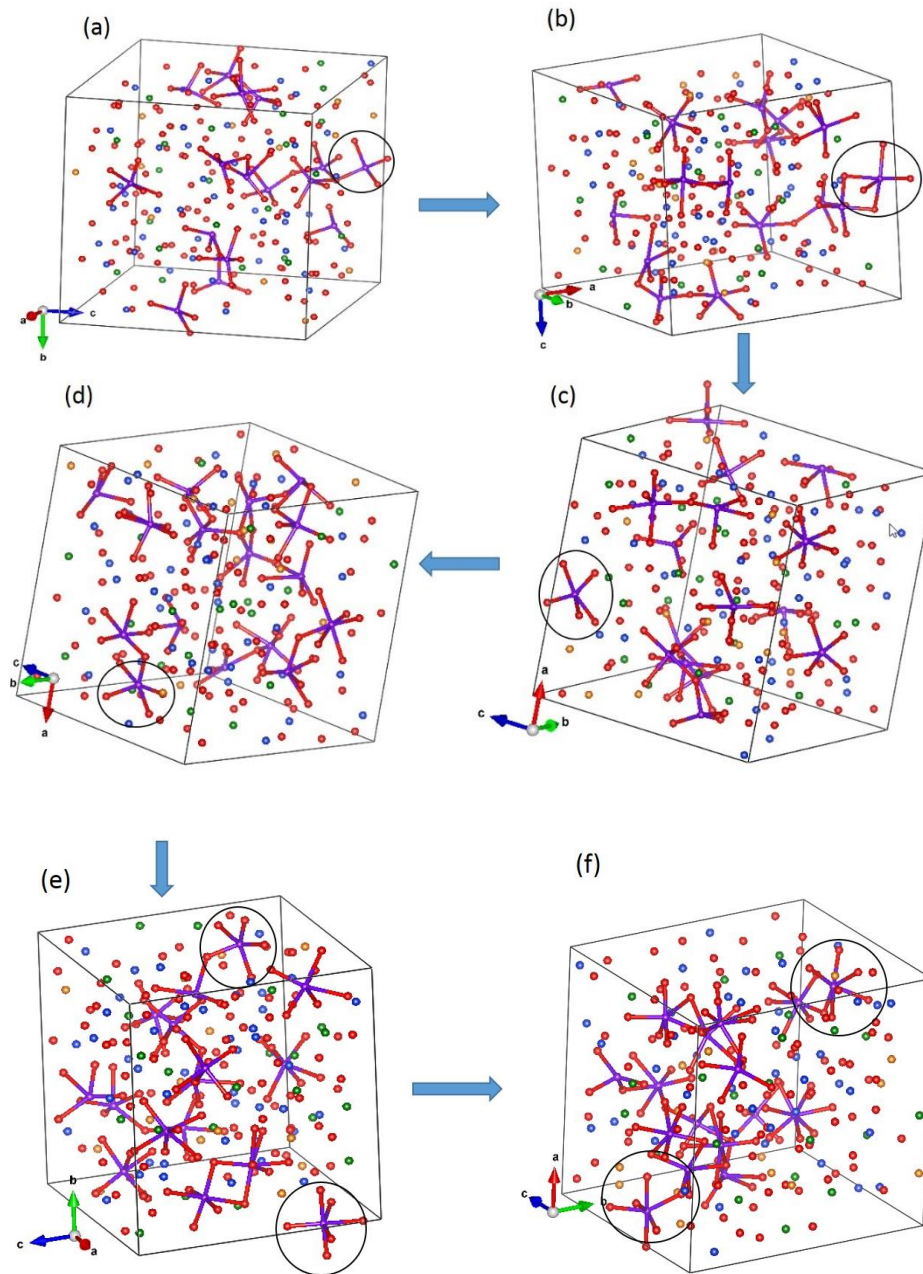
Figure 5.17 a-f) Snapshots of the structure of molten Basalt at 0, 18, 23, 38, 50, and 68 GPa respectively. The purple sphere are Al and the red spheres are O. The structural transition of the Al-O coordination has been shown with increasing pressure.

5.3.2.3 Radial Distribution

The RDFs of Si-O for molten basalt are plotted in Fig. 5.18a for all the pressure points at which simulations were performed. The nature of the RDF matched extremely well with those in literature as well as with our glass system. In this case the Si-O bond length is seen to shift to a lower value up to approximately 18 GPa and then starts to shift to higher values. The peak position gradually shifts to the left after 38 GPa. The Si-O bond length of the basalt melt at ambient pressure is 1.62 Å which decreases to 1.60 Å by 18 GPa and the four fold coordination of the Si atoms is still dominant. The same explanation as that for glass holds for this case as well. With compression, the bonds gets more squeezed. However, once the structural change commences, and higher coordination sets in, the bond length increases to accommodate more neighboring atoms, in this case oxygen. From 50 GPa onwards, when the transition from SiO_4 to SiO_6 is complete, the silicon-oxygen bond length is 1.65 Å. It further decreases gradually with increase in pressure. The first peak of the pair distribution function of Fig. 5.18a is the Si-O bond length. The nearest neighbour Si-O distances have been plotted in Fig. 5.18b and compared with the data from other studies [165, 168, 208 and 214]. The trend of the values that we obtained from MD simulations is in very good agreement with other silicate melts. In summary, the initial dip in the bond length till 20 GPa is due to compression, followed by an increase in the bond length (till 50 GPa) which signifies coordination change or structural transition, *i.e.* since the number of nearest neighbors (in this case oxygen) increases, the oxygen atoms spread out more at greater bond lengths to fit in more O atoms. At higher pressures there is another dip which is once again due to the reduction in the volume of the octahedron structure.
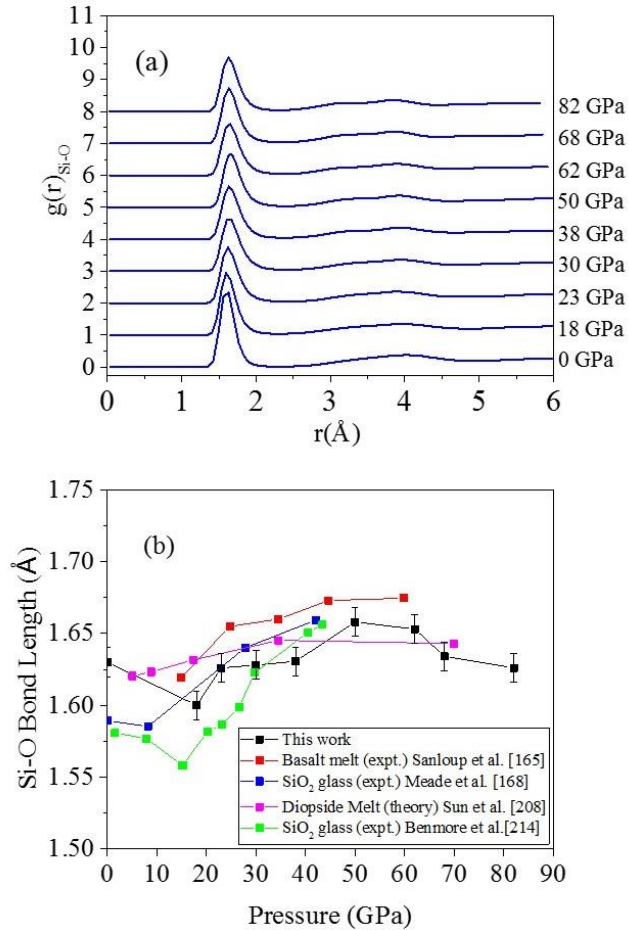
Figure 5.18 a) The RDF of Si-O at increasing pressure and b) Si-O bond length vs pressure for molten basalt.

Fig. 5.19a shows the RDF for Al-O. At 0 GPa, the Al-O bond length is 1.75 Å and at 18 GPa, the peak shifts to a higher value. From 0 to 18 GPa, there is a rapid drop in the four fold coordination but the five-fold coordination is maintained. To fit in more nearest neighbours, the Al-O bond length increases to approximately 1.77 Å. However once the transition to the octahedron (AlO₆) phase is almost complete, the bond length decreases to 1.75 Å once again due to decrease in volume. One would expect the bond length to decrease on further compression. However, we notice that even at 68 and 82 GPa, the bond length remains almost constant at 1.75 Å. This is probably due to the rise of seven fold coordination as has been shown in the next section. The

nature of the evolution of the Al-O bond length has been illustrated in Fig. 5.19b, which agrees very closely with another study on alumina melt by Verma *et al.* [213].
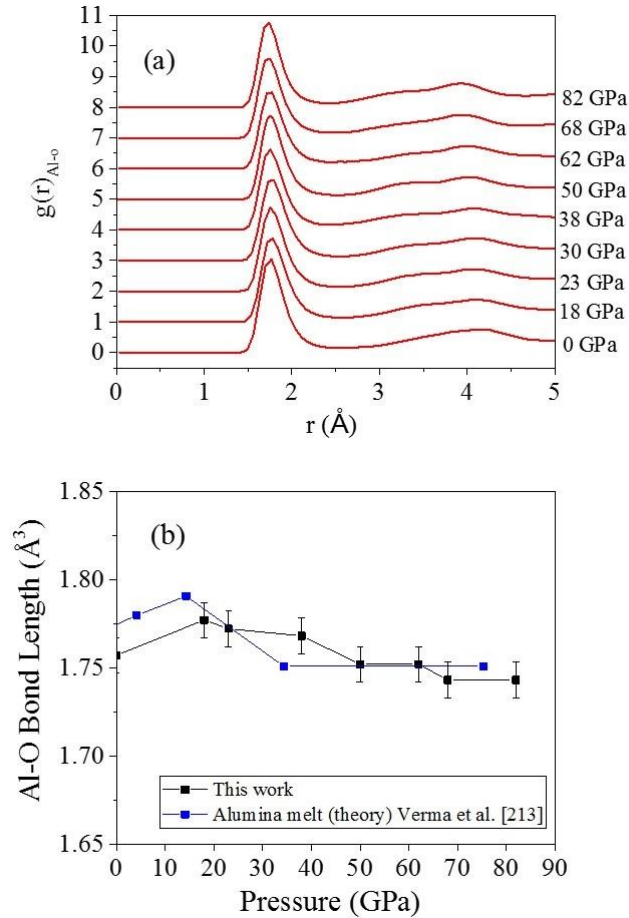

Figure 5.19 a) The RDF of Al-O at increasing pressure and b) Al-O bond length vs pressure of molten basalt.

From Fig. 5.20a and b, it is evident that unlike Al and Si, the bond length between calcium and oxygen keeps decreasing with pressure. The same trend was seen for the glass as well. Specifically, after 30 GPa, the bond length falls much faster. The average Ca-O bond length at ambient pressure is 2.29 Å and it remains almost constant up to 30 GPa. Above 23 GPa, Ca-O distance starts decreasing with pressure. For a better understanding, we compared our result with

that obtained by Sun *et al.* [208] as illustrated in Fig. 5.20b. From their MD calculations for molten diopside, the results matched extremely well with ours.
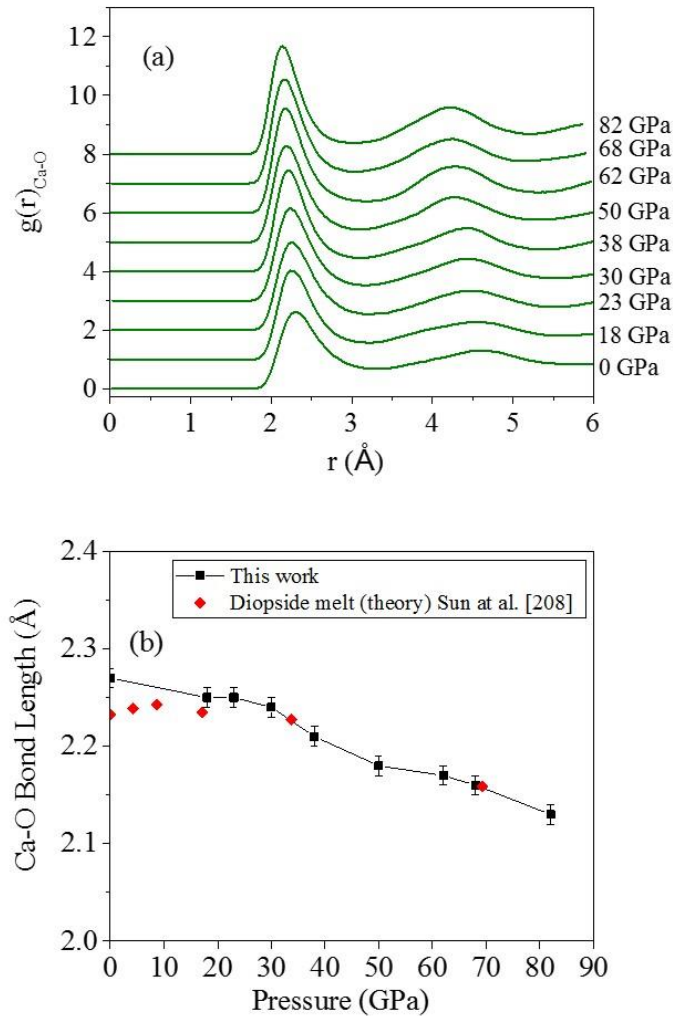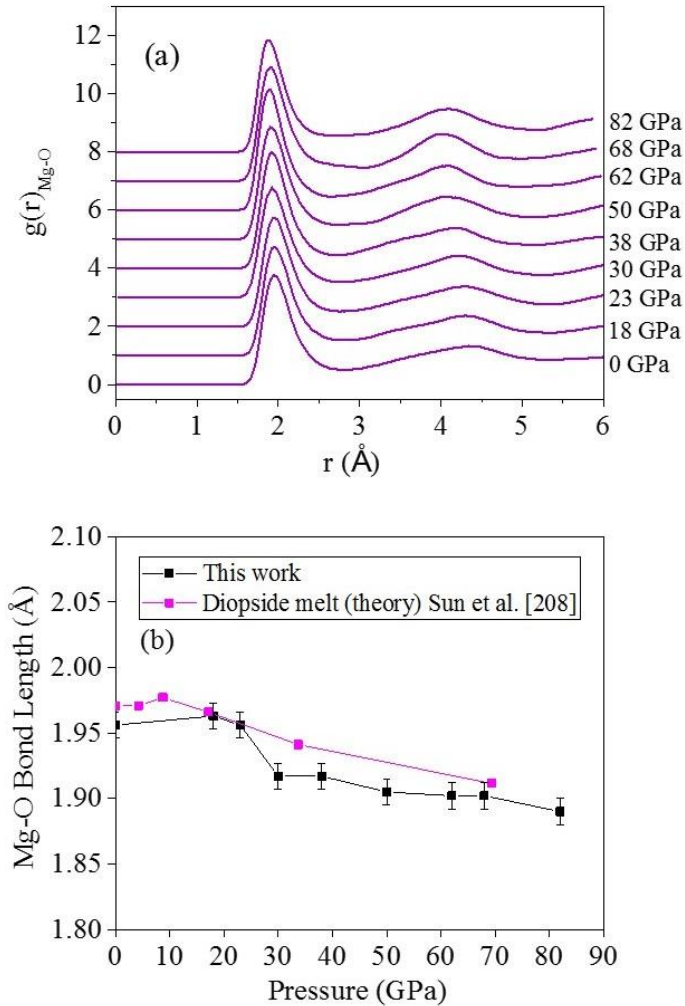

Figure 5.20 a) RDF of Ca-O with increasing pressure and b) Change in Ca-O bond length with increasing pressure basalt melt.

Similar to Ca, the bond lengths of magnesium and oxygen atoms in the glass structure are also almost constant till 23 GPa. Then it starts to decrease owing to the compression. After around 23 GPa, the Mg-O bond length falls steeply and attains a comparatively stable value of roughly

1.89 Å. This trend and the bond lengths match well with the Mg-O bond lengths found for diopside

melt by Sun *et al.* [208] and our results for the glass.

Figure 5.21 a) RDF of Mg-O with increasing pressure and b) Change in Mg-O bond length with increasing pressure of basalt melt.

5.3.2.4 Coordination Number

The melt structure is largely controlled by cation–anion bonding so the structural changes

due to pressure, temperature and composition can be better understood in terms of coordination

environments consisting of different cations and anions. As pressure rises, the calculated mean Si–O coordination increases relatively gradually initially from fourfold (at zero pressure) to six fold at high pressure in a remarkably similar way for the basaltic compositions studied in Ref. 165. The evolution of the coordination number of silicon atoms with respect to oxygen atoms has been shown in Fig. 5.22a. The basaltic melt like most other silicate melts has four fold coordination of silicon atoms at ambient pressure. With the onset of significant densification at 18 GPa, there is clearly a mixed four and five fold coordination. This was apparent in Fig. 5.16, where the structural change of the unit cell was shown at consistent pressure intervals. Although, we have no pressure points between 0 and 18 GPa, it is safe to assume that the four fold coordination dominates upto around 15 GPa. This can be justified from Fig. 5.22b in which we can see that for both experiments (NMR) and MD simulations, the average coordination remains very close to 4 for silica and silicate melts, within 0 and 15 GPa, indicating that the higher coordinations do not set in before 15 GPa. This has been found in the theoretical calculations as well which shows the individual percentage of the different coordination. The drop in the four fold coordination is sudden at approximately 18 GPa and then the coordination number increment keeps happening smoothly up until 38 GPa, after which it becomes a mix of five and six fold coordination which is somewhat similar to what we obtained for the glass structure. At higher pressures, that is after 50 GPa, the transformation from four fold (tetrahedron) to six fold (octahedron) coordination gets completed. For Silicon, this increase in coordination is possible as with increase in pressure and in turn energy, the d orbitals of the Si atoms also participate in bonding. The average coordination has been plotted in Fig. 5.22b. The increment of the value from 4 to 6 is once again marked by two distinct regions. From 0 to 23 GPa, the coordination increases rapidly while it slows down after 23 GPa.
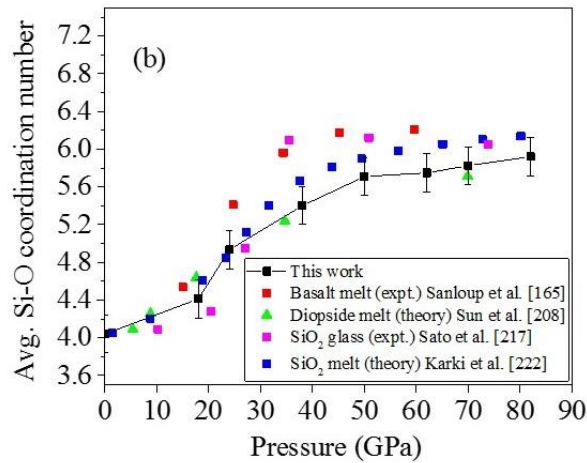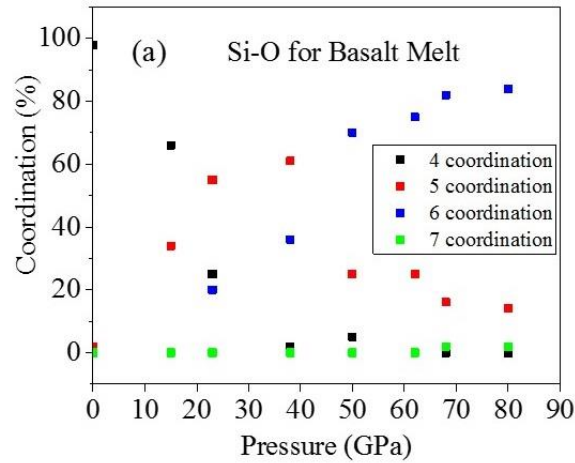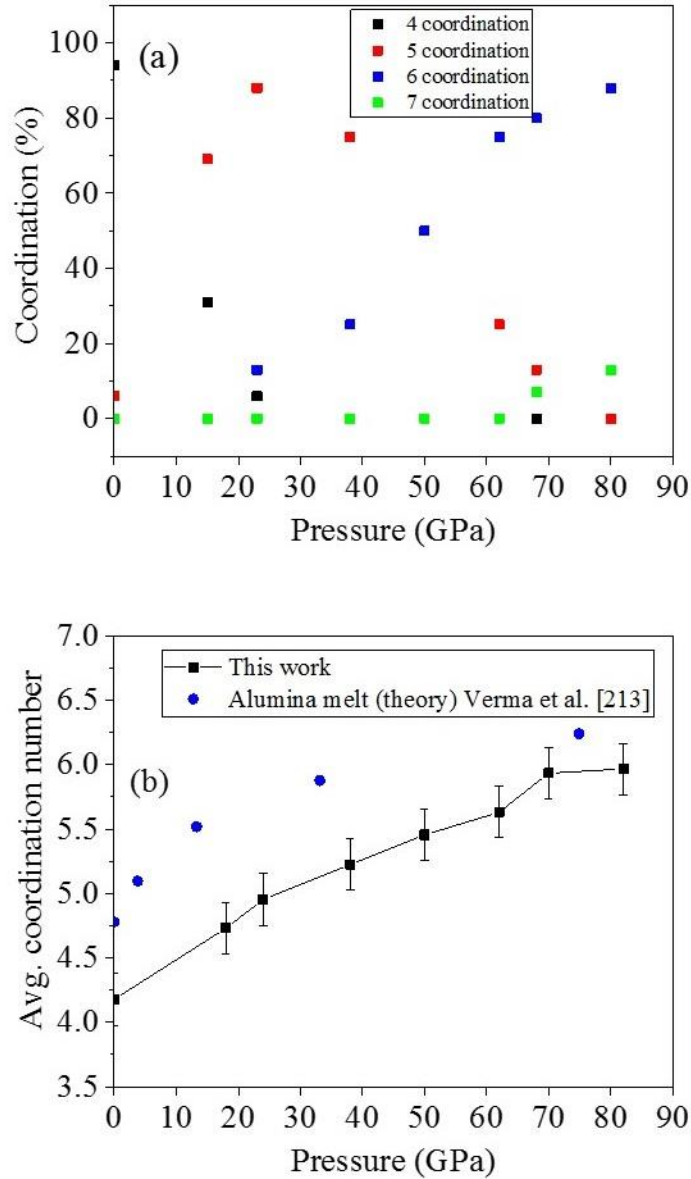
Figure 5.22 a) Coordination percentage vs pressure of Si atoms with respect to O atoms and b) Average Si-O coordination number vs pressure compared with other works.

The aluminium coordination number with respect to oxygen atoms is much sharper as is evident in Fig. 5.23a. By 20 GPa, the four fold coordination almost vanishes and gives rise to the intermediate five-fold coordination. Once again, this is in agreement with the literature for aluminosilicate liquids [218]. At 50 GPa, there is an almost equal concentration of five and six coordinated Al atoms. Eventually at very high pressures above 70 GPa, seven fold coordination

surfaces. The rapid increase in the density between 0 and 18 GPa can be attributed to the rapid increase in Al coordination.

Figure 5.23 a) Coordination percentage vs pressure of Al atoms with respect to O atoms and b) Average coordination number of Al atoms vs pressure.

5.3.2.5 Equation of State

The pressure-volume relation of basaltic melt is shown in Fig. 5.24. The points are fitted using the 4th order Birch Murnaghan (BM) equation of state (Eq. 5.1). All the points could not be fit using Eq. 5.1. Therefore two different fits (blue and red lines in Fig. 5.24) were used with the discontinuity being at approximately 30 GPa. The fit parameters are as follows. For the curve from 0 to 30 GPa, the ambient pressure volume (V_0) is 3120 Å^3, bulk modulus (K_0) is equal to 46 GPa and the pressure derivative of the bulk modulus is 3.2. From 30 GPa to 82 GPa, the pressure derivative of the bulk modulus is 5.2. Below and above 23 GPa, the compression mechanisms are different. For pressures below 23 GPa, the volume falls sharply and the decrement becomes slower at higher pressures. The structural change however is gradual and continuous.
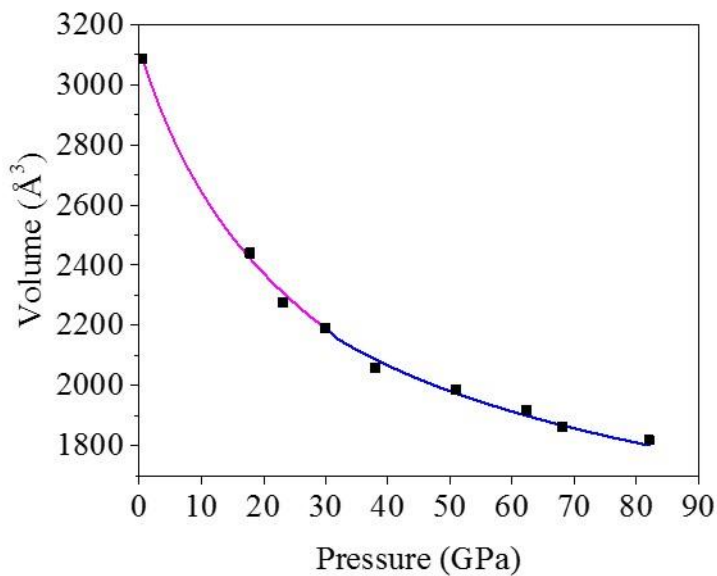

Figure 5.24 P-V curve of molten basalt fit with 4th order Birch- Murnaghan EOS fit. The two different curves are due to two different 4th order BM EOS fits.

The nature of the change of volume is reflected in the most of the other properties as well. This has been discussed next. From Fig. 5.25, the density of the molten basalt is seen to be

increasing which is not unexpected. Similar to the P-V curve, the increase in the density between 0 and 23 GPa is much more rapid than pressures above 23 GPa. In the investigated range of pressure points, no inversion of density was noted for the basalt melt either. From Fig. 5.25, it can be seen that the density obtained from our calculations is in excellent agreement with the density calculated in the simulations performed by Bajgain *et al.* for molten basalt [218].
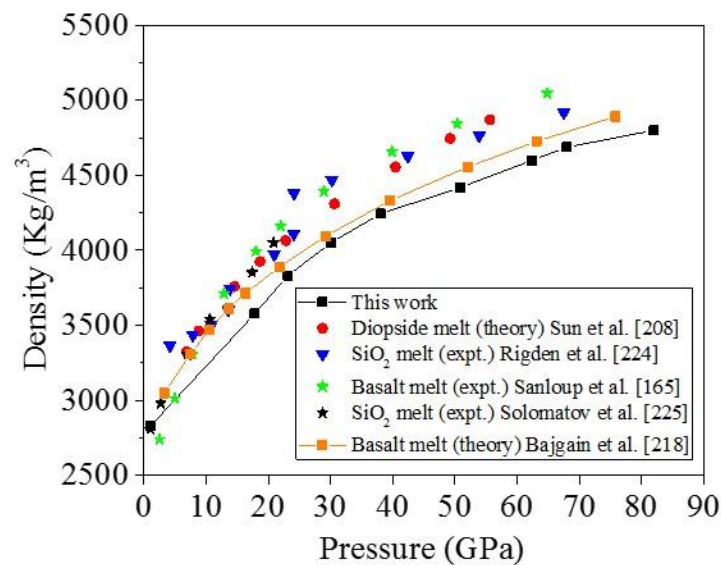

Figure 5.25 Change in density of the basaltic melt with pressure compared with other silicate melts.

Density of the relevant melt at high pressure and high temperature conditions, and finally the structures and coordination changes of such melts with pressure, influence the thermal, physical, and transport properties of melts with depth help to evaluate the density contrast between the solids and liquid that are present at great depth within the early Earth's mantle. Interestingly, a similar analysis has been postulated for silica from the observed glass behaviour [217]. Over the 0–60 GPa range, silica melt first transforms to a densified melt (equivalent of the quartz to coesite transition but smoothed over a larger pressure range), then Si–O coordination number increases from 4 to 6, after which silica melt has a stishovite-like behaviour.

139

From the 4th order BM fit, the first order numerical derivative of the pressure with respect to the volume can be obtained. Using the following formula (Eq. 5.3), the bulk modulus was obtained. Same as the glass structure, the pressure range where the pressure volume curve is steep, and the bulk modulus has a smaller value. This is expected as at lower pressure the material can be compressed more, the isotropic compressibility is more as the bulk modulus is simply the inverse of compressibility. At 23 GPa, there is a slight discontinuity due to the two different BM fits used for the low and high pressure regions.
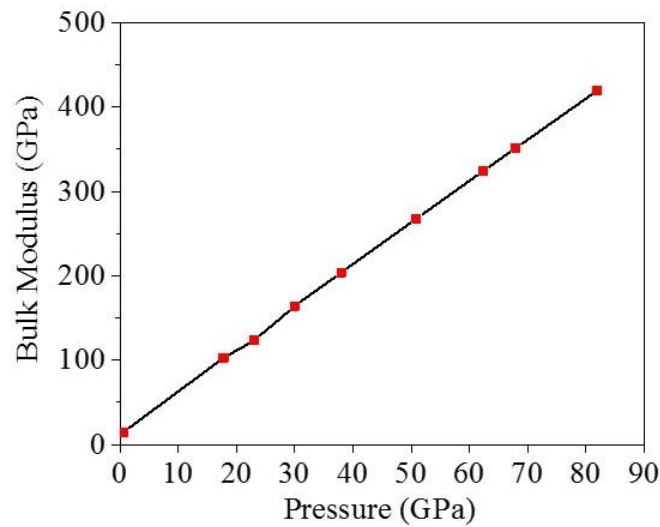
Figure 5.26 Bulk modulus of the melt as a function of pressure.

The velocity of sound at bulk is calculated from Eq. 5.4. As evident from Fig. 5.27, above 23 GPa, there is an increase in the velocity. This increase can be explained mathematically. At high pressures, *i.e.* above 23 GPa, both the bulk modulus and density increase. But the density as seen from Fig. 5.27 flattens down compare to that in the lower pressure region. Thus the bulk modulus increases more rapidly than the density which leads to high velocity of sound. Compared to other studies as illustrated in the plot of Fig. 5.27 and the system in the glass state as discusses in the

140

previous sections, the increase of the velocity is much steeper between 0 and 23 GPa and becomes more slow at higher pressures.
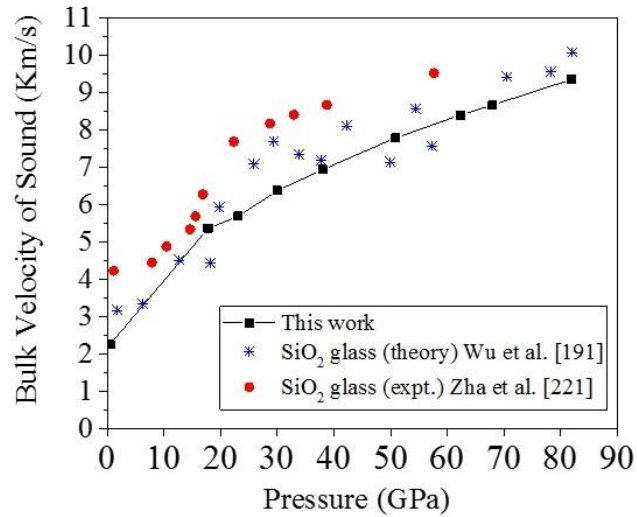

Figure 5.27 Pressure evolution of the velocity of sound in molten basalt.

5.3.2.6 Electronic Properties

The electronic density of states (DOS) was determined for the molten basalt at all the pressure points. Throughout the compression process, no transition to the metallic state was observed. Fig. 5.12 a-d shows the DOS at various pressure points. In fact, on the contrary, the band gap increases gradually from 1.52 eV at 0 GPa to 3.60 eV at 68 GPa.
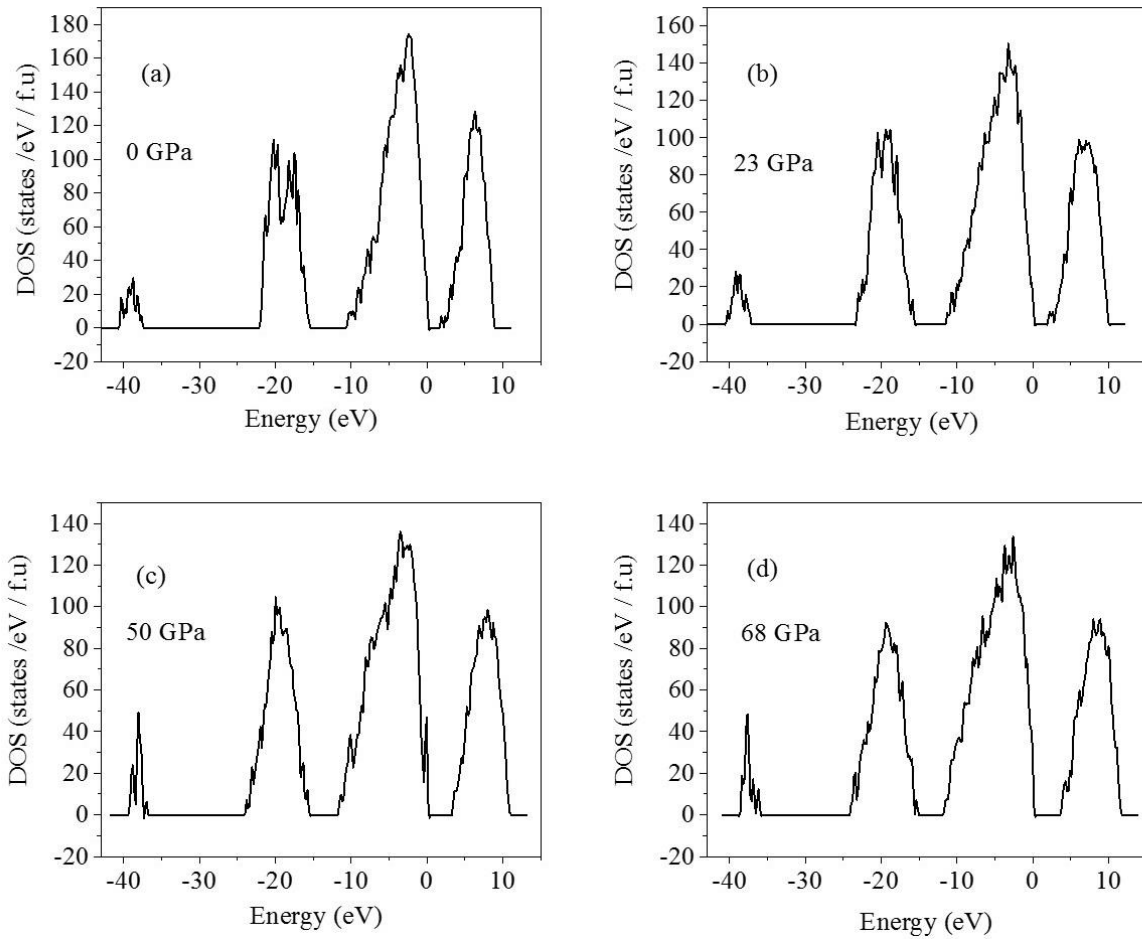
Figure 5.28 a-d) Electronic DOS of basalt melt at 0, 23, 50 and 68 GPa, calculated using PBE XC functional.

5.3.3 Diffusion and Viscosity of the Melt

The study of molten silicates is crucial to understand the cooling and crystallization of the Earth's early magma ocean as well as the present day mantle dynamics [224-225]. Diffusivity is unique compared to other transport properties such as viscosity with regards to the fact that diffusion coefficient can refer to a specific component or species rather than to the bulk melt. In order to understand the geological implications of the basaltic melt at the upper mantle condition, it is necessary to study this transport property, *i.e.* diffusion. In this section, the diffusion and

viscosity of the molten basalt at 2200 K as a function of pressure has been discussed. From Fig. 5.29, it is apparent that the MSD of the Mg atoms has the highest slope in the linear region, denoting that the magnesium atoms diffuse the most at 0 GPa and 2200 K. Consistent with literature [226], silicon has comparatively the least steep MSD, thereby diffusing the least. The predicted diffusivity sequence is Mg > Ca > Al > O > Si. Our results at 0 GPa and 2200 K show that Mg is the fastest species, whereas Si is the slowest species with $D_{Mg}/D_{Si} = 1.83$. The predicted ordering of $D_{Mg} > D_{Ca} > D_{Al} \approx D_O > D_{Si}$ somewhat agrees with the measured order for the melt with composition 20CaO-20Al$_2$O$_3$-60SiO$_2$(wt %) at 1 GPa and 1773 K [210]. As temperature decreases, the mechanisms become increasingly sensitive to local structural environments and different species see different local potentials. Mg and Ca atoms, being relatively weakly bonded to O atoms compared to bonding between Si (or Al) and O atoms, can move easily in open space available at large volumes. Consistently, in MgSiO$_3$ liquid, Mg was also predicted to be the fastest species [227]. Since, the Ca-O and Mg-O bonds are much weaker than the Al-O and Si-O bonds, they get broken at much higher rates. Generally diffusion is inhibited on compression. If one considers atoms and ions as hard spheres, pressure suppresses the proportion of "free volume" in the structure (referred to as the ionic porosity) [228-229] and makes diffusion more difficult. For depolymerized melts, the negative pressure effect is also associated with the polymerization of melt structure, by converting non-bridging oxygen (NBO, oxygen atom bonded with a single network-forming cation) to bridging oxygen (oxygen atom shared by two neighboring network-forming units) [182]. The calculated self-diffusivities depend on temperature along with pressure. Quite intuitively, they show the normal trend that the diffusivity decreases monotonically with pressure. As temperature is decreased, the pressure dependence becomes stronger and vice versa. This can be attributed to bond breaking with increasing temperature, facilitating higher diffusion.
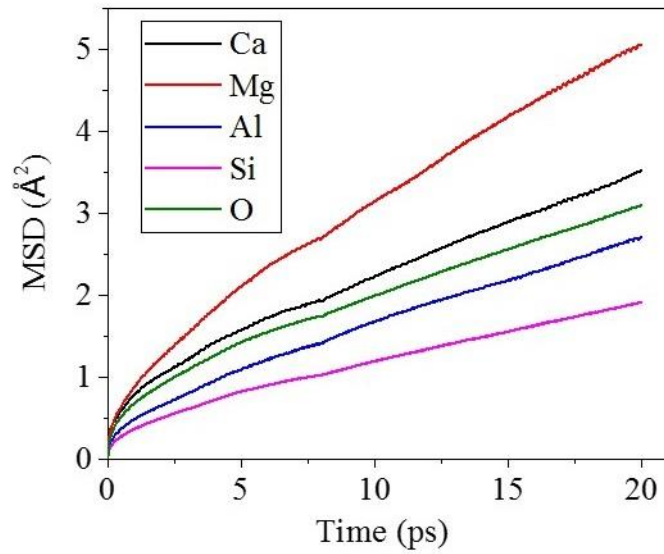
Figure 5.29 Mean Squared Displacement of the different elements in the Basaltic melt at 0 GPa.

Once the individual diffusion coefficients are determined for all the species, the average is taken to get a rough estimate of the overall diffusion coefficient of the bulk melt. Fig. 5.30 shows the mean squared displacement of the bulk melt at 0 GPa. Till close to 1 ps, the ballistic regime dominates and the diffusion is proportional to t^2 and is non-linear as collision is almost negligible in this regime of the MD study. Once, the curve becomes linear, the slope is calculated and using Eq. (1.64), the diffusion coefficient (D) is calculated.
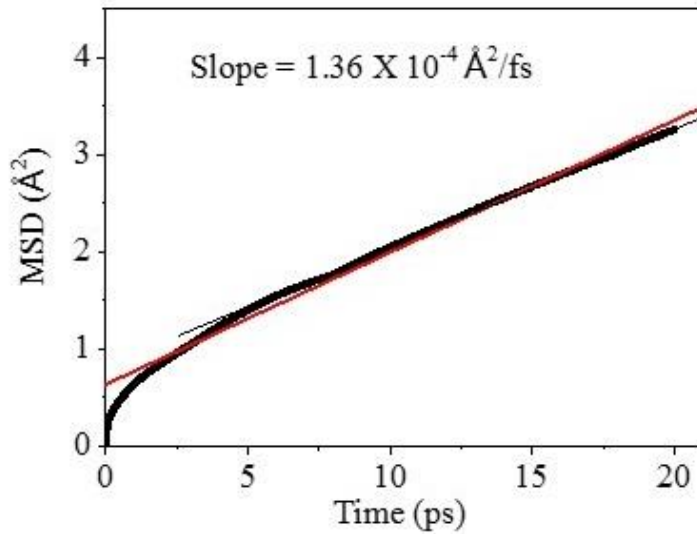
Figure 5.30 Net Mean Squared Displacement of the Basaltic melt at 0 GPa. The red line is the best linear fit and the slope is calculated to compute the diffusion coefficient further.

The dependence of D on pressure is shown in Fig. 5.31 and 5.32. The drop at approximately 23 GPa insinuates a structural transition, *i.e.* change in coordination number. This pressure point matches well with the transition point shown in the EOS in the previous section. At this pressure, both the Si and Al atoms start losing the four fold coordination and start becoming octahedrally coordinated. At 62 GPa, there is another significant drop in the order of magnitude, possibly originating from the further increment of coordination where it starts to show traces of 7 fold coordination for both Al and Si. From Fig. 5.31, it can be noted that for all the species, the diffusion coefficient decreases at 18 GPa. As for Al, Ca and Mg, at 50 GPa, the diffusion coefficient rises again before it starts decreasing. However, for Si and O, the diffusion coefficient rises at 62 GPa and then starts to plummet when compressed.
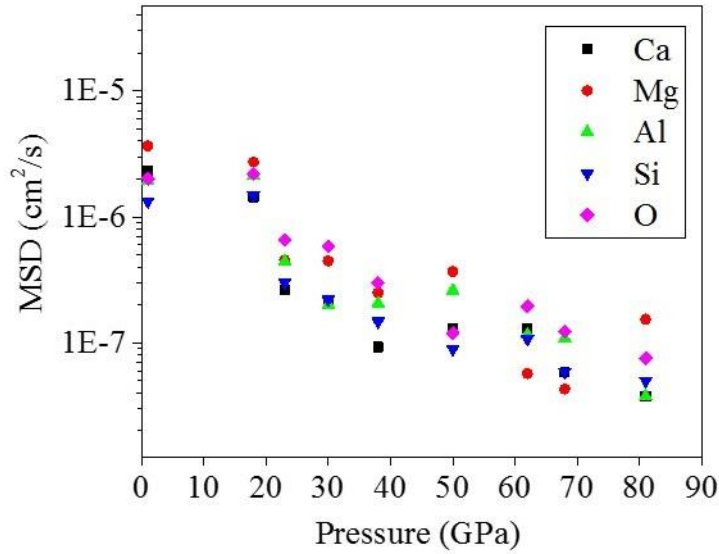
Figure 5.31 Diffusion coefficient of the individual species as a function of pressure at 2200 K.
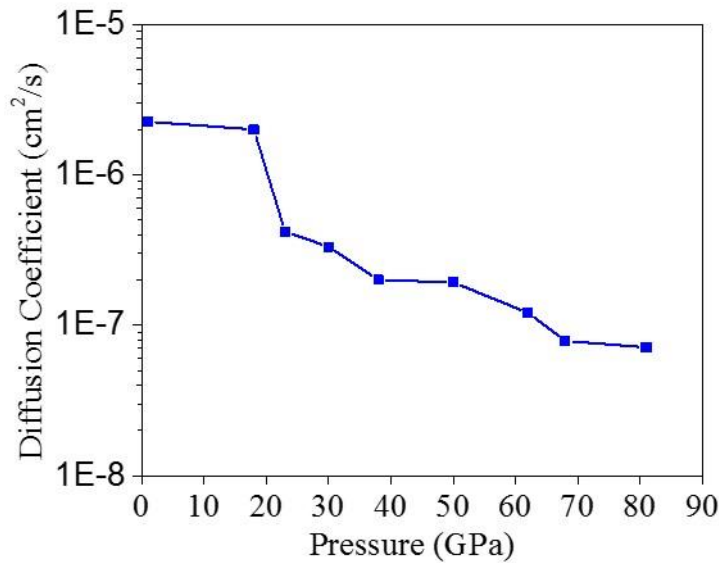

Figure 5.32 Diffusion coefficient vs pressure of basalt melt at 2200 K.

In order to compute the coefficient of viscosity using Eq. (1.63), the diagonal (xx,yy and zz) and off-diagonal (xy, yz and zx) stress tensors should oscillate around the desired pressure and zero pressure respectively. This ensures that the pressure applied is isotropic. Therefore, all the

146

stress tensors of molten basalt were checked to confirm that in our MD calculations the pressure was always isotropic. Fig. 5.33 shows the diagonal and off-diagonal stress tensors for molten basalt at 30 GPa.
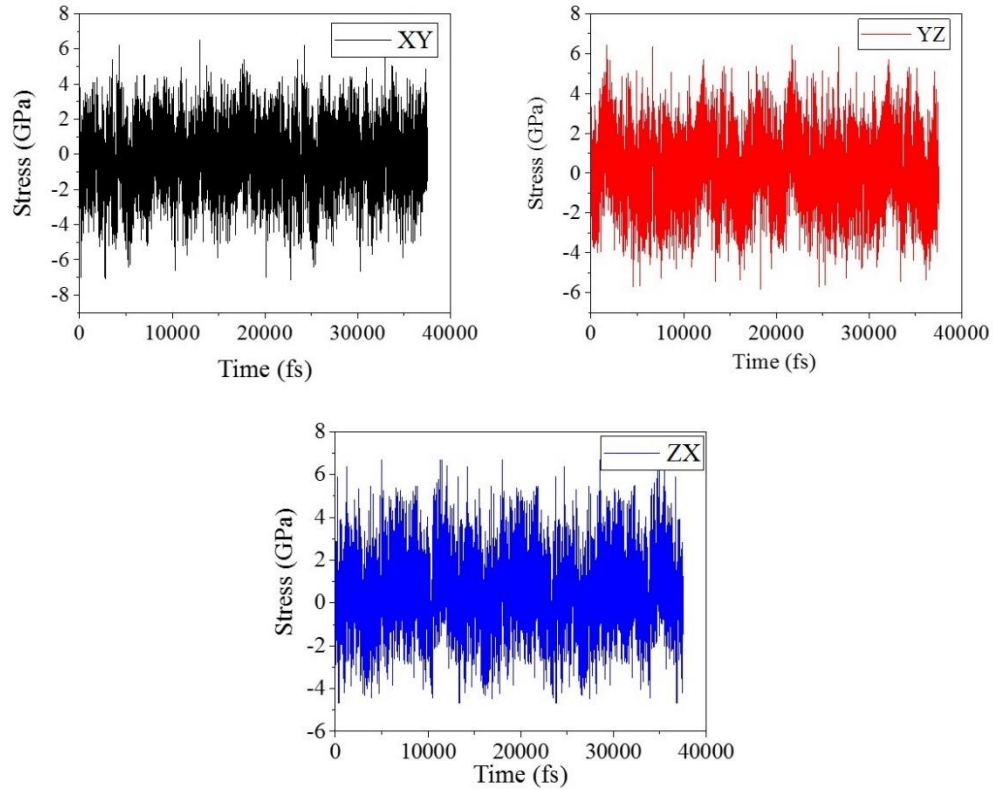

(a)
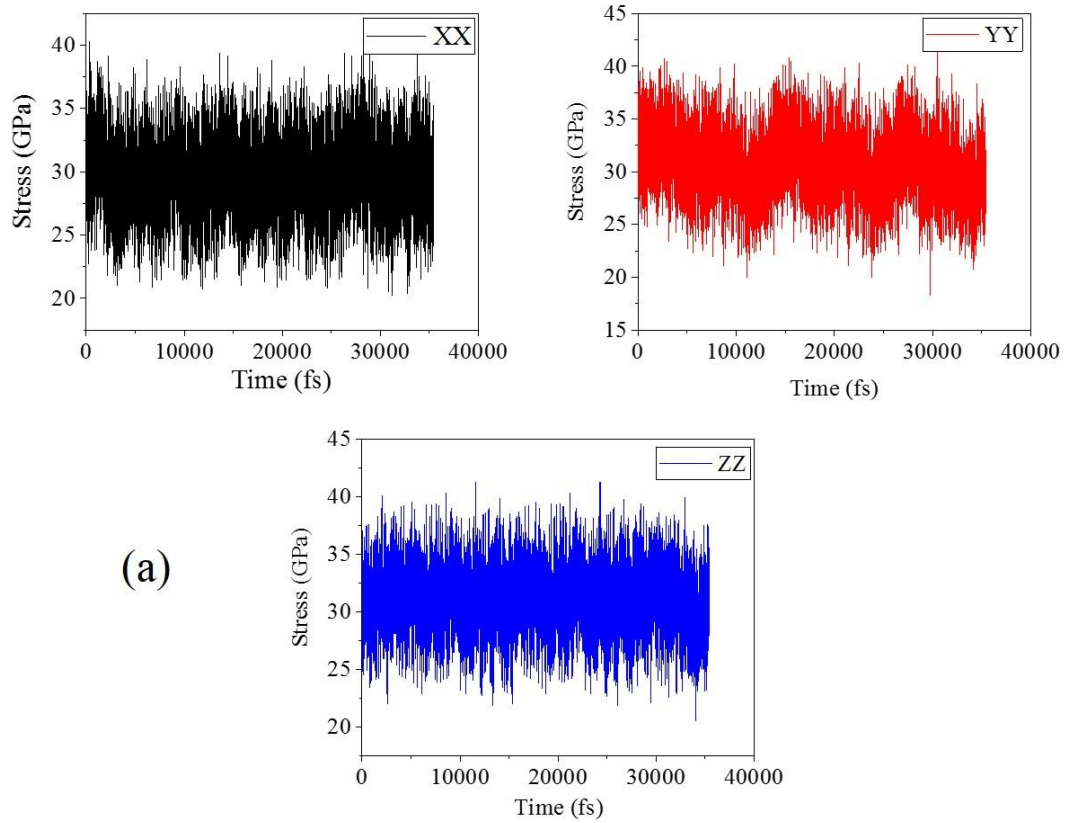
Figure 5.33 Stress tensors of molten basalt at 30 GPa of the a) diagonal and b) off-diagonal components.

Once the isotropy of the stress tensors is established, the stress autocorrelation function (SACF) is calculated and from Eq. (1.63) the coefficient of viscosity is computed. In Fig. 5.34, the average of all the SACF (off-diagonal and difference of diagonal) is shown for 0 GPa. After approximately 8 ps, the SACF decays to and oscillates about zero. Taking the area under the curve and choosing 8 ps as the cutoff, and using Eq. (1.63), the coefficient of viscosity (η) is found to have an average value of 48 mPa.s. In the same way, the η for the other pressure points is also calculated. Due to the oscillatory profile of the SACF around zero, we calculated the η with different cutoff values and included the deviations from the average value in the error bars. The deviation is generally seen to be approximately within 10-15% of the average value.
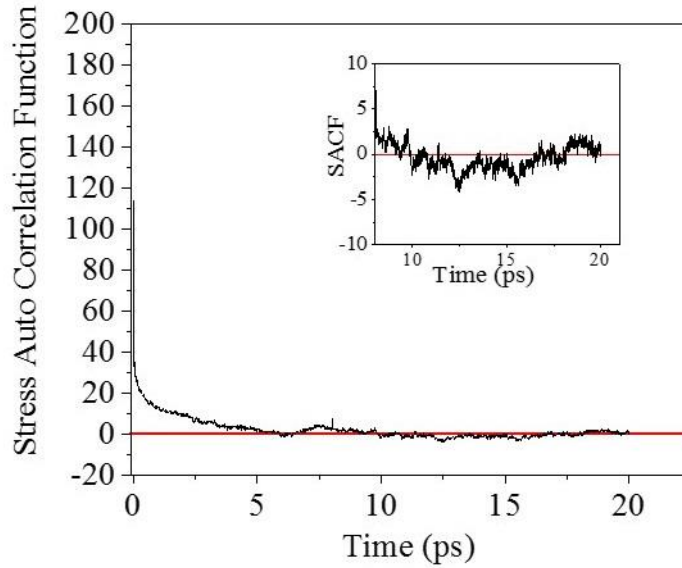
Figure 5.34 Stress auto correlation function vs time for molten basalt at 0 GPa. In the inset, the oscillation around 0 is shown.

The coefficient of viscosity at different pressures were calculated using different time origins and cutoff times, to confirm the convergence within the error bar. Usually, if the curves do not become roughly flat (converge) and show undulations, the simulations are run for longer periods of time to allow the SACF to decay to zero. In Fig. 5.35, the η is seen to converge approximately after 8 ps for the different pressures (0, 38 and 62 GPa). It is the converged values that have been reported.
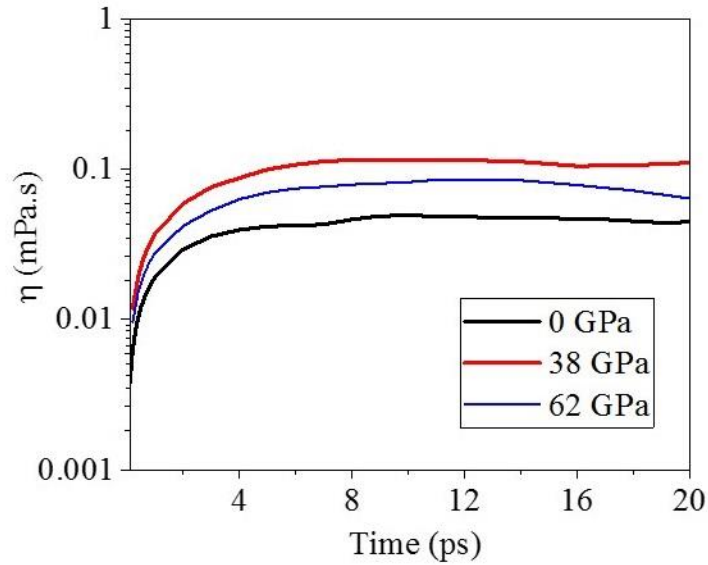
Figure 5.35 Convergence of the coefficient of viscosity with respect to time at selected pressure points.

Molten aluminosilicates are responsible for many of the igneous processes in the mantle. The density contrast of the molten aluminosilicate with the surrounding mantle determines the buoyancy of the melt which is a deciding factor in whether the basaltic magma will rise or sink. Similarly, the viscosity of the melt can influence several factors too, *e.g.* mineral fractionation and crystallization, thermal transport, *etc*. The shear viscosity of the melt is dependent on several factors that include the effect of composition, pressure, and temperature. In our study, the effect of pressure has been studied on the viscosity at 2200 K. The coefficients of viscosity for the molten basalt is shown in Fig. 5.36. At 0 GPa, the coefficient of viscosity is 49 mPa.s. It rises to 105 mPa.s by 50 GPa and then drops to 80 mPa.s by 80 GPa.
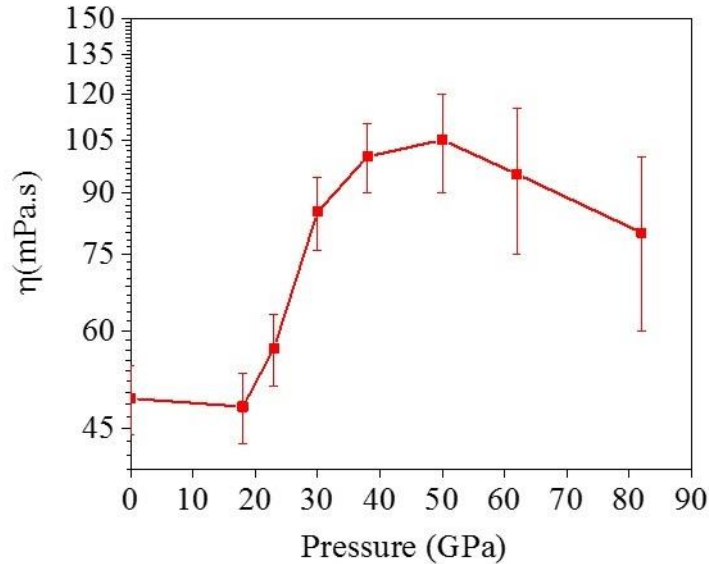
150

Figure 5.36 Coefficient of viscosity vs pressure of molten basalt at 2200 K.

Similar to other aluminosilicate melts that have been studied, even in our study we see a slight drop in the coefficient of viscosity till 18 GPa, which in literature is referred to as the anomalous behaviour of viscosity on compression [230]. Above 18 GPa, the viscosity rises steadily up to 50 GPa. Above 50 GPa, within a considerably large error bar, the coefficient of viscosity decreases contrary to other studies on silicate melts [231]. Between 0 and 18 GPa, the coordination of both Si and Al increase above 4. Specifically for aluminium, within a very narrow range (as described earlier), the coordination predominantly becomes five. This is contrary with the structure of silicate crystals in which fivefold coordination occurs rarely. Thus silicate or aluminosilicate liquid structures cannot be considered to be a somewhat disordered version of crystalline structure. The predominance of fivefold coordination at intermediate compressed region has the following consequences. Firstly, it contributes to the gradual change in the mean Si–O and Al-O coordination number and the density with increasing pressure. Secondly, fivefold coordination has been proposed by Angell *et al.* as a key ingredient for facilitating diffusion and viscous flow [192]. Even

151

experimentally, diopside melt shows an initial decrease in viscosity with increasing pressure, consistent with the growth of fivefold coordination [232]. Ideally, a polymerized network aluminosilicate liquid should have four coordinated aluminium and silicon atoms, and 2 coordinated oxygen atoms. In such a melt system, all the oxygen atoms act as bridging oxygen (BO) atoms. Such systems have very high viscosity owing to the high activation barrier. On increasing the pressure, the coordination of the aluminium atoms increases to five very rapidly, weakening the Al-O bond, thus increasing the mobility of the atoms. However, Yarger *et al.* [233] suggested that the bond angle changes of tetrahedral aluminosilicate network can also be a factor responsible for the decrease of the viscosity with compression. Although pure silica melts have been observed to have high viscosity, the addition of alkali and alkali earth elements act as network modifiers which reduce the viscosity drastically [233]. The inclusion of alkali and alkali earth elements (Na, Ca, Mg, *etc.*) breaks the Si-O and Al-O linkages, giving rise to non-bridging oxygen (NBO) atoms. Previous studies have shown that the viscous flow in aluminosilicate melts is dependent on the oxygen exchange between polymeric units [234-235]. Presence of the non-bridging oxygen atoms destroys the tetrahedral network structure resulting in the lowering of the activation energy for oxygen exchange. The low activation energy facilitates higher mobility, *i.e.* lower viscosity. In this study, between 0 and 18 GPa, the decrease in the viscosity can be attributed to the rapid increase in the aluminium coordination with oxygen. Interestingly, in our study, we found that the viscosity once again drops after 50 GPa. We have already seen that above 50 GPa, aluminium starts showing seven fold coordination, thus weakening the Al-O bond further. Furthermore, on compression, the alkaline and alkaline earth metals in our system, *i.e.* Ca and Mg, also attain higher coordination, thus giving rise to more NBO and lowering the viscosity further.

Fig. 5.37 shows the transition in the polyhedral structures for Si and Al. It is apparent that five-fold coordination and eventually even seven-fold coordination of the Si and Al atoms is the reason behind the anomalous viscosity.
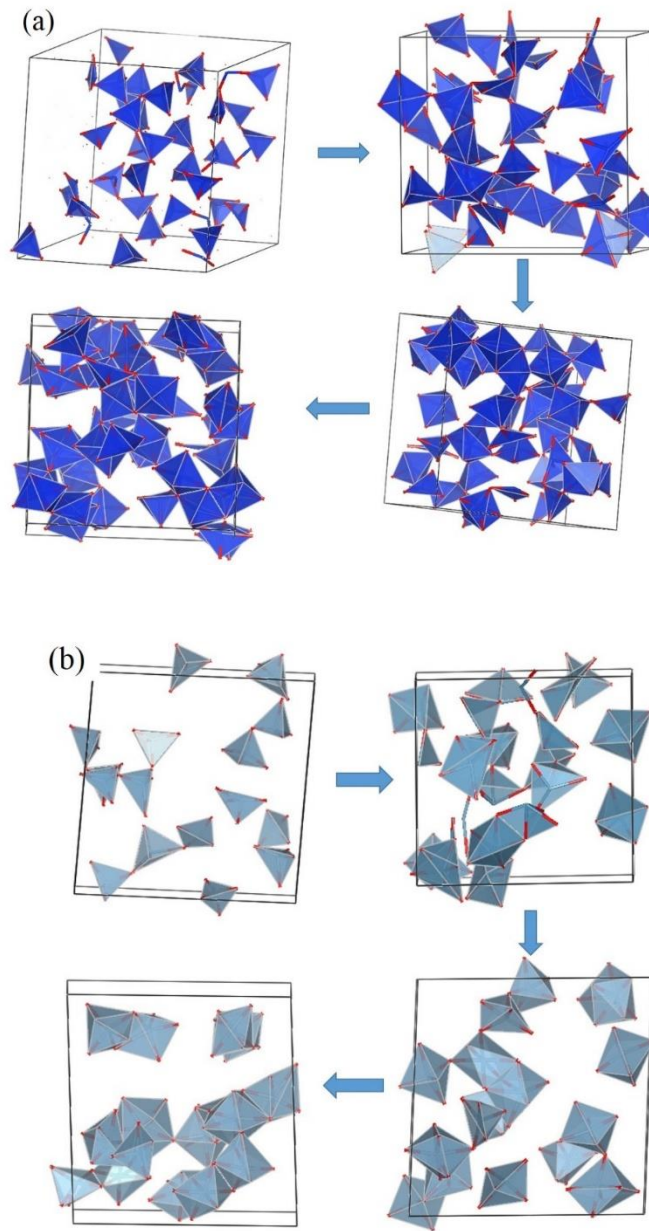

Figure 5.37 a) Polyhedra of Si-O linkages showing the transition from 0 GPa to 79 GPa via 30 GPa and 50 GPa and b) Polyhedra of Al-O linkages showing the transition from 0 GPa to 79 GPa via 30 GPa and 50 GPa.

5.4 Comparison of the Glass and Molten Basalt and Geological Implication

Considering the similarity in the structural changes in compressed silicate glasses and melts at conditions similar to that of the Earth's lower mantle [236], we studied both basalt glass and melt. This is to confirm if the glass structure can be used to determine melt properties as it is difficult to experimentally compress and study the various properties of melt. From Fig. 5.38, it can be seen that all the intrinsic properties, *i.e.* density, bulk modulus and bulk acoustic velocity are almost overlapping. Therefore, the model basalt glass is a good representative of its molten counterpart. Our results show that the melt is more compressible than the glass. At lower pressures, the glass is around 5% denser than the melt. But, the density contrast keeps decreasing with increasing pressure (Fig. 5.38b). At pressures close to 80 GPa, the densities of the glass and melt are very similar. In several studies concerning silicate and alumina melts [213, 222], density crossover has been predicted at pressures of around 90 GPa. At this pressure, the liquid becomes denser than the solid, a feature that is relevant in the dynamics of the magma in the Earth's interior. In this study, the small density contrast insinuates at density crossovers in the mantle. Thus the negative buoyancy of the melt makes it plausible to be trapped in the lower mantle, which eventually effects the dynamics of the melt accumulation and circulation in the deeper parts of the mantle. This can perhaps even explain the seismic discontinuities. Due to the density crossover between liquid and solid phases, the mantle is fractionated. Similarly, the possibility of density crossover between basaltic magma and olivine was first suggested by Stolper et al. [237]
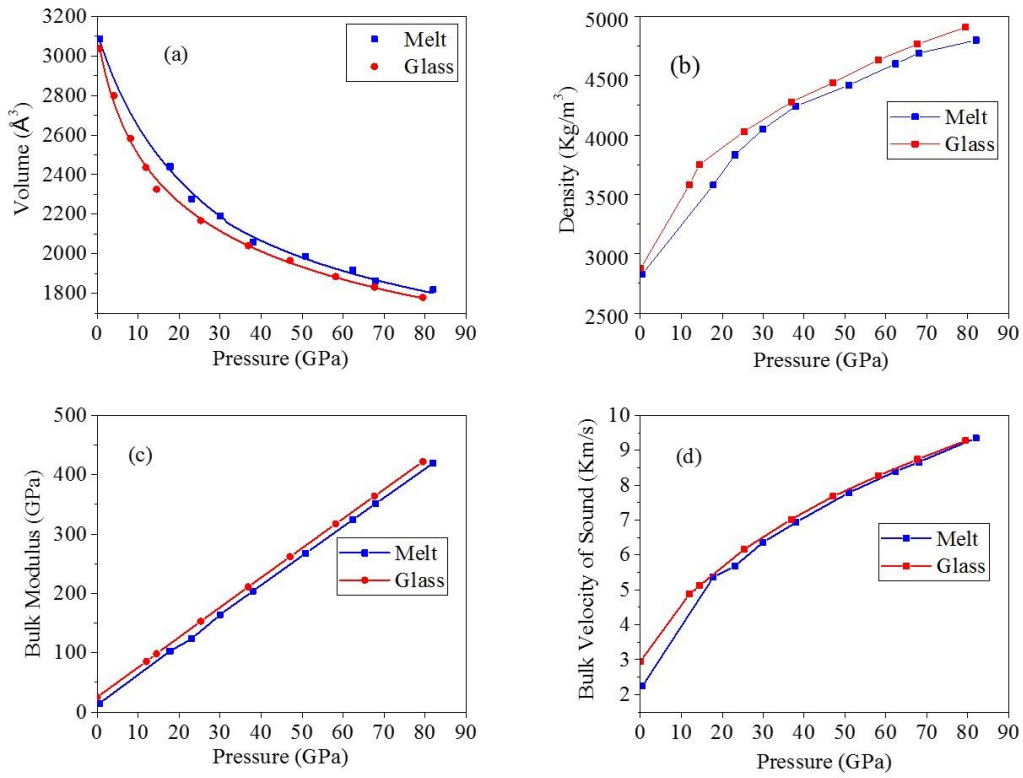
Figure 5.38 Comparison of glass and molten basalt at 2200 K. a) volume vs pressure, b) density vs pressure, c) bulk modulus vs pressure and d) bulk velocity of sound vs pressure.

The probable density crossover can also be inferred from the cation-anion bond lengths in the glass and melt. In Fig. 5.39, it can be clearly seen that the bond lengths are greater for the melt at lower pressures. This is due to the greater volume of the melt. However, at higher pressures, the bond lengths almost coincide, confirming that the volume and density of both the glass and melt become almost equal, thus the densities becoming almost equal.
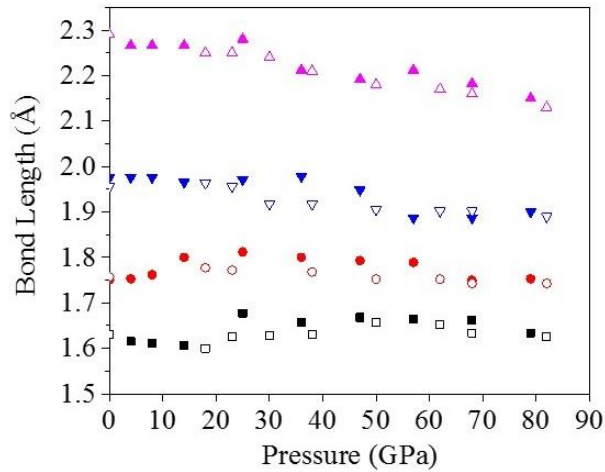
Figure 5.39 Comparison of bond lengths as a function of pressure of glass and molten basalt at 2200 K. Open and closed shapes denote glass and melt respectively.

Although the glass and melt show similar density profiles, the glass structure has a different trend of aluminium coordination number change compared to that of the melt. This is perhaps because, the glass structure even at ambient conditions has a significant amount of five-fold coordinated aluminium. Since, the pentahedral Al-O structure has weak bonding, on slight compression, the bonds break and form octahedral structures. From Fig. 5.40, the trend of the silicon coordination for both the melt and glass is similar, although the glass structure shows slightly more rapid transition to five-fold coordination.
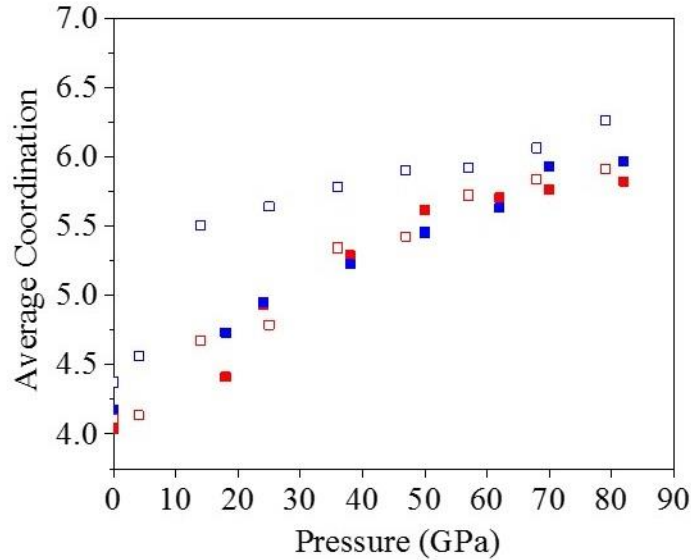
Figure 5.40 Comparison of the average coordination of silicon and aluminium with oxygen. The red squares represent Si while the blue squares represent Al. Open and closed shapes denote glass and melt respectively.

One of the very few pioneering works which explores the structural changes of molten basalt at the deep mantle conditions is by Sanloup *et al.* [165]. In the previous sections, we have compared our results with the density, Si-O distance and Si-O coordination number obtained in the study by Sanloup *et al.* [165]. Our calculations slightly underestimate the density, Si-O bond length and Si-O coordination compared to the experimental results (Figs. 5.18, 5.22 and 5.25). This is probably due to the difference in composition, *i.e.* in our model basalt system, we have not considered other components such as Fe-O, Na_2O, K_2O, *etc.* But, since the trends are same, it allows us to draw certain geological inferences that have been discussed in Ref. [165]. Owing to the already discussed density crossover, a layered magma ocean can be expected to exist at the lower mantle. This magma ocean is separated from another upper magma ocean by a solid crystalline layer.

157

As pressure decreases, the melt density decreases too and the magma is pushed upwards. But, the other factor that determines the motion of the magma is the viscosity. Thus a more reliable parameter to understand the magmatic dynamics is the melt mobility ($\Delta\rho/\eta$), where $\Delta\rho$ is the density contrast between the melt and its surroundings. The melt mobility is therefore largely influenced by temperature, pressure and composition. The depth at which the viscosity becomes least, the melt mobility becomes maximum which is ~20 times higher than the value near the surface. Increased melt mobility implies that the flow resistance is reduced drastically. A more rigorous understanding of the distribution of the melt mobility will unravel the long standing geophysical mysteries surrounding the origin of large igneous regions [238], nature of the asthenosphere and low-velocity zone, *etc.* [239]

5.5 Summary

Earlier, classical MD calculations on silicate melts were performed using semi-empirical force fields [240]. The transition to *ab initio* MD is fairly recent and paved the way to many theoretical studies of silicates. Most of the studies have been limited to rather simple systems, *e.g.* pure silica. The advancement has been gradual with the inclusion of more components that are similar to natural magma, by considering binary to ternary systems. Although these silicate and aluminosilicate systems were good approximations to describe basaltic systems, however, the lack of other significant components (occurring in natural basalt) showed some discrepancy in the MD results. Recently, model basalt and mid-ocean ridge basalt (MORB) have been studied using AIMD. In this chapter, we investigated the structural, thermodynamic, elastic, electronic and transport properties of both glass and molten model basalt. Owing to the experimental difficulty in studying melts at high pressure, the study of the corresponding glass structure helps (within a

certain error range) to draw parallels between the glass and melt. The present study of basalt glass and melt over a wide pressure range enables us to better understand and explain the pressure response of various structural and physical properties, such as bond distances, coordination, density, elasticity, *etc.*, obtained from first principles MD simulations. The structural changes on being compressed, occur continuously and is characteristically similar to that seen in molten and glass silicates. For both the glass and melt, the considered pressure range can be broadly classified into two regions: an initial accelerated region interval where changes are rapid, and comparatively slower changes thereafter. For the glass at 300 K, the effect of pressure on the Si environment appears to remain almost unchanged in the 0–15 GPa interval, despite continuous increase in density. This compression regime can be attributed to changes in the network topology and oxygen coordination around the other cations, specifically aluminium. On the other hand, for the melt, the environment around the Si atoms does change significantly compared to the glass. The absence of this trait in the melt system signals kinetic hindrance in the cold-compressed glass. It is, therefore, likely that the characteristics of the molten basalt that we studied will resemble more closely to that of actual melts.

The calculated diffusion coefficient and coefficient of viscosity show one to two orders of variation in magnitude over the investigate pressure range. Since aluminium has more tendency to be seven fold coordinated compared to silicon, thus aluminium has more network forming possibility. The presence of odd cation–anion coordination (Si and Al) species and the inclusion of network modifying species (Ca and Mg) are likely to lower the viscosity, thus explaining the dynamical anomalies. On including network modifiers, the bond breaking and formation gets facilitated more, rendering the oxygen atoms more mobile. This decreases the overall viscosity of the melt. In fact, this can even be verified from the coefficients of diffusion of the different species as shown in Fig. 5.35. From 0 to 18 GPa, the diffusion coefficients of Si and Al tend to increase,

which is the same pressure range after which the five fold coordination starts to appear. Similarly, after 50 GPa and 80 GPa respectively, the diffusion coefficients of Ca and Mg suddenly increase noticeably, possibly resulting in the decrease in the coefficient of viscosity. As stated and illustrated in the previous sections, our data matches quite well with that of both silicate and aluminosilicate glasses and melts obtained from experiments.

Further studying the structural and transport properties of simulated glasses and melts with compositional variance of Si and Al will help us better constrain the trend obtained from simulations enabling us to make more rigorous comparison with existing experimental data. Our results will hopefully contribute to the better understanding of the origin, stability and mobility of magmatic and partial melts in the present day mantle as well as he mantle in the early stages of the Earth.

CHAPTER 6

GENERAL SUMMARY

The general aim of this thesis is to theoretically investigate and predict structural transitions and various properties of selected materials at high pressure. The theoretical calculations are performed using *ab initio* methods. The *ab initio* methods includes density functional theory (DFT), molecular dynamics (MD) and metadynamics. These tools have been used to study structural phase transitions, thermodynamic, electronic, vibrational and transport properties of the selected materials.

In Chapter 1, the theoretical methods are discussed, establishing the fundamental theory behind the computational tools that are employed for all the calculations.

Chapter 2 describes the application of *ab initio* metadynamics method to describe a first order structural phase transition in aluminium triiodide (AlI$_3$) at high pressure, which was not reported experimentally. The results are verified by Raman spectra. The conclusion of the chapter is that *ab initio* metadynamics method is a very powerful tool to scan the potential energy surface and search for locally (metastable) or globally (ground state) configurations.

In Chapter 3, *ab initio* metadynamics and molecular dynamics are applied to describe the structural phase transition in superconducting hydrogen sulfide (H$_2$S) at high pressure. Our theoretical findings corroborate the experimental results. Moreover, in this chapter, *ab initio* techniques have also been used to determine superconducting properties, which also matched excellently with experimental results. This work is the only work available in literature that successfully and unambiguously describes the high pressure structure as well as the electronic properties of the superconducting phase of H$_2$S simultaneously, while other theoretical studies are

unable to bridge the gap between theory and experiment by describing both the structure and superconductivity of H_2S.

Chapter 4 deals with the *ab initio* technique to find the superconducting properties of a newly synthesized polyhydride of iron (FeH_5) at high pressure. In this chapter, FeH_5 is found to have low superconducting critical temperature, although it has atomic hydrogen rings, an ingredient proposed to be key for high temperature superconductivity. We describe other delicate factors which determine the superconducting critical temperature, thus providing an effective pathway to synthesizing high temperature hydride superconductors.

Lastly, Chapter 5, is a geophysical topic, that deals with the structural changes and transport properties of basaltic material at mantle conditions, *i.e.* high pressure and temperature. Basalt is an aluminosilicate material containing other components (MgO, CaO, *etc.*). Both the amorphous glass and melt structures of basalt were studied by employing *ab initio* molecular dynamics. The structural and transport properties obtained agree quite well with other experimental and theoretical studies on silicates and aluminosilicate. From our results we have described the fate of the basaltic magma at different depths beneath the surface of the Earth and also the anomalous viscosity of basalt when compressed. A well rounded and connected explanation is given in this chapter, making links between the radial distribution function, bond lengths, coordination numbers, densities, elastic properties and transport properties. The results give a better understanding of the thermochemical and compositional evolution of the Earth ad can help solve geophysical problems.

APPENDIX A

Supplementary Data for Chapter 2

Mode symmetry and frequency (cm^{-1})	Born effective charge (e)	Raman Tensors		
B$_g$ 57		-0.000000000	0.000591090	0.000000000
		0.000591090	-0.000000000	-0.000857925
		0.000000000	-0.000857925	-0.000000000
A$_g$ 62		0.000917225	-0.000000000	0.000546853
		-0.000000000	-0.000379414	0.000000000
		0.000546853	0.000000000	-0.000288564
B$_u$ 76	0.582			
B$_g$ 84		-0.000000000	-0.000356454	0.000000000
		-0.000356454	-0.000000000	0.000450308
		0.000000000	0.000450308	0.000000000
A$_u$ 94	1.471			
B$_u$ 95	1.176			
A$_g$ 98		0.001405799	0.000000000	-0.000646347
		0.000000000	0.002487649	0.000000000
		-0.000646347	0.000000000	-0.001248360
B$_g$ 99		-0.000000000	0.000056637	0.000000000
		0.000056637	-0.000000000	0.001263687
		0.000000000	0.001263687	0.000000000
A$_g$ 104		-0.001933596	0.000000000	-0.001295203
		0.000000000	-0.001653264	0.000000000
		-0.001295203	0.000000000	0.002036924
B$_g$ 116		-0.000000000	-0.001841896	-0.000000000
		-0.001841896	0.000000000	0.000583977
		-0.000000000	0.000583977	-0.000000000
A$_g$ 119		-0.002501825	0.000000000	0.000225807
		0.000000000	0.001452588	-0.000000000
		0.000225807	-0.000000000	0.000682402
B$_u$ 122	0.818			
A$_u$ 128	0.636			
A$_u$ 140	0.647			
A$_g$ 149		0.006269211	-0.000000000	-0.000311400
		-0.000000000	0.006500436	0.000000000
		-0.000311400	0.000000000	0.013375048

B$_g$	243		0.000000000	-0.000175317	-0.000000000
			-0.000175317	0.000000000	0.000171560
			-0.000000000	0.000171560	0.000000000
B$_u$	254	5.245			
A$_u$	255	5.238			
A$_g$	292		0.000098407	0.000000000	0.000959569
			0.000000000	-0.000561436	-0.000000000
			0.000959569	-0.000000000	-0.000580645
B$_g$	293		-0.000000000	0.000128338	-0.000000000
			0.000128338	-0.000000000	-0.000977968
			-0.000000000	-0.000977968	-0.000000000
B$_u$	365	3.972			

TABLE A1 Predicted Infrared and Raman activity for *C2/m* AlI3 at 4.8 GPa obtained from DFPT calculations.

REFERENCES

[1]   W. B. Holzapfel, *Rep. Prog. Phys.* **59**, 28 (1996).

[2]   J. V. Badding, *Annu. Rev. Mater. Sci.* **28**, 631 (1998).

[3]   R. J. Hemley, *Annu. Rev. Phys. Chem.* **51**, 763 (2000).

[4]   P. F. McMillan, *Nat. Mater.* **1**, 19 (2002).

[5]   P. McMillan, *High Press. Res.* **23**, 7 (2003).

[6]   P. F. McMillan, *Chem. Soc. Rev.* **35**, 855 (2006).

[7]   W. Grochala, R. Hoffmann, J. Feng, and N. W. Ashcroft, *Angew. Chem. Int. Ed.* **46**, 3620 (2007).

[8]   P. F. McMillan, *High Press. Res.* **24**, 67 (2004).

[9]   P. F. McMillan, *Nat. Mater.* **4**, 715 (2005).

[10] R. J. Hemley, *High Press. Res.* **30**, 581 (2010).

[11] L. Zhang, Y. Wang, J. Lv, and Y. Ma, *Nat. Rev. Mater.* **2**, 17005 (2017).

[12] H. K. Mao, X. J. Chen, Y. Ding, B. Li, and L. Wang, *Rev. Mod. Phys.* **90,** 015007 (2018).

[13] R. H. Wentorf, *J. Chem. Phys.* **26**, 956 (1957).

[14] W. Zhang *et al.*, *Science* **342**, 1502 (2013).

[15] X. Li, A. Hermann, F. Peng, J. Lv, Y. Wang, H. Wang, and Y. Ma, *Sci. Rep.* **5**, 16675 (2015).

[16] M. S. Miao, X. L. Wang, J. Brgoch, F. Spera, M. G. Jackson, G. Kresse, and H. Q. Lin, *J. Am. Chem. Soc.* **137**, 14122 (2015).

[17] L. Zhu, H. Liu, C. J. Pickard, G. Zou, and Y. Ma, *Nat. Chem.* **6**, 644 (2014).

[18] A. P. Drozdov, M. I. Eremets, I. A. Troyan, V. Ksenofontov, and S. I. Shylin, *Nature* **525**, 73 (2015).

[19] M. I. Eremets, I. A. Trojan, S. A. Medvedev, J. S. Tse, and Y. Yao, *Science* **319**, 1506 (2008).

[20] Y. Wang, and Y. Ma, *J. Chem. Phys.* **140**, 40901 (2014).

[21] N. Dubrovinskaia *et al.*, *Sci. Adv.* **2**, e1600341 (2016).

[22] P. Hohenberg and W. Kohn, *Phys. Rev.* **136**, B864 (1964).

[23] W. Kohn and L. J. Sham, *Phys. Rev.* **140**, A1133 (1965).

[24] S. Kirkpatrick, C. D. Gelatt, and M. P. Vecchi, *Science* **220**, 671 (1983).

[25] S. Goedecker, *J. Chem. Phys.* **120**, 9911 (2004).

[26] R. Car and M. Parrinello, *Phys. Rev. Lett.* **55**, 2471 (1985).

[27] J. S. Tse, *Annu. Rev. Phys. Chem.* **53**, 249 (2002).

[28] A. Laio and M. Parrinello, *Proc. Natl Acad. Sci. U S A* **99**, 12562 (2002).

[29] C. J. Pickard and R. J. Needs, *J. Phys. Condens. Matter* **23**, 053201 (2011).

[30] G. Trimarchi and A. Zunger*, Phys. Rev. B* **75**, 104113 (2007).

[31] D. C. Lonie and E. Zurek, *Comput. Phys. Commun.* **182**, 372 (2011).

[32] A. R. Oganov and C. W. Glass, *J. Chem. Phys.* **124**, 244704 (2006).

[33] A. N. Kolmogorov, S. Shah, E. R. Margine, A. F. Bialon, T. Hammerschmidt, and R. Drautz, *Phys. Rev. Lett.* **105**, 217003 (2010).

[34] C. Buzea and K. Robbie, *Supercond. Sci. Technol.* **18**, R1 (2005).

[35] J. J. Hamlin, *Phys. C Supercond. Appl.* **514**, 59 (2015).

[36] M. Pépin, G. Geneste, A. Dewaele, M. Mezouar, and P. Loubeyre, *Science* **357**, 382 (2017).

[37] M. Born and R. Oppenheimer, *Anna. Phys.* **389**, 457 (1927).

[38] L. H. Thomas, *Math. Proc. Cambridge Philos. Soc.* **23**, 542 (1927).

[39] E. Fermi, *Rend. Accad. Naz. Lincei* **6**, 602 (1927).

[40] E. Fermi, *Z. Phys.* **48**, 73 (1928).

[41] N. M. Harrison, *Computational Materials Science (IOS Press, Amsterdam,* 2003).

[42] D. M. Ceperley and B. J. Alder, *Phys. Rev. Lett.* **45**, 566 (1980).

[43] G. D. Mahan, *Many-Particle Physics* (Plenum Press, New York, 1990).

[44] J. P. Perdew and W. Yue, *Phys. Rev. B* **33**, 8800 (1986).

[45] J. P. Perdew and W. Yue, *Phys. Rev. B* **40**, 3399 (1989).

[46] J. P. Perdew, K. Burke, and M. Ernzerhof, *Phys. Rev. Lett.* **77**, 3865 (1996).

[47] M. Santoro, F. A. Gorelli, R. Bini, J. Haines, O. Cambon, C. Levelut, J. A. Montoya, and S. Scandolo, *Proc. Natl. Acad. Sci. U S A* **109**, 5176 (2012).

[48] V. I. Anisimov and O. Gunnarsson, *Phys. Rev. B*, **43**, 7570 (1991).

[49] I. V. Solovyev and P. H. Dederichs, *Phys. Rev. B*, **49**, 6736 (1994).

[50] A. Bloch, *Ann. Fac. Sci. Toulouse* **17**, 1 (1925).

[51] R. Orlando, R. Dovesi, C. Roetti, and V. R. Saunders, *J. Phys. Condens. Matter* **2**, 7769 (1990).

[52] M. S. José, A. Emilio, D. G. Julian, G. Alberto, J. Javier, O. Pablo, and S.-P. Daniel, *J. Phys. Condens. Matter* **14**, 2745 (2002).

[53] J. B. Foresman and A. Frisch, *Exploring Chemistry with Electronic Structure Methods*, 3rd ed. (Gaussian Inc., Pittsburg, 1996).

[54] P. E. Blöchl, *Phys. Rev. B* **50**, 17953 (1994).

[55] G. Kresse and J. Hafner, *Phys. Rev. B* **47**, 558 (1993).

[56] G. Kresse and J. Hafner, *Phys. Rev. B* **49**, 14251 (1994).

[57] G. Kresse and J. Furthmüller, *Computational Materials Science* **6**, 15 (1996).

[58] T. Bučko, J. Hafner, S. Lebègue, and J. G. Ángyán, *J. Phys. Chem. A* **114**, 11814 (2010).

[59] B. J. Alder and T. E. Wainwright, *J. Chem. Phys.* **27**, 1208 (1957).

[60] B. J. Alder and T. E. Wainwright, *J. Chem. Phys.* **31**, 459 (1959).

[61] M. P. Allen and D. J. Tildesley, *Computer simulation of liquids*, REP ed. (Clarendon Press, Wotton-under-Edge, 1989).

[62] K. Mizushima, S. Yip, and E. Kaxiras, *Phys. Rev. B* **50,** 14952 (1994).

[63] A. Laio and M. Parrinello, *Proc. Natl. Acad. Sci. U S A* **99,** 12562 (2002).

[64] R. Martoňák, A. Laio, and M. Parrinello, *Phys. Rev. Lett.* **90**, 075503 (2003).

[65] R. Martoňák *et al.*, *Nature Mater.* **5**, 623 (2006).

[66] J. Bardeen, L. N. Cooper, and J. R. Schrieffer, *Phys. Rev.* **108**, 1175 (1957).

[67] J. R. Schrieffer, *Theory of Superconductivity*, 1st ed. (Benjamin, New York, 1964).

[68] Y. Yao, University of Saskatchewan, 2008.

[69] G. M. Eliashberg, *Sov. Phys. JETP* **11**, 696 (1960).

[70] G. M. Eliashberg, *Zh. Eksp. Teor. Fiz.* **38**, 966 (1960).

[71] A. B. Migdal, *Sov. Phys. JETP* **34**, 996 (1958).

[72] A. B. Migdal, *Zh. Eksp. Teor. Fiz.* **34**, 1438 (1958).

[73] J. P. Carbotte, *Rev. Mod. Phys.* **62**, 1027 (1990).

[74] W. L. McMillan, *Phys. Rev.* **167**, 331 (1968).

[75] P. B. Allen and R. C. Dynes, *J. Phys. C* **8**, L158 (1975).

[76] P. B. Allen and R. C. Dynes, *Phys. Rev. B* **12**, 905 (1975).

[77] P. Morel and P. W. Anderson, *Phys. Rev.* **125**, 1263 (1962).

[78] Y. G. Jin and K. J. Chang, *Phys. Rev. B* **57**, 14684 (1998).

[79] N. W. Ashcroft, *Phys. Rev. Lett.* **92**, 187002 (2004).

[80] J. K. Freericks, S. P. Rudin, and A. Y. Liu, *Physica B* **425**, 284 (2000).

[81] N. E. Christensen and D. L. Novikov, *Phys. Rev. B* **73**, 224508 (2001).

[82] P. Giannozzi *et al.*, *J. Phys.: Condens. Matter* **21**, 395502 (2009).

[83] X. Yong, University of Saskatchewan, 2016.

[84] M. Hargittai, M. Kolonits, J. Tremmel, J-L. Fourquet, and G. Ferey, *Struct. Chem.* **1**, 75 (1990).

[85] E. Stavrou, J. M. Zaug, S. Bastea, J. C. Crowhurst, A. F. Goncharov, H. B. Radousky, M. R. Armstrong, S. K. Roberts, and J. W. Plaue, *J. Chem. Phys.* **142**, 214506 (2015).

[86] T. Karasawa, T. R. Bramblett, D. Lubben, J. E. Greene, and J. O. Carlsson, *J. Vac. Sci. Technol. A* **11**, 301 (1993).

[87] M. Hargittai, M. Kolonits, and L. Godorhazy, *Chem. Phys. Lett.* **257**, 321 (1996).

[88] M. Hargittai, B. Reffy, and M. Kolonits, *J. Phys. Chem. A* **110**, 3770 (2006).

[89] Z. Varga, M. Kolonits, and M. Hargittai, *Struct. Chem.* **23**, 879 (2012).

[90] M. Yoshioka, N. Takahashi, and T. Nakamura, *Mater. Chem. Phys.* **86**, 74 (2004).

[91] M. Pouget, J. P. Lecompte, and M. J. Billy, *Chim. Phys. Phys. Chim. Biol.* **91**, 547 (1994).

[92] J. Ravez, A. Mogusmilankovic, J. P. Chaminade, and P. Hagenmuller, *Mater Res. Bull.* **19**, 1311 (1984).

[93] P. Daniel, A. Bulou, M. Rousseau, J. Nouet, J. L. Fourquet, M. Leblanc, and R. Burriel, *J. Phys.: Condens. Matter* **2**, 5663 (1990).

[94] S. I. Troyanov, T. Krahl, and E. Kemnitz, *Z. Kristallogr.* **219**, 88 (2004).

[95] S. I. Troyanov, *Zh. Neorg. Khim.* **39**, 552 (1994).

[96] Y. Yao and D. D. Klug, *J. Chem. Phys.* **138**, 094501 (2013).

[97] W. Kohn, *Rev. Mod. Phys.* **61**, 689 (1989).

[98] G. Kresse and D. Joubert, *Phys. Rev. B* **59**, 1758 (1999).

[99] H. J. Monkhorst and J. D. Pack, *Phys. Rev. B* **13**, 5188 (1976).

[100] D. Alfe, *Comp. Phys. Com.* **180**, 2622 (2009).

[101] X. Gonze *et al.*, *Comp. Phys. Com.* **180**, 2582 (2009).

[102] M. Veithen, X. Gonze, and Ph. Ghosez, *Phys. Rev. B* **71**, 125107 (2005).

[103] N. Troullier and J. Martins, *Phys. Rev. B* **43,** 1993 (1991).

[104] M. Schluter, M. L. Cohen, S. E. Kohn, and C. Y. Fong, *Phys. Status Solidi B* **78**, 737 (1976).

[105] H. Yorikawa and S. Muramatsu, *J. Phys.: Condens. Matter* **20**, 325220 (2008).

[106] J. D. Forrester, A. Zalkin, and D. H. Templeton, *Inorg. Chem.* **3**, 63 (1964).

[107] H. R. Brooker and T. A. Scott, *J. Chem. Phys.* **41**, 475 (1964).

[108] N. Hamaya, M. Ishizuka, S. Onoda, J. Guishan, A. Ohmura, and K. Shimizu, *Phys. Rev. B* **82**, 094506 (2010).

[109] Y. Yao, D. D. Klug, R. Martonak, and S. Patchkovskii, *Phys. Rev. B* **83**, 214105 (2011).

[110] D. Duan, X. Huang, C. Chen, F. Tian, K. Bao, D. Li, Y. Liu, H. Yu, B. Liu, and T. Cui, *RSC Adv.* **4**, 32068 (2014).

[111] C. J. Pickard and R. J. Needs, *Phys. Rev. Lett.* **97**, 045504 (2006).

[112] R. W. G. Wyckoff, *Crystal Structures*, 2nd ed. (Wiley, New York, 1964).

[113] A. Majumdar, D. D. Klug, and Y. Yao, *J. Chem. Phys.* **144**, 124507 (2016).

[114] Y. Li, J. Hao, H. Liu, Y. Li, and Y. Ma, *J. Chem. Phys.* **140**, 174712 (2014).

[115] D. Duan, Y. Liu, F. Tian, D. Li, X. Huang, Z. Zhao, H. Yu, B. Liu, W. Tian, and T. Cui, *Sci. Rep.* **4**, 6968 (2014).

[116] R. Akashi, W. Sano, R. Arita, and S. Tsunneyuki, *Phys. Rev. Lett.* **117**, 075503 (2016).

[117] Y. Liu, L. Wang, H. Liu, Y. Zhang, J. Hao, C. J. Pickard, J. R. Nelson, R. J. Needs, W. Li, Y. Huang, I. Errea, M. Calandra, F. Mauri, and Y. Ma, *Phys. Rev. B*, **93**, 020301 (2016).

[118] A. F. Goncharov, S. S. Lobanov, I. Kruglov, X.-M. Zhao, X-J. Chen, A. R. Oganov, Z. Konôpková, and V. B. Prakapenka, *Phys. Rev. B*, **93**, 174105 (2016).

[119] M. Einaga, M. Sakata, T. Ishikawa, K. Shimizu, M. I. Eremets, A. P. Drozdov, I. A. Troyan, N. Hirao, and Y. Ohishi, *Nature Phys.* **12**, 835 (2016).

[120] A. F. Goncharov, S. S. Lobanov, V. B. Prakapenka, and E. Greenberg, *Phys. Rev. B* **95**, 140101(R) (2017).

[121] E. E. Gordon, K. Xu, H. Xiang, A. Bussmann-Holder, R. K. Kremer, A. Simon, J. Köhler, and M-H. Whangbo, *Angew. Chem. Int. Ed.* **128**, 3746 (2016).

[122] B. Guigue, A. Marizy, and P. Loubeyre, *Phys. Rev. B* **95**, 020104(R) (2017).

[123] Y. Yao and D. D. Klug, *Phys. Rev. B* **88**, 014113 (2013).

[124] Y. Yao and D. D. Klug, *Phys. Rev. B* **85**, 214122 (2012).

[125] R. F. W. Bader, *Atoms in Molecules – A Quantum Theory*, (Oxford University Press, Oxford, 1990).

[126] R. F. W. Bader, *Acc. Chem. Res.* **18**, 9 (1985).

[127] I. Errea, M. Calandra, C. J. Pickard, J. R. Nelson, R. J. Needs, Y. Li, H. Liu, Y. Zhang, Y. Ma, and F. Mauri, *Nature* **532**, 81 (2016).

[128] M. Benoit, D. Marx, and M. Parrinello, *Nature* **392**, 258 (1998).

[129] R. Rousseau, M. Boero, M. Bernasconi, M. Parrinello, and K. Terakura, *Phys. Rev. Lett.* **85**, 1254 (2000).

[130] Y. Yao, J. S. Tse, Y. Ma, and K. Tanaka, *Europhys. Lett.* **78**, 37003 (2007).

[131] J. S. Tse, Y. Yao, and K. Tanaka, *Phys. Rev. Lett.* **98**, 117004 (2007).

[132] A. Simon, *Angew. Chem., Int. Ed. Engl.* **36**, 1788 (1997).

[133] T. Ishikawa, A. Nakanishi, K. Shimizu, H. Katayama-Yoshida, T. Oda, and N. Suzuki, *Sci. Rep.* **6**, 23160 (2016).

[134] R. Akashi, M. Kawamura, S. Tsuneyuki, Y. Nomura, and R. Arita, *Phys. Rev. B* **91**, 224513 (2015).

[135] P. Pavone, S. Baroni, and S. de Gironcoli, *Phys. Rev. B* **57**, 10421 (1998).

[136] A. Majumdar, J. S. Tse, and Y. Yao, *Angew. Chem. Int. Ed.*, **56**, 11390 (2017).

[137] N. W. Ashcroft, *Phys. Rev. Lett*. **21**, 1748 (1968).

[138] D. D. Klug and Y. Yao, *Phys. Chem. Chem. Phys*. **13**, 16999 (2011).

[139] R. P. Dias and I. F. Silvera, *Science* **355**, 715 (2017).

[140] D. Castelvecchi, *Nature* **542**, 17 (2017).

[141] R. F. Service, *Science* **355**, 332 (2017).

[142] H. Wang, J. S. Tse, K. Tanaka, T. Iitaka, and Y. Ma, *Proc. Natl. Acad. Sci. U S A* **109**, 6463 (2012).

[143] Y. Li, J. Hao, H. Liu, J. S. Tse, Y. Wang, and Y. Ma, *Sci. Rep.* **5**, 9948 (2015).

[144] H. Liu, I. I. Naumov, R. Hoffmann, N. W. Ashcroft, and R. J. Hemley, *Proc. Natl. Acad. Sci. U S A* **114**, 6990 (2017).

[145] F. Peng, Y. Sun, C. J. Pickard, R. J. Needs, Q. Wu, and Y. Ma, *Phys. Rev. Lett.* **119**, 107001 (2017).

[146] C. J. Pickard and R. J. Needs, *Nat. Phys*. **3**, 473 (2007).

[147] M. Cococcioni and S. de Gironcoli, *Phys. Rev.* B **71**, 035105 (2005).

[148] B. G. Janesko, T. M. Henderson, and G. E. Scuseria, *Phys. Chem. Chem. Phys*. **11**, 443 (2009).

[149] Y. Wang, H. Wang, J. S. Tse, T. Iitaka, and Y. Ma, *Phys. Chem. Chem. Phys*. **17**, 19379 (2015).

[150] J. Hooper, T. Terpstra, A. Shamp, and E. Zurek, *J. Phys. Chem. C* **118**, 6433 (2014).

[151] D. C. Lonie, J. Hooper, B. Altintas, and E. Zurek, *Phys. Rev. B* **87**, 054107 (2013).

[152] E. Zurek, R. Hoffmann, N. W. Ashcroft, A. R. Oganov, and A. O. Lyakhov, *Proc. Natl. Acad. Sci. U S A* **106**, 17640 (2009).

[153] A. D. Becke and K. E. Edgecombe. *J. Chem. Phys*. **92**, 5397 (1990).

[154] P. H.-L. Sit, R. Car, M. H. Cohen, and A. Selloni, *Inorg. Chem.* **50**, 10259 (2011).

[155] P. Cudazzo, G. Profeta, A. Sanna, A. Floris, A. Continenza, S. Massidda, and E. K. U. Gross, *Phys. Rev. Lett.* **100**, 257001 (2008).

[156] K. Tanaka, J. S. Tse, and H. Liu, *Phys. Rev. B* **96**, 100502(R) (2017).

[157] A. G. Kvashnin, I. A. Kruglov, D. V. Semenok, and A. R. Oganov, *J. Phys. Chem. C* **122**, 4731 (2018).

[158] A. Majumdar, J. S. Tse, and Y. Yao, *Phys. Rev. B* **96**, 201107 (2017).

[159] M. G. Best, *Igneous and Metamorphic Petrology*, 2nd ed. (Wiley-Blackwell, Hoboken, 2002).

[160] L. Stixrude and B. Karki, *Science* **310**, 297 (2005).

[161] A. Lopez-Noriega, D. Arcos, I. Izquierdo-Barba, Y. Sakamoto, O. Terasaki, and M. Vallet-Regi, *Chem. Mater.* **18**, 3137 (2006).

[162] H. H. Kim, F. Miyaji, T. Kokubo, C. Ohtsuki, and T. Nakamura, *J. Am. Ceram. Soc.* **78**, 2405 (1995).

[163] R. E. Schenker and W. G. Oldham, *J. Appl. Phys.*, **82**, 1065 (1997).

[164] P. D. Asimow and T. J. Ahrens, *J. Geophys. Res.* **115**, B10209 (2010).

[165] C. Sanloup, J. W. E. Drewitt, Z. Konopkova, P. D-Simpson, D. M. Morton, N. Rai, W. van Westrenen, W. Morgenroth, *Nature* **503**, 104 (2013).

[166] Q. Williams, R. Jeanloz, *Science* **239**, 902 (1988).

[167] J. D. Kubicki, R. J. Hemley, A. M. Hofmeister, *Am. Mineral.* **77**, 258 (1992).

[168] C. Meade, R. J. Hemley, H. K. Mao, *Phys. Rev. Lett.* **69**, 1387 (1992).

[169] S. Petitgirard, W. J. Malfait, R. Sinmyo, I. Kupenko, L. Hennet, D. Harries, T. Dane, M. Burghammer, D. C. Rubie, *Proc. Natl. Acad. Sci. U S A* **112**, 14186 (2015).

[170] S. Petitgirard *et al.*, *Phys. Rev. Lett.* **119**, 215701 (2017).

[171] S. E. Haggerty and V. Sautter, *Science* **248**, 993 (1990).

[172] C. Herzberg, *Chem. Geol.* **126**, 1 (1995).

[173] G. H. Miller, E. M. Stolper, and T. J. Ahrens, *J. Geophys. Res.* **96**, 11831 (1991).

[174] Q. Williams and E. J. Garnero, *Science*, **273**, 1528 (1996).

[175] R. M. Canup, *Annu. Rev. Astron. Astrophys.* **42**, 441 (2004).

[176] S. Labrosse, J. Hernlund, and N. Coltice, *Nature* **450**, 866 (2007).

[177] B. E. John and M. J. Cheadle, *Slow-spreading mid-ocean ridges,* 10th ed. (McGraw-Hill Inc., New York City, 2007).

[178] S. Labrosse, J. W. Hernlund, and N. Coltice, *Nature*, 450, 866 (2007).

[179] R. L. Mozzi and B. E. Warren, *J. Appl. Crystallogr.* **2**, 164 (1969).

[180] R. J. Hemley, H. K. Mao, P. M. Bell, and B. O. Mysen, *Phys. Rev. Lett.* **57**, 747 (1986).

[181] D. L. Price and J. M. Carpenter, *J. Non-Cryst. Solids* **92**, 153 (1987).

[182] X. Xue, J. F. Stebbins, M. Kanzaki, P. F. McMillan, and B. Poe, *Am. Mineral.* **76**, 8 (1991).

[183] S. Susman, K. J. Volin, D. L. Price, M. Grimsditch, J. P. Rino, R. K. Kalia, P. Vashishta, G. Gwanmesia, Y. Wang, and R. C. Liebermann, *Phys. Rev. B* **43**, 1194 (1991).

[184] J. R. Rustad, D. A. Yuen, and F. J. Spera, *Phys. Rev.* B **44**, 2108 (1991).

[185] L. Stixrude and M. S. T. Bukowinski, *Phys. Rev. B* **44**, 2523 (1991).

[186] J. P. Rino, I. Ebbsjo, R. K. Kalia, A. Nakano, and P. Vashishta, *Phys. Rev. B* **47**, 3053 (1993).

[187] W. Jin, R. K. Kalia, P. Vashishta, and J. P. Rino, *Phys. Rev. Lett.* **71**, 3146 (1993).

[188] J. R. Rustad, D. A. Yuen, and F. J. Spera, *Phys. Rev. A* **42**, 2081 (1990).

[189] C. S. Marians and L. W. Hobbs, *J. Non-Cryst. Solids* **124**, 242 (1990).

[190] J. Horbach and W. Kob, *Phys. Rev. B* **60**, 3169 (1999).

[191] M. Wu, Y. Liang, J.Z. Jiang, and J. S. Tse, *Sci. Rep.* **2**, 398 (2012).

[192] C. A. Angell, P. A. Cheeseman, and S. Tamaddon, *Science* **218**, 885 (1982).

[193] J. Revenaugh and S. A. Sipkin, *Nature* **369**, 474 (1994).

[194] J. Monteux, D. Andrault, and H. Samuel, *Earth Planet. Sc. Lett.* **448**, 140 (2016).

[195] J. B. Wacheul, M. Le Bars, J. Monteux, and J. M. Aurnou, *Earth Planet. Sc. Lett.* **403**, 236 (2014).

[196] O. Adjaoud, G. Steinle-Neumann, and S. Jahn, *Earth Planet. Sc. Lett.* **312**, 3 (2011).

[197] M. Bauchy, B. Guillot, M. Micoulaut, and N. Sator, *Chem. Geol.* **346**, 47 (2013).

[198] F. Bejina and O. Jaoul, *Earth Planet. Sc. Lett.* **153**, 229 (1997).

[199] D. B. Dingwell and D. Virgo, *Geochim. Cosmochim. Acta.* **52**, 395 (1988).

[200] J. R. Farver and R. A. Yund, *Geophys. Res. Lett.* **27**, 2337 (2000).

[201] S. M. Fortier and B. J. Giletti, *Science* **245**, 1481 (1989).

[202] Y. Sun, H. Zhou, K. Yin, M. Zhao, S. Xu, and X. Lu, *J. Geophys. Res.: Solid Earth* **123** (2018).

[203] P. Ganster, M. Benoit, W. Kob, and J. M. Delaye, *J. Chem. Phys.* **120**, 10172 (2004).

[204] N. A. Morgan and F. J. Spera, *Geochim. Comochim. Acta.* **65**, 4019 (2001).

[205] B. O. Mysen and P. Richet, *Silicate glasses and melts, properties and structure*, 1st ed. (Elsevier, Amsterdam, 2005).

[206] D. R. Neuville, L. Cormier, and D. Massiot, *Chem. Geol.* **229**, 173 (2006).

[207] D. B. Ghosh and B. B. Karki, *Phys. Chem. Miner.* **45**, 575 (2018).

[208] N. Sun, L. Stixrude, N. de Koker, and B. B. Karki, *Geochim. Cosmochim. Acta.* **75**, 3792 (2011).

[209] F. J. Spera, D. Nevins, M. Ghiorso, and I. Cutler, *Geochim. Cosmochim. Acta.* **73**, 6918 (2009).

[210] B. B. Karki, B. Bohara, and L. Stixrude, *Am. Mineral.* **96**, 744 (2011).

[211] S. Nosé, *J. Chem. Phys.* **81**, 511 (1984).

[212] A. Ponitzsch, M. Nofz, L. Wondraczek, and J. Deubener, *J. Non Cryst. Solids* **434**, 1 (2016).

[213] A. K. Verma, P. Modak, and B. B. Karki, *Phys. Rev. B* **84**, 174116 (2011).

[214] C. J. Benmore, E. Soignard, S. A. Amin, M. Guthrie, S. D. Shastri, P. L. Lee, and J. L. Yarger, *Phys. Rev. B* **81**, 054105 (2010).

[215] L. Cormier and D. R. Neuville, *Chem. Geol.* **213**, 103 (2004).

[216] T. Sato and N. Funamori, *Phys. Rev. Lett.* **101**, 255502 (2008).

[217] T. Sato and N. Funamori, *Phys. Rev. B* **82**, 184102 (2010).

[218] S. Bajgain, D. B. Ghosh, and B. B. Karki, *Nat. Comm.* **6**, 8578 (2015).

[219] M. L. Rivers and I. S. E. Carmichael, *J. Geophys. Res.* **92**, 9247 (1987).

[220] K. H. Smith, E. Shero, A. Chizmeshya, and G. H. Wolf, *J. Chem. Phys.* **102**, 6851 (1995).

[221] C. S. Zha, R. J. Hemley, H. K. Mao, T. S. Duffy, and C. Meade, *Phys. Rev. B* **50**, 13105 (1994).

[222] B. B. Karki, D. Bhattarai, and L. Stixrude, *Phys. Rev. B* **76**, 104205 (2007).

[223] A. M. Dziewonski and D. L. Anderson, *Phys. Earth Planet. Inter.* **25**, 297 (1981).

[224] S. M. Rigden, T. J. Ahrens, and E. M. Stolper, *Science* **226**, 1071 (1984).

[225] V. S. Solomatov, *Treatise on Geophysics*, 1st ed. (Elsevier, Ney York City, 2007).

[226] B. B. Karki, D. B. Ghosh, and S. K. Bajgain, *Magmas Under Pressure*, 1st ed. (Elsevier, New York City, 2018).

[227] B. B. Karki and L. P. Stixrude, *Science* **328**, 740 (2010).

[228] M. H. Cohen and D. Turnbull, *J. Chem. Phys.* **31**, 1164 (1959).

[229] S. M. Fortier and B. J. Giletti, *Science* **245**, 1481 (1989).

[230] Y. Bottinga and P. Richet, *Geochim. Cosmochim. Acta* **59**, 2725 (1995).

[231] D. B. Ghosh, S. K. Bajgain, M. Mookherjee, and B. B. Karki, *Sci. Rep.* **7**, 848 (2017).

[232] J. E. Reid, *et al.*, *Phys. Earth Planet. In.* **139**, 45 (2003).

[233] J. L. Yarger, K. H. Smith, R. A. Nieman, J. Diefenbacher, G. H. Wolf, B. T. Poe, and P. F. McMillan, *Science* **270**, 1964 (1995).

[234] J. F. Stebbins, *Nature* **351**, 638 (1991).

[235] B. T. Poe, P. F. McMillan, B. Cote, D. Massiot, and J. P. Coutures, *J. Phys. Chem.* **96**, 8220 (1992).

[236] C. Sanloup, *Chem. Geol.* **429**, 51 (2016).

[237] E. M. Stolper, D. Walker, B. H. Hager, and J. F. Hays, J. Geophys. Res. **86**, 6161 (1981).

[238] N. Coltice *et al.*, *Gondwana Res.* **15**, 254 (2009).

[239] G. Schubert, D. L. Turcotte, and P. Olson, *Mantle Convection in the Earth and Planets*, 1st ed. (Cambridge University Press, Cambridge, 2001).

[240] D. Nevins and F. Spera, *Am. Mineral.* **83**, 1220 (1998).

PERMISSIONS

All the figures and tables in Chapter 2 have been adapted with permission from Arnab Majumdar, Dennis D. Klug, and Yansun Yao, High Pressure Structural Changes in Aluminium Triiodide: A First Principles Study, *J. Chem. Phys*. **144**, 124507 (2016). Copyright 2016 American Institute of Physics (see below).

All the figures in Chapter 3 have been adapted with permission from Arnab Majumdar, John S. Tse, and Yansun Yao, Modulated Structure Calculated for Superconducting Hydrogen Sulfide, *Angew. Chem. Int. Ed.*, 56, 11390 (2017). Copyright 2017 John Wiley and Sons (see below).

Figs. 4.1, 4.3, 4.4, 4.5 and 4.6 in Chapter 4 have been adapted with permission from Arnab Majumdar, John S. Tse, and Yansun Yao, Superconductivity in FeH$_5$, *Phys. Rev. B* 96, 201107 (2017). Copyright 2017 American Physical Society (see below).

Figure 4.2 in Chapter 4 have been adapted with permission from M. Pépin, G. Geneste, A. Dewaele, M. Mezouar, and P. Loubeyre, *Science* 357, 382 (2017). Copyright 2017 The American Association for the Advancement of Science (see below).